

DATA-DRIVEN MODELING OF CELL BEHAVIOR, MORPHOGENESIS AND GROWTH IN REGENERATION AND DEVELOPMENT

Fabian Rost

Born on: March 16, 1984 in Radebeul

DISSERTATION

to achieve the academic degree

DOCTOR RERUM NATURALIUM (DR. RER. NAT.)

First referee

Prof. Elly M. Tanaka

Second referee

Prof. Andreas Deutsch

Submitted on: March 15, 2017

Defended on: August 4, 2017

One does not come by studying living things for a lifetime to suppose that physics and chemistry cannot account for them all.¹

¹D. W. Thompson (1992). *On Growth and Form*. Ed. by J. T. Bonner. Canto ed. Cambridge: Cambridge University Press. 376 pp., p. 9

ABSTRACT

The cell is the central functional unit of life. Cell behaviors, such as cell division, movements, differentiation, cell death as well as cell shape and size changes, determine how tissues change shape and grow during regeneration and development. However, a generally applicable framework to measure and describe the behavior of the multitude of cells in a developing tissue is still lacking. Furthermore, the specific contribution of individual cell behaviors, and how exactly these cell behaviors collectively lead to the morphogenesis and growth of tissues are not clear for many developmental and regenerative processes.

A promising strategy to fill these gaps is the continuing effort of making developmental biology a quantitative science. Recent advances in methods, especially in imaging, enable measurements of cell behaviors and tissue shapes in unprecedented detail and accuracy. Consequently, formalizing hypotheses in terms of mathematical models to obtain testable quantitative predictions is emerging as a powerful tool. Tests of the hypotheses involve the comparison of model predictions to experimentally observed data. The available data is often noisy and based on only few samples. Hence, this comparison of data and model predictions often requires very careful use of statistical inference methods. If one chooses this quantitative approach, the challenges are the choice of observables, i.e. what to measure, and the design of appropriate data-driven models to answer relevant questions.

In this thesis, I applied this data-driven modeling approach to vertebrate morphogenesis, growth and regeneration. In particular, I study spinal cord and muscle regeneration in axolotl, muscle development in zebrafish, and neuron development and maintenance in the adult human brain. To do so, I analyzed images to quantify cell behaviors and tissue shapes. Especially for cell behaviors in post-embryonic tissues, measurements of some cell behavior parameters, such as the proliferation rate, could not be made directly. Hence, I developed mathematical models that are specifically designed to infer these parameters from indirect experimental data. To understand how cell behaviors shape tissues, I developed mechanistic models that causally connect the cell and tissue scales.

Specifically, I first investigated the behaviors of neural stem cells that underlie the

regenerative outgrowth of the spinal cord after tail amputation in the axolotl. To do so, I quantified all relevant cell behaviors. A detailed analysis of the proliferation pattern in space and time revealed that the cell cycle is accelerated between 3-4 days after amputation in a high-proliferation zone, initially spanning from 800 μm anterior to the amputation plane. The activation of quiescent stem cells and cell movements into the high-proliferation zone also contribute to spinal cord growth but I did not find contributions by cellular rearrangements or cell shape changes. I developed a mathematical model of spinal cord outgrowth involving all contributing cell behaviors which revealed that the acceleration of the cell cycle is the major driver of spinal cord outgrowth. To compare the behavior of neural stem cells with cell behaviors in the regenerating muscle tissue that surrounds the spinal cord, I also quantified proliferation of mesenchymal progenitor cells and found similar proliferation parameters. I showed that the zone of mesenchymal progenitors that gives rise to the regenerating muscle segments is at least 350 μm long, which is consistent with the length of the high-proliferation zone in the spinal cord.

Second, I investigated shape changes in developing zebrafish muscle segments by quantifying time-lapse movies of developing zebrafish embryos. These data challenged or ruled out a number of previously proposed mechanisms. Motivated by reported cellular behaviors happening simultaneously in the anterior segments, I had previously proposed the existence of a simple tension-and-resistance mechanism that shapes the muscle segments. Here, I could verify the predictions of this mechanism for the final segment shape pattern. My results support the notion that a simple physical mechanism suffices to self-organize the observed spatiotemporal pattern in the muscle segments.

Third, I corroborated and refined previous estimates of neuronal cell turnover rates in the adult human hippocampus. Previous work approached this question by combining quantitative data and mathematical modeling of the incorporation of the carbon isotope ^{14}C . I reanalyzed published data using the published deterministic neuron turnover model but I extended the model by a better justified measurement error model. Most importantly, I found that human adult neurogenesis might occur at an even higher rate than currently believed.

The tools I used throughout were (1) the careful quantification of the involved processes, mainly by image analysis, and (2) the derivation and application of mathematical models designed to integrate the data through (3) statistical inference. Mathematical models were used for different purposes such as estimating unknown parameters from indirect experiments, summarizing datasets with a few meaningful parameters, formalizing mechanistic hypotheses, as well as for model-guided experimental planning. I venture an outlook on how additional open questions regarding cell turnover measurements could be answered using my approach. Finally, I conclude that the mechanistic understanding of development and regeneration can be advanced by comparing quantitative data to the predictions of specifically designed mathematical models by means of statistical inference methods.

PUBLICATIONS

My work as presented in this thesis has contributed to the following four published articles. Additional results from these articles, which were obtained by my co-authors, are either not included in this thesis or reviewed in this thesis only if my work builds up on them.

- Rost, F.², A. Rodrigo Albors², V. Mazurov, L. Bruschi, A. Deutsch, E. M. Tanaka³, and O. Chara³ (2016). Accelerated Cell Divisions Drive the Outgrowth of the Regenerating Spinal Cord in Axolotls. *eLife* 5, e20357. DOI : 10.7554/eLife.20357.
- Vincent, C. D., F. Rost, W. Masselink, L. Bruschi, and E. M. Tanaka (2015). Cellular Dynamics Underlying Regeneration of Appropriate Segment Number during Axolotl Tail Regeneration. *BMC Dev. Biol.* 15, p. 48. DOI : 10.1186/s12861-015-0098-1.
- Rodrigo Albors, A.², A. Tazaki², F. Rost, S. Nowoshilow, O. Chara, and E. M. Tanaka (2015). Planar Cell Polarity-Mediated Induction of Neural Stem Cell Expansion during Axolotl Spinal Cord Regeneration. *eLife* 4, e10230. DOI: 10.7554/eLife.10230.
- Rost, F., C. Eugster, C. Schröter, A. C. Oates, and L. Bruschi (2014). Chevron Formation of the Zebrafish Muscle Segments. *J. Exp. Biol.* 217.21, pp. 3870–3882. DOI: 10.1242/jeb.102202.

²Shared first authorship

³Shared last authorship

CONTENTS

1. Introduction	1
1.1. Cell behavior, morphogenesis and growth in development and regeneration	1
1.2. Specific topics of the thesis	3
1.3. Data-driven mathematical models in development and regeneration	5
1.4. Structure of the thesis	7
2. Methods	11
2.1. Statistical inference	11
2.1.1. Likelihood	11
2.1.2. Parameter estimation	12
Frequentist approach: Maximum-likelihood and Least-squares method	12
Bayesian approach	13
Bootstrapping	14
2.1.3. Model selection: Akaike information criterion	15
2.1.4. Statistical nomenclature	16
2.2. Numerical methods	16
2.2.1. Model simulation	16
2.2.2. Statistical inference	16
Parameter estimation for empirical model of chevron angle time course	16
2.2.3. Data analysis	17
2.3. Image analysis	18
2.3.1. Angle measurements to quantify chevron formation	18
3. Regeneration of spinal cord and muscle segments in axolotl	21
3.1. Introduction	21
3.1.1. Morphology of the spinal cord	22
3.1.2. Spinal cord regeneration	22
3.1.3. Quantitative analysis strategy	23

3.2. Results: Spinal cord regeneration	25
3.2.1. Spinal cord outgrowth time-course	25
3.2.2. A proliferation-driven outgrowth model	26
3.2.3. Cell behaviors that could drive outgrowth	30
3.2.4. Quantification of cell behaviors	32
Cell length	32
Cell rearrangements	32
Spatiotemporal pattern of proliferation	34
Quantification of proliferation rate time-course	37
Activation of quiescent stem cells	39
Cell influx	40
3.2.5. Mechanistic model of spinal cord outgrowth	40
3.2.6. Application of the mechanistic model to perturbed regeneration	45
3.3. Results: Muscle segment regeneration	47
3.3.1. Cell cycle analysis	47
3.3.2. Total number of cells in the mesenchymal blastema and size of source zone	49
3.4. Discussion	51
3.4.1. Cell behaviors driving spinal cord outgrowth	51
3.4.2. Understanding of perturbed regeneration	52
3.4.3. The cell pushing mechanism	53
3.4.4. Comparison of regeneration parameters in spinal cord and muscle	55
3.5. Conclusion	55
4. Development of muscle segments in zebrafish	57
4.1. Introduction	57
4.1.1. Chevron shape of muscle segments	58
4.1.2. Suggested mechanistic explanations for the chevron's emergence	60
4.2. Results	62
4.2.1. Quantification of chevron formation in mobile embryos	62
4.2.2. Empirical model to summarize chevron angle time course	64
4.2.3. Quantitative description of chevron formation	65
4.2.4. Role of body movements	67
4.2.5. Role of simple chevron templating	67
4.2.6. Inhibition of muscle pioneer differentiation	67
4.3. Discussion	69
4.3.1. Insufficiencies of three proposed mechanisms to explain chevron formation	69
4.3.2. U-shaped myotome mutants and the role of muscle pioneers	70
4.3.3. A mechanical model for the self-organization of heterogeneous chevron angles	71
4.3.4. Chevron patterns in other species and evolutionary aspects	77

4.4. Conclusion	78
5. Neurogenesis in the adult human brain	79
5.1. Introduction	79
5.2. Results	81
5.2.1. Maximum-likelihood estimation of cell turnover parameters	81
5.2.2. Estimation of additional number of subjects needed to infer turnover rate	84
5.3. Discussion	87
5.4. Conclusion	89
6. Summary and outlook	91
Appendix A. Supplementary figures	95
Appendix B. Supplementary calculations	103
B.1. Overdamped dynamics of the mechanical model of chevron formation . . .	103
B.2. Mathematical model of neuron turnover in the adult human hippocampus	104
List of Figures	107
List of Tables	109
Bibliography	111
Acknowledgements	127
Versicherung	129

ABBREVIATIONS

AIC Akaike information criterion

AICc corrected Akaike information criterion, also called small sample Akaike information criterion

AP anteroposterior

BrdU 5-bromo-2'-deoxyuridine

CI confidence interval

EdU 5-ethynyl-2'-deoxyuridine

ER evidence ratio

hpf hours post fertilization

LS Least squares

MCMC Markov chain Monte Carlo

ML Maximum-likelihood

PCNA Proliferating cell nuclear antigen

PCNA⁺ PCNA-positive

SOX2 sex determining region Y-box 2

SOX2⁺ SOX2-positive

SSE sum of squared errors

1. INTRODUCTION

1.1. CELL BEHAVIOR, MORPHOGENESIS AND GROWTH IN DEVELOPMENT AND REGENERATION

This year, the 100th anniversary of D'Arcy W. Thompson's *On Growth and Form* highlights the long-standing search for the principles that underlie the shaping of organisms. This question is tackled by the field of developmental biology, the science of understanding how the fertilized egg gives rise to an orderly body (Gilbert 2010). One of the ultimate goals is to understand human development, which includes to understand developmental failures. In turn, this understanding shall lead to progress in medical treatments. For example, the study of neurogenesis during development and homeostasis can lead to new treatments for neurodegenerative diseases. Another medically relevant subject is the study of regeneration, the reconstitution of lost body parts (Tanaka 2003). Recent advances in molecular biology and imaging allow the study of development in unprecedented detail. However, we still lack a full, quantitative, mechanistic understanding of how cells behave to shape tissues and let them grow.

Development was studied even long before D'Arcy W. Thompson. Hippocrates started to study development in the 15th century BC and Aristotle continued about 100 years later. Aristotle formulated the important concept of epigenesis according to which the structures of an embryo are created *de novo* during development (Wolpert et al. 2015). This concept was proven to be correct: After the discovery of the cell in the 17th century (Hooke 1665), Matthias Jakob Schleiden, Theodor Schwann and Rudolf Virchow, among others, formulated the cell theory which identified the cell as the basic unit of life (Schleiden 1838; Schwann 1839; Virchow 1858; Wolpert et al. 2015). They found that all living organisms consist of cells and that all these cells arise from previous cells. This turned the question of understanding development into questions of understanding cell behavior.

The same is true for regeneration. It is fascinating to observe that some animals can reconstitute lost body parts. For example, the fresh-water polyp hydra and the planarian flatworm regenerate into two individuals when cut into two pieces. Salamanders are

able to completely regenerate lost limbs or the tail (Murawala et al. 2012; Nacu and Tanaka 2011). Obviously, these processes involve tissue size and shape changes driven by the underlying cell behaviors. Again, to understand regeneration, an understanding of the underlying cell behaviors is needed.

Cell behaviors determining tissue shape and size are cell division, movements, differentiation, cell death as well as cell shape and size changes. But how does each cell know what to do? Individual cells become increasingly different from each other during development and the collective behavior of all the different cells forms the organism. In the late 19th century, research focused on the question how cells become different from each other. Starting with the works of August Weismann, Hans Driesch and many others, more than a century of following research now provides the basic principles to answer this question: Genes control the expression of proteins which in turn regulate cell behavior; gene expression is controlled by feedback loops involving intercellular signaling (Alberts 2015; Wolpert et al. 2015).

In turn, these cell behaviors lead to changes in tissue size and form. The detailed study of gastrulation, neural tube formation in vertebrates and wing disc development in *Drosophila* showed that all types of cell behavior are involved in tissue shape changes. (Etournay et al. 2015; Heisenberg and Bellaïche 2013; Oates et al. 2009; Wolpert et al. 2015). Now, how do those many, different cells behave exactly when they form and shape an organism? I aim to study this question in quantitative terms. The question can be broken down to three sub-questions: First, how does one measure and describe how the many cells in the developing embryo actually behave? Second, how can one measure and describe the complex shape and size of tissues and organisms as a whole, also taking into account the time course of shape and size? Third, what are the mechanisms that connect the observed cell behaviors to the observed growth and shaping of tissues and organisms?

Measuring how a single cell behaves is comparably easy. We can use a microscope to time-lapse image and measure where it is, how big it is, how it is shaped, when it divides and when it dies. Measuring when and how a cell differentiates is already more difficult as it involves measuring gene expression at single cell level as a function of time. But measuring the behavior of thousands of cells in the complex environment of the developing embryo is much harder. It is not generally possible to track each single cell in an organism although there are initial successes in time-lapsing whole organs or embryos at resolutions that do allow this (Currie et al. 2016; Etournay et al. 2015; Keller et al. 2008; Pantazis and Supatto 2014). In cases for which this is not possible, it may still be possible to infer cell behaviors by indirect experiments. But these experiments have to be designed according to the special situation one is interested in. Even if single cell tracks are available, the fact that there are thousands of cells makes it an intellectual challenge to generate knowledge out of such datasets. Several suggestions for how to describe cell behaviors in planar, epithelial tissues have been made (Blanchard et al. 2009; Bosveld et al. 2012; Etournay et al. 2016; Guirao et al. 2015). But a universal framework for measuring and describing the complex cell behavior in developing embryos is lacking

and an applicable strategy must be developed for each considered process.

The quantification of the complex shape and size of the organism is termed morphometrics (Prpic and Posnien 2016). It involves the rather easy measurement of the linear size of an organism in a certain direction but extends to the quantification of complex shapes with adequate mathematical formulations as proposed already by Thompson (1915). The time course of shape and size is of particular importance in development (Oates et al. 2009). Once again, a universal method for how to perform the quantification of shape and size does not exist but must be appropriately selected for the studied developmental process (Fruciano 2016; Prpic and Posnien 2016).

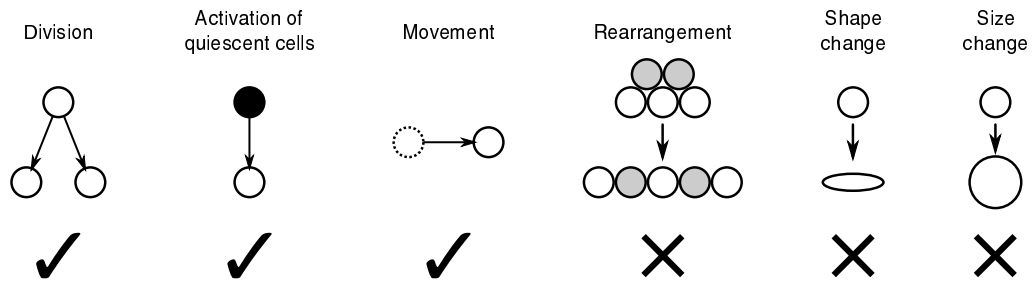
The question of how cell behavior leads to changes in form and growth ultimately involves the study of the involved forces. To understand the effects of these forces, the mechanism of morphogenesis is often studied with mathematical models (e.g. Bielmeier et al. 2016; Graner and Glazier 1992; Köhn-Luque et al. 2011). In special cases, e.g. if one can show that tissue size is proportional to cell number, it is possible to model the effects of cell behavior on growth without explicitly taking into account forces. Without a generally applicable theory that mechanistically couples cell behavior to morphogenesis and growth, suitable models must be developed for each developmental process at hand (Taber 2009).

Taken together, a generally applicable framework to measure and describe the behavior of the multitude of cells in a developing tissue is still lacking. To quantify tissue shape and size, appropriate observable must be selected for the studied developmental or regenerative process. Furthermore, the specific contribution of individual cell behaviors, and how exactly these cell behaviors collectively lead to the morphogenesis and growth of tissues are not clear for many developmental and regenerative processes. I worked on these problems for selected processes in development and regeneration (Figure 1.1). In the next section, I will introduce my specific topics.

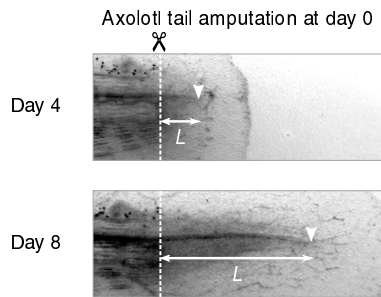
1.2. SPECIFIC TOPICS OF THE THESIS

Axolotl spinal cord and muscle regeneration: A particularly fascinating part of developmental biology is the study of regeneration, the ability of some species to rebuild lost body parts. In this thesis, I first investigate the regeneration of the spinal cord and muscle tissues after tail amputation in the Mexican salamander, axolotl (*Ambystoma mexicanum*). Specifically, I seek to find out how, when and where neural stem cells change their behavior in response to the injury. Furthermore, I want to identify the cell behaviors that are responsible for the tissue scale growth of the spinal cord. I compare this to the regeneration of the adjacent muscle segments. A better understanding of which cellular behaviors act when and where during regeneration and how they function to shape tissues will help to facilitate the search for the responsible molecular machinery. In turn, this will finally lead to the understanding of the whole process across all spatial scales.

A Cell behaviors



B Morphogenesis and growth



C Data-driven modeling

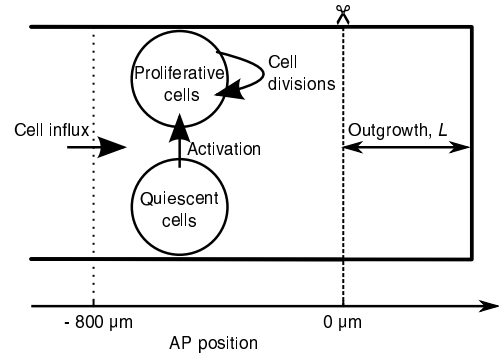


Figure 1.1.: The aim of this thesis was to study how cell behaviors shape selected tissues and let them grow during regeneration and development. This is exemplified by my study of axolotl spinal cord outgrowth during regeneration in chapter 3. **A:** Cell behaviors that could cause the outgrowth. My quantification of these behaviors showed that only division, activation and influx contribute to growth, as indicated by the check marks. **B:** The spinal cord grows after amputation. I quantified the outgrowth length, L , for 8 days after amputation. **C:** I developed a mathematical model of spinal cord outgrowth which uses the quantified cell behaviors as an input. The model correctly predicts the outgrowth and revealed cell cycle acceleration as the main driver of spinal cord outgrowth.

Development of muscle segments in zebrafish: Furthermore, it is an open question to what extent regeneration reuses developmental programs (Tanaka 2003; Tanaka and Ferretti 2009). Only a detailed characterization of both, development and regeneration, will allow answering this question. Accordingly, I also study development. For that, I keep investigating muscle tissue but I turn to the model organism zebrafish (*Danio rerio*). Its embryo facilitates the study of morphological shape changes and has already been used to extensively study muscle differentiation (Cortés et al. 2003; Currie and Ingham 1996; Daggett et al. 2007; Devoto et al. 1996; Henry and Amacher 2004; van Raamsdonk et al. 1978; van Raamsdonk et al. 1974a; Yin and Solnica-Krezel 2007). Zebrafish muscle segments take on a similar folded shape as the muscle segments in the regenerating axolotl tail. Previously, I proposed a mechanism involving cells that exert mechanical forces to organize the observed segment shapes (Rost 2010). Here, I quantify the segment shapes to test whether the proposed cellular behavior could drive the shaping of muscle tissue.

Neurogenesis in the adult human brain: Subsequently, I return to the study of the behavior of neural stem cells but turn to the hippocampus of the adult human brain. There, I refine the estimation of neuron turnover throughout life by contributing a better justified measurement error model to already published data and models (Spalding et al. 2013).

The tools I use throughout are the careful quantification of the involved processes, mainly by image analysis, and the derivation and application of mathematical models designed to make sense out of the data with the help of statistical inference. Being a physicist by training, I am inclined to the thesis, that the complex process of development can only be fully understood in the context of a quantitative, mathematical modeling framework (Oates et al. 2009). I view mathematical models as tools that can have very different purposes. Therefore, the next section shall introduce the role of mathematical modeling for investigating development and regeneration.

1.3. DATA-DRIVEN MATHEMATICAL MODELS IN DEVELOPMENT AND REGENERATION

Mathematical modeling is used in many fields of biology (Chara et al. 2014; Edelstein-Keshet 2005; Getto and Marciniak-Czochra 2015; Murray 2002). The use of mathematics has for instance been successful in physiology, ecology and systems biology and evolution (Edelstein-Keshet 2005; Keener and Sneyd 1998; Murray 2002). After the early efforts of D'Arcy W. Thompson using mathematics to describe development, the first successful, mechanistic models in developmental biology were on pattern formation, i.e. how do cells become different from each other in the developing embryo.

In his French flag model, Wolpert (1969) proposed a morphogenetic gradient encoding positional information. This positional information can be read by cells and hence cells can differentiate according to their position in the embryo. Crick (1970) proposed the diffusion of a molecule, termed morphogen, through the embryo would be a likely physical mechanism underlying the formation of the morphogenetic gradient. Although this model could not be proven immediately as the molecular players were unknown, it highlights an important use of mathematical models: They can be used to qualitatively understand a mechanism. Later, the model was proven for *Drosophila* development by identifying bicoid as an involved morphogen (Driever and Nüsslein-Volhard 1988).

Pattern formation was also the topic that Alan M. Turing, Alfred Gierer and Hans Meinhardt worked on, using reaction-diffusion systems (Gierer and Meinhardt 1972; Turing 1952). Their works feature mathematical models that predict a non-intuitive mechanism for the formation of spatial patterns that takes into account chemical reactions and diffusion of the reactants. A main result of Gierer and Meinhardt (1972) and Turing (1952) was qualitative one: Their models are able to self-organize patterns and this works for a whole range of model parameters. Hence, it gave a possible solution for the long-standing question how patterns can be generated out of uniform, unpatterned initial conditions (Kondo and Miura 2010; Nicolis and Wit 2007).

Nonetheless, already Hans Meinhardt noted that proving the existence and relevance of this pattern formation mechanisms would include identifying the involved molecules and measuring their properties (Gierer and Meinhardt 1972; Maini et al. 2017). This highlights another use for mathematical models: They can be used to formally formulate a mechanism in quantitative terms; solving the model then leads to predictions that can be tested against quantitative data. This approach is very successful nowadays (Chickarmane et al. 2010; de Back 2015; Etournay et al. 2015; Oates et al. 2009; Roeder et al. 2011; Sasai 2013). The common view is that quantitative data, which is generated by imaging and subsequent image analysis, can be tested against model predictions. If the data contradict the model predictions, the model needs to be refined until the model predictions are validated (Bonner 1974; Chickarmane et al. 2010; de Back 2015; Roeder et al. 2011; Sasai 2013). From the validated model, predictions for new experiments can be made to further refine our understanding.

However, this comparison of model prediction and experimental data can be difficult (Swigon 2012). Depending on the context, low amount of data and high levels of noise in the data may lead to the need of carefully employing the correct statistical inference methods to properly perform the test of model predictions against the data (Sasai 2013; Swigon 2012). Luckily, there already exists a wealth of statistical methods to choose from. Depending on the problem at hand, one may employ frequentist methods (namely the methods of Maximum-likelihood (ML), Least squares (LS) and bootstrapping) and the Bayesian method. Statistical inference methods allow estimating unknown parameters by fitting a model to the data. Furthermore, fitting the model allows accessing how well the model describes the data. One might reject a hypothesis if even the best fitting model does not describe essential features of the data. Especially, if there are two

competing hypotheses available, model selection criteria can be used to select the best model and avoid overfitting. These model selection criteria, like the Akaike information criterion (AIC) used in this thesis, give a quantitative score that rewards well fitting models while penalizing overly complex models. This score can be used to rigorously select the best model from a set of alternatives.

The application of statistical inference methods is not new to biology. For instance, in the field of systems biology these methods are actively applied and developed to understand gene regulation (Kreutz et al. 2007; Raue et al. 2013). The challenge in applying these methods in developmental biology is to identify observables for which data of sufficient quality are available to answer relevant questions.

Let me sketch this with an example: Imagine, you want to measure the cell cycle length of cells in a developing tissue. Seemingly, the easiest way would be to keep track of all cells and measure the time between consecutive cell divisions with a watch. However, as stated above, this is generally not yet possible for all developing tissues nowadays. Hence, one has to find other data to infer the rate indirectly. One possibility are continuous label incorporation assays in which newly synthesized DNA is marked with nucleotide analogues (Lefevre et al. 2013; Nowakowski et al. 1989; Spalding et al. 2005). Intuitively, the label will be incorporated into DNA faster if cells divide faster. However, only with the help of a mathematical model that relates the label incorporation speed at the population level with the cell cycle length, these data can be used to infer the cell cycle length at the cellular level.

Hence, the availability of data dictates what kind of model is useful to answer the question. I call these models which are designed to answer relevant questions given the possibly available data 'data-driven' models. Throughout this thesis, I will define several such models to answer questions concerning cell behavior, tissue shaping and growth.

1.4. STRUCTURE OF THE THESIS

I describe the methods I use in chapter 2. Starting with statistical inference methods, I will first focus on how parameters can be estimated by model fitting. Then, I will discuss model selection. There, the idea is: If there are two competing models to explain the same experimental data, we want to find the model which explains the data best while trying to avoid selecting an overly complicated model. Then, I go on to explain the numerical tools I used to implement those methods and briefly explain how I performed image analysis.

Chapter 3 on axolotl tail regeneration is the most extensive one of the thesis. It's based on my contributions to Rodrigo Albors et al. (2015), Rost et al. (2016a), and Vincent et al. (2015). There, I ask what the underlying cellular behaviors are that drive the regenerative spinal cord outgrowth after tail amputation. After quantifying the spinal cord outgrowth, I present a first mathematical model that assumes proliferation as the only driver of the outgrowth. Comparing different hypotheses for how the proliferation

response is regulated in space and time, I will find that a model involving a biphasic proliferation response, initially slow and accelerated from about 3 days after amputation could explain the outgrowth well. To test this prediction, I will quantify the contributions of all possibly involved cellular mechanisms. Particularly, I make use of neural stem cell density measurements (Rodrigo Albors et al. 2015) to show that convergence and extension is negligible. I make use of cell proliferation-related measurements along the anteroposterior (AP) axis of the spinal cord (Rodrigo Albors and Tanaka 2015) to identify a high-proliferation zone that extends 800 μm anterior to the amputation plane, and calculate changes in cell cycle kinetics within this zone. By measuring the displacement of sparsely-labeled cells, I also establish the cell influx into the regenerating spinal cord. Subsequently, I set up a mathematical model of spinal cord outgrowth that incorporates cell proliferation, stem cell activation and cell influx. Using this model, I show that cell influx and quiescent stem cell activation are of minor importance, but that the acceleration of the cell cycle in the high-proliferation zone is the major driver of the regenerative spinal cord outgrowth, indeed. Finally, I demonstrate how the same model ideas can be applied to understand the regulation of cellular mechanisms in perturbed regeneration conditions. I compare the identified zone length and the growth mode to the regeneration of the adjacent muscle tissue.

In chapter 4 which is based on my contributions to Rost et al. (2014), I examine the shaping of muscle segments during development in zebrafish. Those segments take on a similar folded shape as the muscle segments in the regenerating axolotl tail. I start with a literature review revealing four hypotheses for the mechanism that shapes the segments. However, for neither of the four hypotheses exists conclusive experimental support. Therefore, I use time-lapse movies of developing zebrafish embryos to quantify the dynamics of muscle segment shape. By comparing such time courses with the start of movements in wildtype zebrafish and analyzing immobile mutants, I show that the previously implicated body movements do not play a role in shape formation. Further, the spatial pattern of final segment shape constrains or rules out possible contributions by other previously proposed mechanisms. Contrary to previous suggestions, I show that a particular cell type, the muscle pioneer, is not required for initial shape formation. Finally, I test the tension-and-resistance mechanism that I proposed in my diploma thesis (Rost 2010). This mechanism involves interactions between intra-segmental tension, possibly due to a particular cell differentiation pattern, and segment boundaries. To evaluate this mechanism, I derive and analyze a mechanical model. The predictions of this model are validated by comparison with experimental data. Altogether, my results support the notion that a simple physical mechanism suffices to self-organize the observed spatiotemporal pattern in muscle segment formation.

Chapter 5 is again concerned with the behavior of neural stem cells. There, I refine the estimation of neuron turnover rates in a part of the adult human brain, the hippocampus. It is based on the data and the mathematical model developed by Spalding et al. (2013). I extend their statistical analysis. My results mainly corroborate previous results, but I find that the rate of neuron turnover in the adult human brain might be even higher than

currently thought.

Chapters 3 to 5 are written such that they can be read on their own. Each of these chapters includes a dedicated introduction and discussion section for the specific topic. In chapter 6, I briefly summarize the main results from chapters 3 to 5. Furthermore, I comment on the different ways mathematical models are used in this thesis and propose which models should be developed in the future.

My approach of combining quantitative data, mathematical models and statistical inference is inherently an interdisciplinary one involving both, biology and mathematics. All biological data used in this thesis are published already. Not being an experimentalist myself, I will explain the important features of the data but I will also refer to the published protocols and methods when describing concrete datasets. When it comes to mathematics, I will attempt to explain the reasoning and assumptions that lead to the equations such that it is possible to follow the line of argument without having to go through the calculations in detail.

2. METHODS

2.1. STATISTICAL INFERENCE

In developmental biology, as in any other natural science, we observe nature and state hypotheses about the processes that underlie our observations. Useful hypotheses lead to predictions that can be tested against experiments. Sometimes, it is necessary or helpful to formalize hypotheses into mathematical models that generate quantitative predictions. These predictions can be tested against quantitative data. Statistics is the mathematical field that deals with these tests.

Furthermore, statistical inference can be used to deduce information about underlying processes by data analysis. In this thesis, I am mainly confronted with two types of situations: Either, I formulate a hypothesis in terms of a mathematical model but some model parameters are unknown. Then, I can use parameter estimation methods to infer unknown parameters by fitting model predictions to measured data. This allows me to do two things: First, it is a self-consistency check. If even the best-fitting model is inconsistent with the data, the hypothesis is rejected. Second, if the model fits the data well, the estimated parameters give additional information about the underlying process or can be used to summarize the data.

Or, in other situations, I formulate competing hypotheses in terms of different mathematical models. Then, I can use model selection methods to decide what the best-fitting model among the competing models is.

Below, I introduce the statistical inference methods I used in this thesis. For more extended background see, e.g. Burnham and Anderson (2002), Olive et al. (2014), and Press et al. (1996).

2.1.1. LIKELIHOOD

The concept of likelihood is most important for statistical inference. Given some measured data, the likelihood is a quantitative measure that tells how likely a certain hypothesis is. The likelihood function is used for parameter estimation and model selection.

Hence, I briefly explain the mathematical concept here.

Mathematical models for a biological process can either be probabilistic or deterministic. However, models for measured data are always probabilistic. Even, if the biological process is deterministic, the model for the data has to include the measurement process which always introduces random measurement errors (Hilborn and Mangel 1997). Hence, the model for the biological data which includes the biological process and the measurement always is a probabilistic model.

To define the likelihood function, let us consider that we formalized a hypothesis into a probabilistic mathematical model. This model shall be fully described with the k parameters p_1, \dots, p_k . Furthermore, the obtained data shall be described by the abstract vector x . This vector could for instance contain multiple measurements of the same observable or the time course of an observable. Then, the probabilistic model for the data defines a probability $P(x|p_1, \dots, p_k)$ to obtain the data x for the given parameters p_1, \dots, p_k . If this probability, $P(x|p_1, \dots, p_k)$ is treated as a function of the parameters p_1, \dots, p_k for given, fixed data x , then this function is called likelihood. It is often written as

$$\mathcal{L}(p_1, \dots, p_k) = P(x|p_1, \dots, p_k). \quad (2.1)$$

It is often convenient to use the logarithm of the likelihood function in mathematical calculations. The logarithm of the likelihood function, $\log \mathcal{L}$, is called log-likelihood.

Often, normally distributed measurement errors are assumed for deterministic models. Let us write the possibly time-dependent, deterministic model as $\tilde{x}(t; p_1, \dots, p_k)$, where t is the time. Further, the data, x , shall be given by the measurements x_1, \dots, x_n at times t_1, \dots, t_n , respectively. Then, the log-likelihood for this deterministic model with normally distributed measurement errors, $\sigma_1, \dots, \sigma_n$, is given by (Burnham and Anderson 2002):

$$\ln \mathcal{L}(p_1, \dots, p_k; \sigma_1, \dots, \sigma_n) = -\frac{1}{2} \sum_{i=1}^n \left(\frac{\tilde{x}_i(t_i; p_1, \dots, p_k) - x_i}{\sigma_i} \right)^2 + \sum_{i=1}^n \ln \left(\frac{1}{\sqrt{2\pi}\sigma_i} \right), \quad (2.2)$$

and under the assumption of uniform $\sigma = \sigma_i$ it becomes

$$\ln \mathcal{L}(p_1, \dots, p_k, \sigma) = -\frac{1}{2} \sum_{i=1}^n \left(\frac{\tilde{x}_i(t_i; p_1, \dots, p_k) - x_i}{\sigma} \right)^2 + n \ln \left(\frac{1}{\sqrt{2\pi}\sigma} \right). \quad (2.3)$$

2.1.2. PARAMETER ESTIMATION

FREQUENTIST APPROACH: MAXIMUM-LIKELIHOOD AND LEAST-SQUARES METHOD

Maximum-likelihood (ML) method: The frequentist approach to statistical inference interprets probability as the frequency of the outcome of a repeatable experiment. A commonly used frequentist method is the method of Maximum-likelihood (ML). In this approach one estimates the parameters of a model by maximizing the likelihood, eq. (2.1). Hence, this procedure gives the parameters for which the measured data

would be most likely. The maximization of the likelihood is often done numerically. I describe the numerical methods I used in section 2.2. I apply the ML method for the analysis of spinal cord outgrowth data in section 3.2.2 (Figure 3.6), for the analysis of continuous 5-bromo-2'-deoxyuridine (BrdU)-labeling data in section 3.2.4 (Figure 3.11A) and to estimate neuron turnover rates in section 5.2.1 (Figure 5.2).

Method of Least squares: The method of Least squares (LS) is another approach for parameter estimation. It coincides with a special case of the ML method, namely for the case of normally distributed measurement errors and known variances of the errors, σ_j^2 . Then, maximization of eq. (2.2) becomes equivalent to minimizing

$$SSE = \sum_{i=1}^n \left(\frac{\tilde{x}_i(t_i; p_1, \dots, p_k) - x_i}{\sigma_i} \right)^2, \quad (2.4)$$

where SSE is the sum of squared errors. The difference, $\tilde{x}_i(t_i; p_1, \dots, p_k) - x_i$, is the shortest distance between model and data when both are plotted. Therefore, the method can alternatively be derived graphically. However, in this thesis, I always use it in the sense of a special case of the ML method. I apply the LS method for the analysis of continuous BrdU-labeling data in section 3.3.1 (Figure 3.17) and for summarizing muscle segment shape changes with an empirical model in sections 2.2.2 and 4.2.2 (Figures 4.2 and 4.3)

Confidence intervals and profile likelihood: The maximization of the likelihood only gives a point estimate for the parameters. However, due to the probabilistic nature of the method this estimate may not properly reflect the true parameters of the underlying process. Therefore, it is important to also estimate the uncertainty of the estimated parameter values. For that purpose, the confidence intervals (CIs) are reported. The CI of a parameter is always connected with a confidence level. The confidence level states the probability, that the parameter is found in the corresponding CI.

Under fairly general conditions, the CIs for the fitted parameters can be inferred by shifting the parameter of interest from the optimal value while fitting the remaining parameters; this generates a log-likelihood profile. For instance, the 95% CI is then given by the positions where the log-likelihood decreases by $\Delta \ln \mathcal{L} = 1.92$ (Olive et al. 2014). I use this method to estimate parameter confidence intervals in section 3.2.2, section 3.2.4, section 3.3.1 and section 5.2.1 (Figures 5.3 and 5.4).

BAYESIAN APPROACH

In the Bayesian approach to statistical inference, probability is not only associated with the data but also with the value of parameters (Olive et al. 2014). In this approach, a prior, $\pi(p_1, \dots, p_k)$, has to be specified before data is analyzed. This prior is a probability distribution that reflects the so called 'degree of belief' about what the possible values

for these parameters are before the experiment. This 'degree of believe' reflects prior knowledge but a subjective choice of the analyst is always involved. Now suppose, we measured some data, x , and we have a probabilistic model for that data, characterized by a likelihood (Equation (2.1)). In turn, the model depends on the parameters p_1, \dots, p_k . Then, the Bayes theorem allows the estimation of parameter values by means of a posterior $p(p_1, \dots, p_k|x)$. This posterior again is a probability distribution which combines the information on the parameter values we had before the experiment (the prior) and the information contained in the measured data (the Likelihood):

$$p(p_1, \dots, p_k|x) = \frac{P(x|p_1, \dots, p_k)\pi(p_1, \dots, p_k)}{\int P(x|p'_1, \dots, p'_k)\pi(p'_1, \dots, p'_k)dp'_1, \dots, dp'_k} \quad (2.5)$$

The full specification of the posterior, $p(p_1, \dots, p_k|x)$, then allows giving point estimates for the true parameter values, for instance by reporting the mode of the posterior. Also, credibility intervals can be constructed. Such intervals contain the true parameter value with a certain probability and can be used to reflect the uncertainty of a parameter estimate, similar to CI calculated with the ML method.

Solving eq. (2.5) often is not possible analytically. Even numerical solutions can be challenging and therefore Markov chain Monte Carlo (MCMC) methods are applied (for instance with the numerical tool PyMC described in section 2.2.2).

As noted above, the choice of priors is a subjective choice of the analyst. However, if the data is of sufficient quality to constrain the model parameters the result of the parameter estimation will be insensitive to reasonable variations of the prior. This method is applied in section 3.2.4 for the detection of a high-proliferation zone during axolotl spinal cord regeneration (Figure 3.10).

BOOTSTRAPPING

The bootstrapping approach for parameter estimation bypasses the need for the specification of a likelihood. It's based on the following idea: We make a point estimate for a parameter from some data, for example by using the LS method. Now, assume that we would repeat the experiment very often, say N times, and get a point estimate for each experiment. Then, it is reasonable to assume that the N obtained point estimates are scattered around the true value of the parameter. However, the repetition of the experiment is often too expensive.

Therefore, the repetition of the experiment is simulated with the bootstrap method (Press et al. 1996). New, synthetic data are generated by drawing from the actual data with replacement. Then, for each synthetic data the point estimate for the parameter is performed. This procedure is repeated very often, typically more than 1000 times. From the set of point estimates one can report the mean and standard deviation as an estimate of the true parameter and the associated uncertainty. I used the bootstrapping method for estimating the confidence belt of the model prediction for spinal cord outgrowth in section 3.2.5 (Figures S6 and 3.14) and for estimating the confidence interval of the

model for summarizing muscle segment shape changes in section 4.2.2.

2.1.3. MODEL SELECTION: AKAIKE INFORMATION CRITERION

During my work, I was confronted with situations in which I formulated multiple hypotheses to explain certain experimental data. These hypotheses could be translated to different mathematical models (see sections 3.2.2 and 5.2.1). Then, I aimed to find the best model in the sense of which model fits the data best while not being overly complex. To do so, I used an information theoretic approach for model selection based on the Akaike information criterion (AIC) first formulated by Akaike (1974).

The AIC is a score for each model under consideration and is given by:

$$AIC = 2k - 2 \ln \mathcal{L}. \quad (2.6)$$

The formula for the AIC involves the maximum-likelihood, \mathcal{L} , of the model and the number of parameters, k . The AIC gets smaller the bigger the maximum-likelihood, i.e. it fits the data better. But it gets bigger the more parameters are used for that model, i.e. the more complex a model is. Then, the model with the lowest AIC might be termed the best model or best approximating model among the candidate models (Burnham and Anderson 2002).

For low amount of data, Burnham and Anderson (2002) suggest to use the corrected Akaike information criterion (AICc) instead of the AIC which is given by:

$$AICc = 2k - 2 \ln \mathcal{L} + \frac{2k(k+1)}{n-k-1}, \quad (2.7)$$

where n is the number of data points.

To judge how much more likely the best model is compared to the other candidate models, one can calculate the evidence ratio (ER). To do so, one first calculates the AICc differences which are defined as

$$\Delta_i = AICc_i - AICc_{min}, \quad (2.8)$$

where $AICc_i$ is the AICc of model i and $AICc_{min}$ is the lowest AICc among the i models. Then, the evidence ratio, ER , of model i is defined as

$$ER = e^{\frac{1}{2}\Delta_i}. \quad (2.9)$$

If the evidence ratio, $ER > 100$ for a pair of candidate models, then there is essentially no empirical support for the worse model. Then it is safe to say that the model with the lowest AICc is the best model among the candidate models. The AIC is used for model selection in sections 3.2.2 and 5.2.1.

2.1.4. STATISTICAL NOMENCLATURE

If not stated otherwise, measurements are reported as mean \pm standard error of the mean. In the figures * denotes $p < 0.05$ and ** denotes $p < 0.01$ for the respective test as indicated in the figure caption.

2.2. NUMERICAL METHODS

2.2.1. MODEL SIMULATION

Most numerical model simulations were implemented with python (Millman and Aivazis 2011; Oliphant 2007) (RRID:SCR_008394).¹ Where relevant, the source code is provided online in Jupyter notebooks (<http://jupyter.org/>). The corresponding URLs are mentioned as footnotes throughout the thesis. For reproduction of my results the python distribution Anaconda (<https://www.continuum.io/>) can be used. Along with the source code, I provide environment.yml files that specify the python environments that are needed for running my code in the online repositories.

For some models a first prototype was implemented in Morpheus (Quintero et al. 2012; Starruß et al. 2014) (RRID:SCR_014975). The overdamped dynamics of the mechanical model of chevron formation (see section B.1) were numerically solved with Wolfram Mathematica (RRID:SCR_014448)

2.2.2. STATISTICAL INFERENCE

For the optimization of the likelihood (Equation (2.1)) or the sum of squared errors (Equation (2.4)), I used the optimization algorithm MIGRAD from the python module iMinuit (<https://github.com/iminuit/iminuit>). I always tried multiple initial values for the fitting to confirm that the algorithm converged to a global minimum. I calculated the CI either with MINOS from iMinuit, which implements the profile likelihood procedure described above or approximated the CI with the parabolic approximation as implemented in iMinuit. For Bayesian parameter estimation, I made use of the python module PyMC (Patil et al. 2010).

PARAMETER ESTIMATION FOR EMPIRICAL MODEL OF CHEVRON ANGLE TIME COURSE

I considered all segments for which more than 80% of the data points fulfilled $\alpha_{mean} - \Delta\alpha \leq 0$ as non-chevron-forming segments (see fig. 4.2C). For the remaining segments I fitted the data for each chevron-forming segment with the piecewise linear function (Section 4.2.2). Hence, I describe the chevron formation of these segments with the 3 parameters of the piecewise linear function: Chevron formation start and end times,

¹Research Resource Identifiers (RRIDs) can be looked up on <https://www.scicrunch.org/resources>

t_{start} and t_{end} , respectively, and a final chevron angle α_{end} that is reached after chevron formation ceased. I determined the fit parameters and their confidence intervals using the bootstrap method (see section 2.1.2). For each segment, I calculated random samples of α for each time point using the Gaussian distribution defined by α_{mean} and $\Delta\alpha$. I generated $N = 100$ random data sets from the measured data for each segment and fitted each data set with the piecewise linear function. Thus, for each of the 3 parameters, I get N realizations from which I can calculate the means, t_{start} , t_{end} , α_{end} , and the standard deviations, Δt_{start} , Δt_{end} , $\Delta\alpha_{end}$.

Fitting was done with a grid search using each parameter triple generated from all possible combinations of

$$\begin{aligned} t_{start} &\in (t_{min}, t_{min} + 10 \text{ min}, \dots, t_{max}), \\ t_{end} &\in (t_{min}, t_{min} + 10 \text{ min}, \dots, t_{max}), \\ \alpha_{end} &\in (-1.0 \text{ rad}, -0.95 \text{ rad}, \dots, 1.4 \text{ rad}) = (-57^\circ, -54^\circ, \dots, 80^\circ), \end{aligned}$$

where t_{min} is the formation time of the current segment boundary and $t_{max} = 740$ min. Then the parameter combination with the minimal sum of squared residuals was chosen.

I considered fitting results insignificant if parameter uncertainties were too high. The criteria I chose for significance are:

$$\begin{aligned} \Delta\alpha_{end} &< 6^\circ, \\ \Delta t_{start} &< 60 \text{ min}, \\ \Delta t_{end} &< 120 \text{ min}. \end{aligned}$$

Furthermore I also considered fits invalid if the end of chevron formation might not have been in the observed period:

$$t_{end} + 2\Delta t_{end} > t_{max}.$$

I considered only segments with significant fitting results as chevron-forming segments, whereas I ignored the results for other segments and treated them as missing data.

2.2.3. DATA ANALYSIS

Furthermore, I used the python modules Bokeh (<http://bokeh.pydata.org>), iMinuit (<http://github.com/iminuit/iminuit>), matplotlib (Hunter 2007), ipycache (<http://github.com/rossant/ipycache>), Numba (<http://numba.pydata.org/>), NumPy (Walt et al. 2011), pandas (McKinney 2010), probfit (<http://github.com/iminuit/proffit>), seaborn (Waskom et al. 2016), SciPy (Jones et al. 2001) and uncertainties (<http://pythonhosted.org/uncertainties/>) for data analysis. Again, the source code is

provided online and corresponding URLs are mentioned as footnotes throughout the thesis.

2.3. IMAGE ANALYSIS

Image analysis was performed with Fiji (RRID:SCR_002285) (Schindelin et al. 2012) and AxioVision (RRID:SCR_002677). In particular, axolotl spinal cord outgrowth was measured with the line tool in Fiji (see figs. S1 and 3.4). Trajectories of single cell clones were measured with AxioVision (see fig. 3.13). The shape of muscle segments in the developing zebrafish was quantified as described below.

2.3.1. ANGLE MEASUREMENTS TO QUANTIFY CHEVRON FORMATION

I analyzed time-lapse movies of chevron formation during zebrafish development at 28 °C which were acquired in previous studies (Herrgen et al. 2009; Schröter et al. 2008) using embryos from incrosses of free spawning heterozygous *nic^{b107}* parents (Westerfield et al. 1990) (see fig. 4.2). The movies show the period from before the 1-somite stage until about the 30-somite stage. Frame rate was every 5 minutes. The embryos are visible in lateral view (Movies 1,2 in supplementary material to Rost et al. (2014)). The formation of segment 1 was not always clearly detectable in the time-lapse movies. Therefore, I chose to set the time of the clearly detectable formation of segment 6 to 115 min for each individual movie, such that the average time point of the formation of segment 1 is $t = 0$ (Movies 1,2 in supplementary material to Rost et al. (2014)).

To quantify the shape of the chevron, I manually measured the angle between the posterior dorsal segment boundary and the notochord, γ , for successive time points using the angle tool in the Fiji package (Schindelin et al. 2012) (Figure 4.2A,B). Assuming a simplified geometrical relation that neglects notochord curvature I calculated angles α , the angles between the dorsal segment boundary and the dorso-ventral axis marked by the dorsal boundary of the notochord (Figure 4.2B), from all measured angles γ :

$$\alpha = 90^\circ - \gamma.$$

The angles α will be used for further analysis because they are easier to compare to the mechanical model presented in section 4.3.3. I determined averages α_{mean} and standard deviations $\Delta\alpha$ for a small number of segments by repeated manual evaluation of γ (data not shown). Low contrast frames and intermittent occurrence of U-shaped contours left some uncertainty in the measurements. To decrease the number of measurements, I approximate the averages α_{mean} and standard deviations $\Delta\alpha$ by only measuring the two extreme angles γ_{min} and γ_{max} (Figure 4.2A). I define

$$\alpha = \frac{\alpha_{max} + \alpha_{min}}{2}, \quad (2.10)$$

where α_{max} and α_{min} are calculated from the angles γ_{min} and γ_{max} , respectively (Figure 4.2A). For the tested segments, α approximates the average of repeated measurements, α_{mean} (data not shown). To estimate the measurement error, I assumed the probability distribution for picking the true value α_t to be a normal distribution around α_{mean} . Repeated manual evaluation of the likely angle α from the same image fell within the interval ($\alpha_{min}, \alpha_{max}$) in more than 95% of cases. Therefore, following the three-sigma rule, the standard deviation of the Gaussian is given by

$$\sigma = \frac{1}{2}\Delta\alpha = \frac{1}{2} \frac{\alpha_{max} - \alpha_{min}}{2}.$$

3. REGENERATION OF SPINAL CORD AND MUSCLE SEGMENTS IN AXOLOTL

3.1. INTRODUCTION

The Mexican salamander (*Ambystoma mexicanum*), commonly known as axolotl, is uniquely able to fully regenerate a functional spinal cord after tail amputation (Tanaka and Ferretti 2009). Why it can do this while other vertebrates only have limited regenerative capacity is a question of great interest (Tanaka 2003). Especially, in the context of regenerative medicine one can hope that understanding axolotl spinal cord regeneration will help to better treat spinal cord injuries in humans. Of course, this regeneration process can only be fully understood taking into account the molecular, cell and tissue scale.

Here, I will first focus on understanding which cell behaviors lead to spinal cord outgrowth. I will show that while cell influx and neural stem cell activation play a minor role, the acceleration of the cell cycle is the major driver of regenerative spinal cord outgrowth in axolotls. Furthermore, I will find that the length of the zones of activated cells are similar for spinal cord and muscle tissue. Let me start by shortly reviewing the morphology of the axolotl spinal cord and important facts about how it regenerates. Then, I sketch my quantitative analysis strategy before presenting Results (Sections 3.2 and 3.3), Discussion (Section 3.4) and Conclusion (Section 3.5).

My own work as presented in this chapter has contributed to the three articles Rodrigo Albors et al. (2015), Rost et al. (2016a), and Vincent et al. (2015). Additional results which were mainly obtained by my co-authors are not included here.

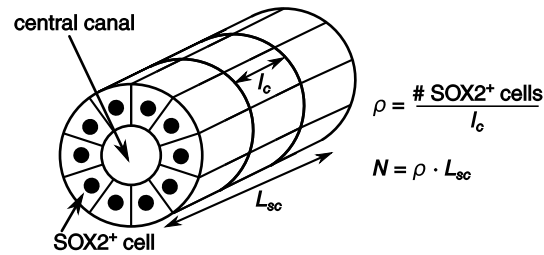


Figure 3.1.: An idealized scheme of the tube-like structure of the spinal cord stem cells during regeneration. The neuronal stem cells form a single layered epithelium around the fluid-filled central canal. The density of SOX2-positive (SOX2⁺) cells along the AP axis, ρ , is the ratio of the number of SOX2⁺ cells per cross section (# stem cells) and the mean AP cell length, l_c . The density of SOX2⁺ cells along the AP axis can also be understood as the proportionality constant between the total number of stem cells in a zone along the spinal cord with zone length, L_{sc} .

3.1.1. MORPHOLOGY OF THE SPINAL CORD

The spinal cord of vertebrates can be thought of as a tube-like structure along the AP axis (Figure 3.1). A fluid filled lumen, the central canal, that runs along the whole length of the spinal cord is surrounded by the gray matter. The gray matter contains ependymal cells, neurons and astrocytes. The gray matter is then surrounded by the white matter which contains ascending and descending fibers and oligodendrocytes (Chernoff et al. 2003; Rodrigo Albors 2014; Tanaka and Ferretti 2009). Different from many other vertebrates the ependymal cells in the axolotl spinal cord retain radial glia-like features such as the expression of the stem cell marker sex determining region Y-box 2 (SOX2) (Mchedlishvili et al. 2012; Rodrigo Albors 2014) (Figure 3.2). Radial glia cells are stem cells of the developing nervous system (Rodrigo Albors 2014). Hence, the ependymal cells in the axolotl are also termed neural stem cells (Tanaka and Ferretti 2009).

3.1.2. SPINAL CORD REGENERATION

Upon tail amputation the axolotl regenerates a fully functional spinal cord. The spinal cord starts to grow as a single-layered epithelium consisting of neural stem cells (Mchedlishvili et al. 2007; Rodrigo Albors 2014; Rodrigo Albors and Tanaka 2015). During an early period of growth the stem cells do not differentiate (Rodrigo Albors et al. 2015; Zhang et al. 2003). The length of this period is in the order of at least one week and is probably similar in axolotl (Arsanto et al. 1992; Rodrigo Albors 2014; Zhang et al. 2003). Only after this initial growth, differentiation of the stem cells into neurons sets in (Mchedlishvili et al. 2007; Tanaka and Ferretti 2009). Furthermore, neurons do not dedifferentiate (Zhang et al. 2003). I will focus on the early period before differentiation into neurons sets in. Grafting experiments showed that the regenerated spinal cord stems from a zone spanning at least 500 μm adjacent to the amputation site (Mchedlishvili et al. 2007). This zone has

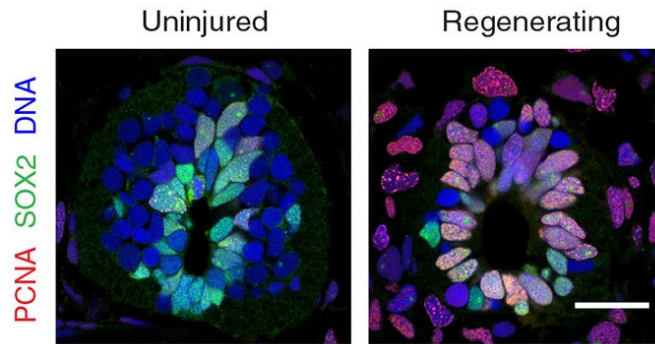


Figure 3.2.: Spinal cord cross sections of an uninjured and regenerating spinal cord at day 6 after amputation. Merge of a staining for DNA with Hoechst (blue), SOX2 (green) and Proliferating cell nuclear antigen (PCNA) (red). Scale bar, 50 μm .^a

^aReprinted from A. Rodrigo Albors et al. (2015). Planar Cell Polarity-Mediated Induction of Neural Stem Cell Expansion during Axolotl Spinal Cord Regeneration. *eLife* 4, e10230. DOI: 10.7554/eLife.10230, Fig. 2.

been termed progenitor zone (Figure 3.3) (Mchedlishvili et al. 2007; Rodrigo Albors 2014).

Single cell tracking experiments showed that proliferation of stem cells is involved in spinal cord growth during regeneration (Mchedlishvili et al. 2007; Zhang et al. 2003). Proliferation is distributed relatively homogeneous along the spinal cord (Holtzer 1956; Mchedlishvili et al. 2007). Knock-out or knock-down of SOX2 impedes proper spinal cord growth and also impedes the proliferation of stem cells (Fei et al. 2014). This suggested that proliferation is necessary for proper spinal cord regeneration. As SOX2 knock-out cells are still able to proliferate Fei et al. (2014) also suggested that an acceleration of the cell cycle is needed for correct spinal cord growth during regeneration. However, it has not been studied yet whether other cell behaviors like cell movements and rearrangements are also involved in the observed tissue growth.

3.1.3. QUANTITATIVE ANALYSIS STRATEGY

In this chapter I ask, what are the underlying cell behaviors that drive the regenerative spinal cord outgrowth during the first 8 days after tail amputation. First, I will quantify the spinal cord outgrowth in section 3.2.1. Then, I present a first naive model that assumes proliferation as the only driver of the outgrowth (Section 3.2.2). I'll compare different hypotheses for how the proliferation response is regulated in space and time with statistical inference methods. I will find that a model involving a biphasic proliferation response, initially slow and accelerated from about 3 days after amputation could explain the outgrowth well. This puts forward the idea that the acceleration of the cell cycle in a zone close to the amputation plane could be the major driver of the outgrowth.

To test this hypothesis, I first inspect which other cellular mechanisms like directed cell migration, convergence and extension movements, cell (de-)differentiation and cell death

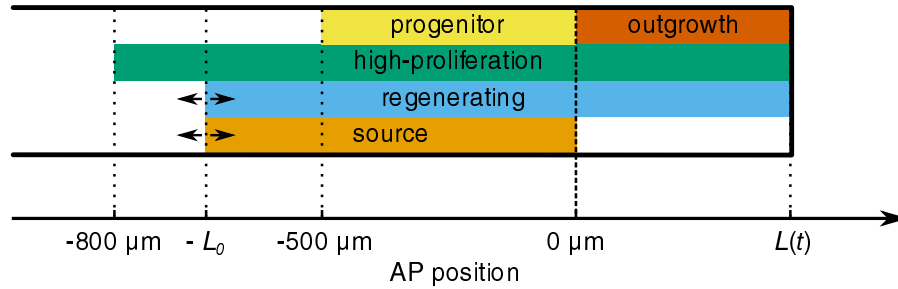


Figure 3.3.: The sketch shows the definition of spatial zones along the AP axis of the axolotl spinal cord as used in this thesis. Along the AP axis various positions are marked, anterior is to the left. $0 \mu\text{m}$ marks the amputation plane. $L(t)$ marks the tip of the spinal cord, hence $L(t)$ corresponds to the current outgrowth. The progenitor zone spans from $-500 \mu\text{m}$ to the amputation plane. As pointed out in section 3.1.2 experimental evidence suggests that the outgrowth stems from this zone. The high-proliferation zone spanning from $-800 \mu\text{m}$ to the tip, $L(t)$, is found in section 3.2.4. For the mechanistic models of spinal cord growth presented in sections 3.2.2 and 3.2.5 a source zone spanning from a position $-L_0$ to the amputation plane will be defined. The position $-L_0$ will coincide with $-800 \mu\text{m}$ or $-500 \mu\text{m}$ depending on the context. The regenerating zone spanning from $-L_0$ to the tip includes the source zone and the outgrowth.

could also influence the observed spinal cord outgrowth (Section 3.2.3). In section 3.2.4, I will quantify the contributions of all possibly involved cell behaviors. Particularly, I make use of neural stem cell density measurements (Rodrigo Albers et al. 2015) to show that convergence and extension is negligible. I make use of cell proliferation-related measurements along the AP axis of the spinal cord (Rodrigo Albers et al. 2015) to identify a high-proliferation zone that extends $800 \mu\text{m}$ anterior to the amputation plane, and calculate changes in cell cycle kinetics within this zone. By measuring the displacement of sparsely-labeled cells, I also determine the cell influx into the regenerating spinal cord.

Subsequently, I set up a mathematical model of spinal cord outgrowth that incorporates cell proliferation, stem cell activation and cell influx (Section 3.2.5). Using this model, I test the contribution of each of these cell behaviors to the regenerative outgrowth. Comparing the predictions of the model with experimental data of tissue outgrowth I show that while cell influx and quiescent stem cell activation are of minor importance, the acceleration of the cell cycle in the high-proliferation zone indeed is the major driver of the regenerative spinal cord outgrowth. Then, I demonstrate how the same model ideas can be applied to understand the regulation of cell behaviors in perturbed regeneration conditions (Section 3.2.6).

Finally, I estimate the cell cycle parameters and calculate the size of the progenitor cell pool in the adjacent, regenerating muscle tissue (Section 3.3). I find similar cell cycle lengths and a source zone lengths for spinal cord and muscle tissue.

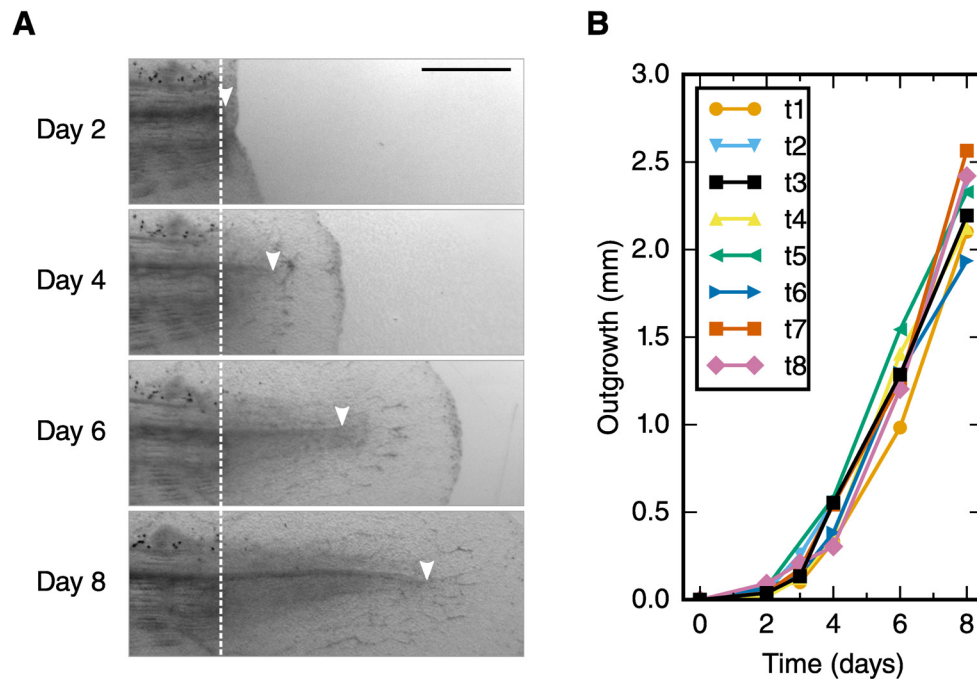


Figure 3.4.: **A:** Time-lapse images of a selected regenerating spinal cord after tail amputation (all time-lapse images in fig. S1). The white dashed line marks the amputation plane. The arrowheads mark the tip of the regenerating spinal cord. Scale bar, 1 mm. **B:** Spinal cord outgrowth time-course during the first 8 d after amputation ($n = 8$ axolotls).

3.2. RESULTS: SPINAL CORD REGENERATION

3.2.1. SPINAL CORD OUTGROWTH TIME-COURSE

I measured the length of the spinal cord outgrowth in time-lapse images of individual axolotls during the first 8 days of regeneration using Fiji (Schindelin et al. 2012) (Figure 3.4A and fig. S1, for experimental method see Rost et al. (2016a)).¹ Time starts with the event of amputation. For spatial positions along the AP axis of the spinal cord, the amputation plane defines 0; positive values refer to positions posterior to the amputation plane, in regenerated tissue; negative values refer to positions anterior to the amputation plane. First, the amputation plane which is clearly visible in the surrounding myotome was marked with a line. Then, the length between the intersection of the amputation plane with the spinal cord and the spinal cord tip was measured with Fiji's line tool.

The regenerating axolotl spinal cord grows with increasing velocity following tail amputation: Initially, the regenerating spinal cords extended slowly to a mean outgrowth of (0.45 ± 0.04) mm at day 4 and thereafter faster, achieving (2.3 ± 0.1) mm at day 8

¹Original image data can be found online: F. Rost et al. (2016b). *Accelerated Cell Divisions Drive the Outgrowth of the Regenerating Spinal Cord in Axolotls - Supplementary File 1*. DOI: 10.5281/zenodo.59817

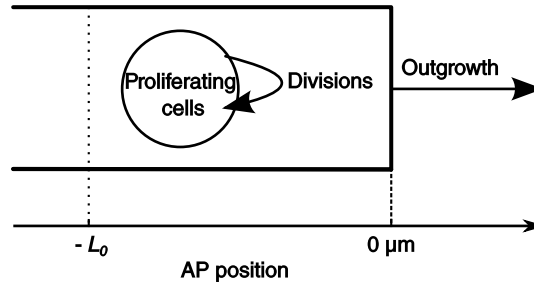


Figure 3.5.: Proliferation-driven outgrowth model of spinal cord outgrowth. Stem cells divide in a source zone of length L_0 . If one assumes that the stem cell density along the AP axis is constant then the increase in stem cell number will lead to an outgrowth.

(Figure 3.4B). Hence, the mean growth speed in the first 8 days after amputation is

$$v = \frac{(2.3 \pm 0.1) \text{ mm}}{8 \text{ d}} = (0.28 \pm 0.01) \text{ mm d}^{-1} = (11.8 \pm 0.4) \mu\text{m h}^{-1} \quad (3.1)$$

To illustrate this number I would like to mention that this growth speed corresponds approximately to the growth speed of human hair (Loussouarn et al. 2005).

3.2.2. A PROLIFERATION-DRIVEN OUTGROWTH MODEL

An increase in growth speed, as observed in the spinal cord outgrowth time-course (Figure 3.4B), is a typical feature of proliferation-driven growth. For instance, it can be observed in the exponential growth phase of bacterial colonies. Therefore, I asked whether the observed outgrowth time-course could be explained with a simple proliferation model. In this section, I will develop 3 proliferation based candidate models to explain the outgrowth time-course. I will fit them to the outgrowth data with a ML approach and make use of the AICc to select the best fitting model among the candidates. I assume that the density of stem cells along the AP axis, ρ , is constant (Figure 3.1). Hence, in the model, the length of a spinal cord region, L_{SC} is proportional to the stem cell number in this region, N :

$$N = \rho \cdot L_{SC}. \quad (3.2)$$

For the first model, I assume that the spinal cord grows due to constant proliferation of cells in a source zone of length L_0 (Figures 3.3 and 3.5). The time-course of the cell number is then given by the Malthusian growth model (Murray 2002):

$$\frac{dN(t)}{dt} = rN(t), \quad N(0) = N_0. \quad (3.3)$$

Here, $N(t)$ is the number of cells at time t and r is the proliferation rate. Substituting $N(t)$

Model	Parameters	Values	68% error
Malthus, 500 μm	r (d^{-1})	0.211	± 0.003
Biphase, 500 μm	r_1 (d^{-1})	0.054	± 0.008
	r_2 (d^{-1})	0.282	± 0.009
	t_{switch} (d)	2.3	± 0.2
Biphase	r_1 (d^{-1})	0.014	± 0.007
	r_2 (d^{-1})	0.13	± 0.05
	t_{switch} (d)	2.7	± 0.1
	L_0 (μm)	2051	± 1038

Table 3.1.: Parameter values estimated by fitting proliferation models to outgrowth time-course.

and N_0 with eq. (3.2) and defining the outgrowth as $L(t) = L_{SC}(t) - L_0$, one gets

$$\frac{dL(t)}{dt} = r(L(t) + L_0), \quad L(0) = 0, \quad (3.4)$$

which is solved by the exponential growth

$$L(t) = L_0(e^{rt} - 1). \quad (3.5)$$

Please note that the time-course of $L(t) + L_0$ will form a straight line in a semi-logarithmic plot because

$$\ln(L(t) + L_0) = rt + \ln L_0. \quad (3.6)$$

As mentioned above, Mchedlishvili et al. (2007) reported that the regenerated spinal cord stems from a region spanning at least 500 μm . If we assume $L_0 = 500 \mu\text{m}$, the only unknown parameter in eq. (3.5) is the proliferation rate, r . I estimated r with a ML approach using additive normally distributed noise as an error model. Using eq. (3.5) in eq. (2.2) the corresponding log-likelihood, $\ln \mathcal{L}$, is

$$\ln \mathcal{L}(r, \sigma_{\text{day}2}, \dots, \sigma_{\text{day}8}) = -\frac{1}{2} \sum_{i=1}^n \left(\frac{L_i(t_i, r) - L_i^{\text{exp}}}{\sigma_{t_i}} \right)^2 + \sum_{i=1}^n \ln \left(\frac{1}{\sqrt{2\pi}\sigma_{t_i}} \right), \quad (3.7)$$

where $\sigma_{\text{day}2}, \dots, \sigma_{\text{day}8}$ are the error model parameters describing the standard deviation of the noise at day 2 to day 8. Maximization of the likelihood lead to the best fit shown in fig. 3.6, left panel.²

The estimated parameter value for the proliferation rate is $r = (0.211 \pm 0.003) \text{d}^{-1}$ which corresponds to a cell cycle length of about 3.3 days (Table 3.1). From fig. 3.6 it

²Source code for the numerical optimization can be found under https://nbviewer.jupyter.org/github/fabianrost84/axolotl-calculations-phd/blob/master/proliferation_model.ipynb

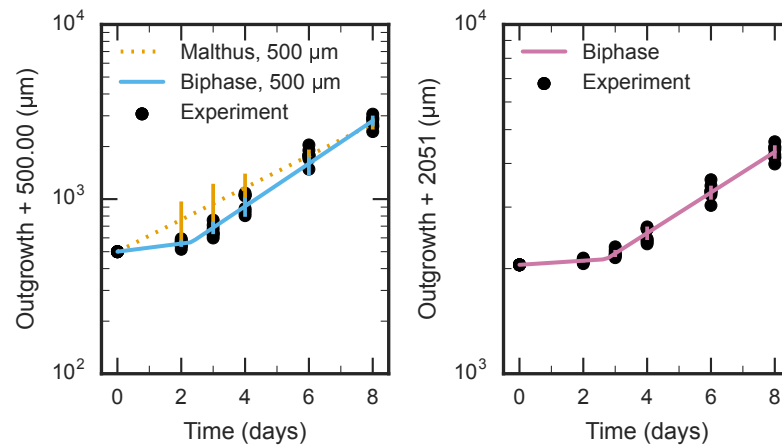


Figure 3.6.: Semi-logarithmic plots of the outgrowth time-course. Left panel: As $L_0 = 500 \mu\text{m}$ for the Malthus growth model and the first case of the biphasic growth model, the y-axis shows $L(t) + 500 \mu\text{m}$. Then, the model predictions form lines in semi-logarithmic plots (Equation (3.6)). The best fit of the Malthus model (orange, dotted line) and the 'Biphase, 500 μm ' model (blue, solid line) are shown. Error bars show the predicted standard deviations. The experimental measurement of the outgrowth is shown as black dots. Right panel: Similar to the left panel, but $L_0 = 2051 \mu\text{m}$. Purple line shows the best fit of the 'Biphase' model.

is evident that this simple model systematically overestimates the outgrowth at early time-points. Therefore, I asked whether a model with time-dependent proliferation rate $r(t)$,

$$\frac{dL}{dt} = r(t) \cdot (L + L_0), \quad L(0) = 0, \quad (3.8)$$

could describe the outgrowth time-course better. A simple time dependent model for the proliferation time-course is a biphase-model:

$$r(t) = \begin{cases} r_1 & \text{for } t \leq t_{switch} \\ r_2 & \text{for } t > t_{switch} \end{cases}. \quad (3.9)$$

The idea behind that model would be, that the response to the amputation event is delayed: The spinal cord initially grows slowly with rate r_1 and only after a delay time, t_{switch} , the rate increases to r_2 . The solution of this model is a biphase exponential growth:

$$L(t) = \begin{cases} L_0 \cdot (e^{r_1 t} - 1) & \text{for } t \leq t_{switch} \\ L_0 \cdot (e^{r_1 t_{switch}} - 1) \cdot (e^{r_2 t} - 1) & \text{for } t > t_{switch} \end{cases}. \quad (3.10)$$

Analogous to eq. (3.6) the time-course of $L(t) + L_0$ is a stepwise linear function in a semi-logarithmic plot. I estimated the parameters analogous to the previous model for 2 model cases: In the first case, I call this model 'Biphase, 500 μm ', I set $L_0 = 500 \mu\text{m}$ and fitted the model parameters r_1 , r_2 and the error model parameters $\sigma_{\text{day } 2}, \dots, \sigma_{\text{day } 8}$ (Figure 3.6, left panel and table 3.1). In the second case, called 'Biphase', I did not fix the source zone length L_0 but also fitted it simultaneously (Figure 3.6), right panel and table 3.1). It should be noted that in the latter case I only allowed for $L_0 \geq 500 \mu\text{m}$ while fitting the model. Both model variants match the data well (Figure 3.6). Hence, a purely proliferation-driven outgrowth model is sufficient to explain the observed outgrowth kinetics.

Next, I asked what is the best model to describe the observed outgrowth. For that I make use of model selection with the AICc (see section 2.1.3) Please note that for the model variant with time dependent proliferation rate, $r(t)$, both cases correspond to different models in the sense of model selection. Hence, together with the simple initial approach of constant proliferation (Equation (3.4)), I used 3 different models to describe the outgrowth time-course. To select the best model among those 3 candidates, I calculated the AICc and the ER using eq. (2.7) and eq. (2.9), respectively (Table 3.2). The model 'Biphase' has the lowest AICc. With an ER of 'Biphase' versus the second best model 'Biphase, 500 μm ' of 24, I conclude that the model 'Biphase' is the best model among the 3 candidates (see section 2.1.3).

Hence, I found strong evidence that the proliferative response is time-dependent: An initial slow growth is followed by a fast growth starting around day 3 ($t_{switch} = 2.7 \pm 0.1$) d). Furthermore, the estimate of $L_0 = (2 \pm 1)$ mm indicates the zone that is responsible for the spinal cord outgrowth might be bigger than the previously reported 500 μm zone. However, it is important to keep in mind that this initial analysis of the

Models	$\ln \mathcal{L}$	k	AICc	ER
Malthus, 500 μm	5.67	6	1.65	2.8×10^{13}
Biphase, 500 μm	36.45	8	-53.90	24
Biphase	41.14	9	-60.29	1

Table 3.2.: Log-likelihood, k (number of free parameters), AICc and ER of the proliferation models. For the number of free parameters keep in mind, that it is the sum of the 5 error model parameters $\sigma_{\text{day}2}, \dots, \sigma_{\text{day}8}$ and the proliferation model parameters (Table 3.1).

outgrowth time-course was based on the hypothesis that the outgrowth is solely driven by proliferation. Of course, other cell behaviors could be involved in driving the outgrowth. In the next section I will review all possible cell behaviors that could drive the outgrowth.

3.2.3. CELL BEHAVIORS THAT COULD DRIVE OUTGROWTH

The spinal cord grows and extends in AP direction during early regeneration (Figure 3.4). As stated in the introduction of this chapter, proliferation is necessary for proper outgrowth. In section 3.2.2 I showed that a proliferation mechanism could be sufficient to explain the observed outgrowth time-course. To assess whether proliferation is the only cell behavior and to test the predictions of the proliferation-driven outgrowth model I will quantify the contribution of different cell behaviors in the next section. But first, I want to describe all cell behaviors that are possibly driving the outgrowth.

A tissue can extend due to two classes of mechanisms, namely volumetric growth, i.e. mechanisms that increase the tissue's volume or tissue convergence, i.e. mechanisms that don't increase tissue volume (Steventon et al. 2016). Volumetric growth can for example be realized by an increase of the volume of single cells or by deposition of extracellular matrix. Furthermore, the addition of cells to the tissue due to cell movements into the tissue can also be interpreted as volumetric growth.

Tissue convergence could be accomplished by rearrangements of cells as it is seen in convergence and extension movements during the development of embryos. Another possible manifestation of tissue convergence could be volume conserving cell shape changes which compress the cell in one direction but extend it in another direction. Interestingly, cell divisions do not necessarily lead to an increase in tissue volume. This is best exemplified in cleavages, the early embryonic cell divisions, which do not lead to significant growth (Gilbert 2010; Kimmel et al. 1995; Wolpert et al. 2002). However, in the case that cell size is conserved, i.e. both daughter cells grow to the size of the mother cell, cell divisions lead to volumetric growth.

My aim is an understanding of how such cell behaviors could lead to the observed spinal cord outgrowth during the first 8 days of axolotl tail regeneration in this chapter. Now, I'd like to state which of the mechanisms reported above could in principle play a

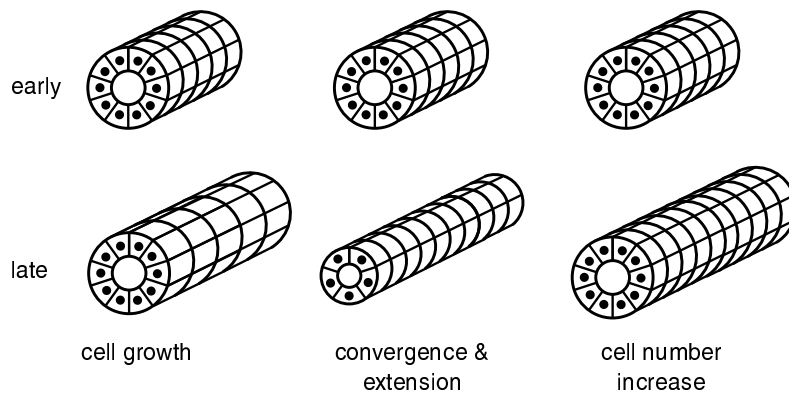


Figure 3.7.: Possible cell behaviors that could lead to spinal cord outgrowth illustrated at an idealized scheme of the spinal cord. **Left:** An increase in AP cell length of individual cells. **Middle:** Rearrangement of cells by convergence and extension. Decreasing the number of cells per cross section leads to an increase in tissue length. **Right:** An increase in cell number also leads to tissue scale outgrowth if the AP cell length is constant.

role in spinal cord growth. The neural stem cells form a single-layered epithelial tissue for which no major addition of extracellular matrix has been reported. Instead, they are tightly packed (Rodrigo Albors et al. 2015). Of course, neural stem cells could increase their AP length (Figure 3.7, left). Whether they would do so by increasing their volume or by volume conserving shape changes would be irrelevant for the observed spinal cord outgrowth.

Another possibility would be the rearrangement of stem cells by convergence and extension movements. By decreasing the number of cells per cross section the length of the spinal cord could be increased (Figure 3.7, middle). The third possibility would be growth due to an increase in cell number. This increase could be achieved by recruiting stem cells that are initially far away from the injury to move towards the injury site or the cell number increase could also be due to cell-size conserving cell divisions (Figure 3.7, right). As there is no evidence for neuron de-differentiation or differentiation of neural stem cells into neurons in this early period, I exclude those as possible mechanism to change cell number (Zhang et al. 2003). Furthermore, there is no evidence of significant amounts of apoptosis during regeneration and therefore I neglect possible cell losses due to cell death (Rodrigo Albors et al. 2015).

In the following section I will show how we quantified the contributions of all the mechanisms possibly involved in spinal cord outgrowth, namely cell elongation, cell rearrangements and increase in cell number. Concerning cell number increase, I will investigate proliferation and cell movements.

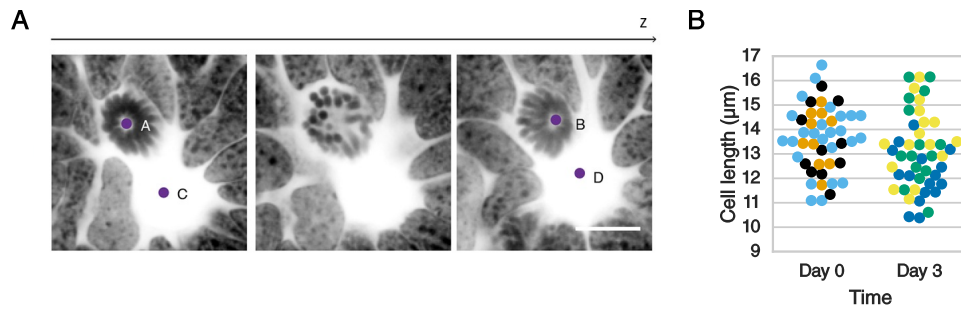


Figure 3.8.: Stem cell length does not change during regeneration. **A:** Images show single optical confocal slices through a 3D tissue section along the AP axis of a regenerating axolotl spinal cord. DNA is labeled with Hoechst (inverted grayscale). Scale bar, 10 μm . For a video showing all slices of the z-stack see <https://elifesciences.org/lookup/doi/10.7554/eLife.10230.007>.^a **B:** For 3 uninjured and 3 regenerating axolotls at day 3 the AP length of SOX2⁺ stem cells was measured in 3D tissue sections like the one shown in (A). Each animal is denoted by a different color. The mean cell length is not significantly different when comparing the uninjured (Day 0) and the regenerating (Day 3) condition (t-test, $p = 0.06$). The data for this plot can be found in a Supplementary notebook under https://nbviewer.jupyter.org/github/fabianrost84/axolotl-calculations-phd/blob/master/cell_length.ipynb.

^aReprinted from Rodrigo Albers et al. 2015, Fig. 4A.

3.2.4. QUANTIFICATION OF CELL BEHAVIORS

CELL LENGTH

I used a dataset of AP cell lengths of randomly chosen cells in 3D confocal images from uninjured and regenerating spinal cords, respectively (Figure 3.8) (Rodrigo Albers et al. 2015). There were 3 animals per time point. Figure 3.8B reveals, that the AP cell length stays approximately constant, independent of the time after amputation the cells were taken from. Therefore, I exclude a change in cell shape as a driving force of the spinal cord outgrowth. Taking the mean over all measured cell lengths, I found that cells have a mean length in AP direction of $(13.2 \pm 0.1) \mu\text{m}$.

CELL REARRANGEMENTS

The spinal cord outgrowth could also be driven by convergence and extension-like cell rearrangements. If that would be the case one would observe a decrease in the number of SOX2⁺ stem cells per cross section during the course of regeneration.

To quantitatively investigate neural stem cell arrangement in space and time, we counted the number of SOX2⁺ cells per cross section in uninjured and regenerating spinal cords at different positions along the AP axis and at different time points (Figures 3.2

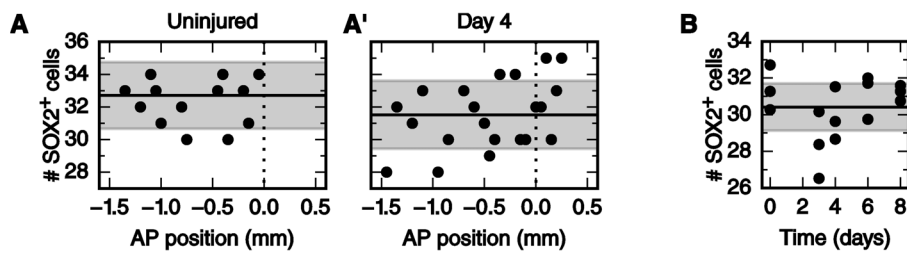


Figure 3.9.: Number of stem cells per cross section is constant. **A,A'**: Number of SOX2⁺ cells per cross section along the AP axis of a selected uninjured (A) and a selected day 4-regenerating spinal cord (A'). Black line and gray region indicate the mean number of SOX2⁺ cells and the standard deviation, respectively. Plots for all individual axolotls are in fig. S2. **B**: Spatial average of the number of SOX2⁺ cells per cross section of individual axolotls against time (black dots). Black line and gray region indicate the mean number of SOX2⁺ cells and the standard deviation of all animals, respectively. The data for this plot can be found in the Supplementary notebook to Rodrigo Albors et al. (2015) under <https://nbviewer.jupyter.org/3cc58a27b5688f4e2eba>.

and 3.9) (for the experimental details on how those images were obtained see Rodrigo Albors et al. (2015)). I tested the number of SOX2⁺ cells per cross section dataset for the occurrence of significant changes along the AP axis with 3 different methods (see Supplementary notebook 'Constant Density' from Rost et al. (2016d) for the source code).

First, I tested if the cell count data linearly depends on spatial position along the AP axis using Bayesian inference. The slope was always smaller than 0.13 cells/mm and only significantly different from 0 ($p < 0.05$) for 4 of the 15 replicates. Second, I fitted a model of 2 spatially homogeneous zones to the data using Bayesian inference. Here, only 4 of the 15 replicates showed a significant difference in density between the two zones ($p < 0.05$). These first two methods indicated that, for an average animal, there is no significant change of the number of SOX2⁺ cells per cross section along the AP axis. As I showed above that the AP cell length is also constant. This means that according to eq. (3.2) the number of SOX2⁺ stem cells per cross section is a proxy for the stem cell density along the AP axis. Hence, as the number of SOX2⁺ stem cells per cross section is constant in space also the stem cell density along the AP axis is constant in space.

Third, I collapsed the data ignoring the spatial position. I tested the resulting cell count histogram for being normally distributed using D'Agostino and Pearson's test as implemented in the SciPy function `scipy.stats.normaltest` (D'Agostino 1971; D'Agostino and Pearson 1973). If the mean number of SOX2⁺ stem cells per cross section would be constant in space and deviations from the mean follow a normal distribution the null hypothesis should not be rejected by the test. Indeed, only for one of the 15 replicates the null hypothesis was rejected ($p < 0.05$) and hence I considered the number of SOX2⁺ cells per cross section as spatially homogeneous with normally distributed noise in this

study.

Knowing that the density is constant in space, it could still vary over time. To access whether the density varies over time, I estimated the mean number of SOX2⁺ cells per cross section averaged over all measurements along the AP axis for each axolotl separately (Figure 3.9B). To access whether there was a significant change in this mean number over time, I grouped the axolotls according to their time after amputation. I performed a one-way ANOVA-test which showed no significant differences among the groups ($p = 0.08$, see Supplementary notebook 'Constant Density' from Rost et al. (2016d) for the source code).

Taken together, I found that the number of SOX2⁺ cells per spinal cord cross section is constant along the AP axis in both uninjured and regenerating samples at any time (Figures S2 and 3.9). I also found that the number of SOX2⁺ cells per cross section spatially averaged along the AP axis is constant during regeneration time (Figure 3.9B). A mean number of 30.4 ± 0.6 SOX2⁺ cells is found in cross sections of the axolotl spinal cord. Using our measurements of the AP cell length and using eq. (3.2) I find that the mean density of cells along the AP axis is equal to (2.3 ± 0.6) cells/ μm .

These findings lead me to exclude cellular rearrangements as a driving force of the spinal cord outgrowth in the axolotl. Instead, constant neural stem cell density implies an increasing stem cell number during spinal cord outgrowth. This suggests that the expansion of the regenerating stem cell pool could depend on proliferation-related mechanisms. I therefore move forward to quantify proliferation next.

SPATIOTEMPORAL PATTERN OF PROLIFERATION

To establish spatial and temporal changes in cell proliferation during regeneration, we calculated different cell proliferation parameters along the uninjured and regenerating spinal cord. Therefore, we quantified the number of proliferating cells and the number of mitotic cells using an antibody against PCNA and Hoechst DNA staining, respectively (for the experimental method see Rodrigo Albors et al. (2015)). We used these datasets to estimate the growth fraction, i.e. the fraction of SOX2⁺/PCNA-positive (PCNA⁺) cells (proliferative cells), and the mitotic index, i.e. the fraction of proliferating cells undergoing mitosis. Although both SOX2⁺/PCNA⁺ cells and mitotic cells did not show any evident spatial pattern along the AP axis in uninjured animals (Figure 3.10A, points), they showed a tendency of increasing posteriorly at times later than 4 days post amputation (Figure 3.10A', points).

To elucidate whether proliferation was patterned along the AP axis during the time of regeneration, I tested the data with a stochastic mathematical model of two spatially homogeneous zones characterized by their growth fraction and mitotic index and separated by a border that we call the switchpoint (Figure 3.10B,B'). I reasoned that in the absence of AP patterning the two zones could not be distinguished (meaning that the two zones would collapse into a single one) while if proliferation events would be locally upregulated the model would allow us to determine the magnitude and the location of

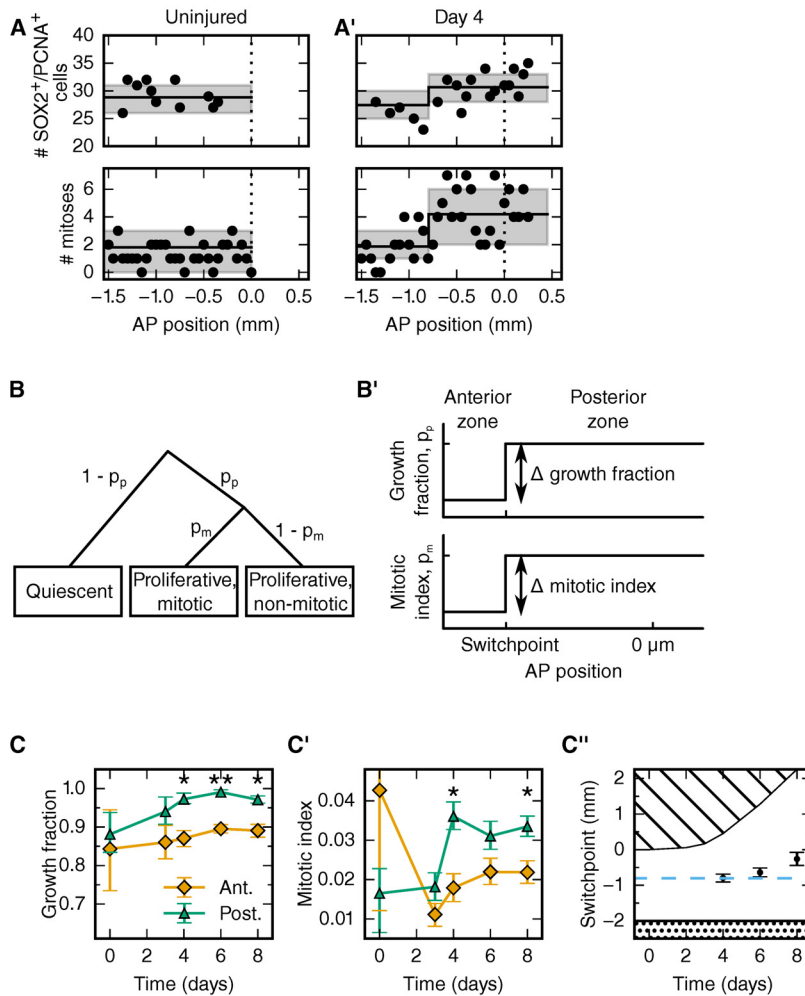


Figure 3.10.: Spatiotemporal pattern of proliferation. **A,A'**: Number of SOX2⁺/PCNA⁺ cells per cross section (upper panel) and mitotic cells per section (lower panel) along the AP axis in a selected uninjured (A) and a selected day 4-regenerating spinal cord (A'). Black line and the gray region show the expected number and the 68% confidence belt for the best fit of the model with two spatial proliferation zones, respectively. Plots for all animals in fig. S3. **B**: Possible cell states in the two spatial proliferation zones model used to analyze the spatial cell proliferation dataset (A,A'). p_p , probability that a cell is proliferative, otherwise quiescent. p_m , probability that a proliferative cell undergoes mitosis. **B'**: The model has two proliferation zones. The location of the border between zones is called *switchpoint*. **C-C'**: Results of model fitting for growth fraction (C) and mitotic index time-course (C') in the anterior (orange diamonds) and posterior (green triangles) zone. Error bars indicate the 68% credibility interval. **C''**: Black dots mark the switchpoint. Blue dashed line marks 800 μm anterior to the amputation plane. The dashed region marks the space outside of the embryo, the dotted region marks the unaffected part of the embryo.

the upregulated proliferation.

For a given growth fraction and mitotic index, the model predicts the expected number of proliferating cells and mitotic cells per cross section (Figure S5). It was defined as follows:

If the number of SOX2⁺ cells for a specific cross section along the AP axis, N_S , was measured it was used for this section. If the data for the specific section was missing, N_S , was imputed by assuming that there is a constant expected number of SOX2⁺ cells per cross section and that the deviations from the expected value follow a normal distribution. The evidence for this assumption was presented in section 3.2.4. The mean and standard deviation of this normal distribution were estimated by the sample mean and standard deviation of the sample of the measured numbers of SOX2⁺ cells per cross section for each animal, respectively. The number of SOX2⁺ cells in a cross section is assumed to be independent from other cross sections.

The state 'Proliferative', i.e. SOX2⁺/PCNA⁺, is independently assigned to each SOX2⁺ cell with probability p_p or 'Quiescent' with probability $1 - p_p$ (Figure 3.10B). Hence, for a given number of SOX2⁺ cells in a cross section, N_S , the number of SOX2⁺/PCNA⁺ cells per cross section, N_P , follows a binomial distribution with N_S experiments and success probability p_p . Consequently, the expected growth fraction equals p_p . As the number of mitotic cells, N_M , in 3D 50 μm tissue sections was measured previously, we estimated the number of SOX2⁺/PCNA⁺ cells also in a 3D 50 μm section, $N_{PS} = 50 \mu\text{m}/l_{cell} \cdot N_P$, where $l_{cell} = (13.2 \pm 0.1) \mu\text{m}$ is the mean AP length of SOX2⁺ cells (see section 3.2.4).

Following from the assumption that the cell cycle position and hence the cell cycle phase of each cell is independent of all other cells, the state 'Proliferative, mitotic' is independently assigned to each SOX2⁺/PCNA⁺ cell with probability p_m or 'Proliferative, non-mitotic' with probability $1 - p_m$. Hence, the number of mitotic cells per section, N_M , follows a binomial distribution with N_{PS} experiments and success probability p_m . Consequently, the expected mitotic index equals p_m .

For given values of p_p and p_m the model gives a likelihood for the observed number of SOX2⁺/PCNA⁺ cells per cross section and mitotic cells per 3D section that can be used to fit the model parameters. To reflect the assumption of two spatial proliferation zones, p_p and p_m have spatial dependencies in the form of step functions (Figure 3.10B'). Hence, there can be different growth fractions and mitotic indices for an anterior and a posterior zone, respectively. The spatial position of the border between the zones is another model parameter termed *switchpoint*. Furthermore, variability between animals in the switchpoint is modeled as a normal distribution with standard deviation σ_{switch} . Likewise, variability in growth fraction and mitotic index between animals is modeled with a normal distribution with spatially homogeneous standard deviations σ_{GF} and σ_{mi} , respectively. Hence, the resulting model to describe the cell count data of all animals at one time-point has 8 parameters: the switchpoint, growth fraction and mitotic index in the anterior zone and in the posterior zone, respectively, and the inter-animal variabilities σ_{switch} , σ_{GF} and σ_{mi} .

Those parameters were estimated with Bayesian inference using uniform priors. Fitting

was performed using a Markov chain Monte Carlo algorithm implemented in PyMC.³ To verify the fitting procedure, test data were created by simulating our model with picked parameter values. These "true" parameter values were then found to be included in the 95% credibility intervals of the parameter values inferred from the test data with my fitting procedure.

Consequently, I fitted the model to the cell number datasets of uninjured and regenerating spinal cords at day 3, 4, 6 and 8 after amputation (Figure 3.10A,A', figs. S3 and S4) to determine the growth fraction, the mitotic index, and the switchpoint for each time-point (Figure 3.10C-C"). Perhaps not surprisingly, I found that in the uninjured spinal cord the growth fraction and the mitotic index in the two modeled zones are not significantly different (Figure 3.10A,C,C'). Hence, the proliferation parameters are spatially homogeneous in the uninjured spinal cord. Similarly, at day 3, there are no significant differences between the two zones (Figure 3.10C,C'). In contrast, the growth fraction and the mitotic index are higher in the posterior zone from day 4 onward (Figure 3.10A,C,C'). These findings reveal that a high-proliferation zone emerges in the regenerating spinal cord at day 4. At this time-point, the switchpoint between the two zones is located (800 ± 100) μm anterior to the amputation plane, but shows the tendency to shift posteriorly at later time-points as the regenerating spinal cord grows (Figure 3.10C").

QUANTIFICATION OF PROLIFERATION RATE TIME-COURSE

In the previous section I showed that cell proliferation increases in a high-proliferation zone 800 μm anterior to the amputation plane in 4-days regenerates (Figures 3.3 and 3.10). In this section, I combine the above mitotic index measurements with a cell cycle length estimate at day 6 to establish how the proliferation rate changes in this zone during regeneration.

We estimated the cell cycle length at day 6 using a cumulative BrdU labeling approach (for the experimental method see Rodrigo Albors et al. (2015)). The basic idea of this approach is to continuously treat the axolotls with BrdU injections. The thymidine analogue BrdU will then be incorporated into the DNA of cells that synthesized new DNA in the S-phase of the cell cycle. One can then measure the time course of the fraction of BrdU-labeled cells lining the central canal of the spinal cord. Indeed, the fraction of BrdU-labeled cells increased over time as cells duplicated their DNA, until all proliferating cells were labeled (Figure 3.11A). Intuitively, one expects that the fraction increases faster if the cells proliferate faster. This has also been formulated in quantitative mathematical models for the time course of the fraction of BrdU-labeled cells (Lefevre et al. 2013; Nowakowski et al. 1989). I extended the modeling framework developed by Lefevre et al. (2013) which is, in turn, an adaptation of the model by Nowakowski et al. (1989) to extract the cell cycle parameters from the cumulative BrdU labeling data.

³for the source code see Supplementary notebook "step_model_fixed_density_fit_per_time-point" from Rost et al. (2016d)

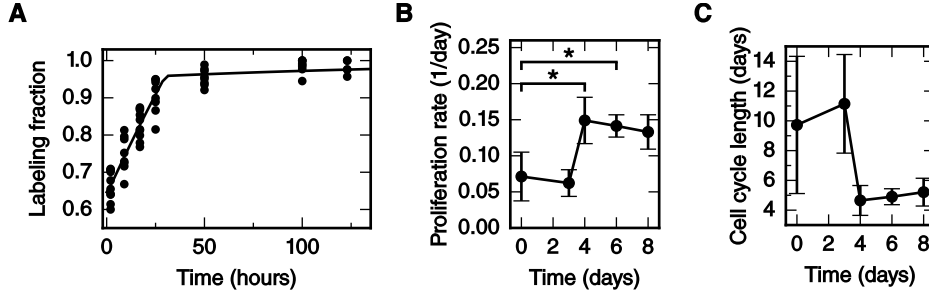


Figure 3.11.: Proliferation rate time-course. **A:** Labeling fraction time course and fit. **B:** Proliferation rate time-course in the high-proliferation zone. **C:** Cell cycle length time course, $T_C(t)$

Under the assumptions that (i) the length of the cell cycle and the cell cycle phases are constant for all cells, that (ii) divisions occur completely asynchronous and that (iii) all cells are proliferating the model by Lefevre et al. (2013) predicts the fraction of BrdU-labeled cells, R' :

$$R'(t) = \begin{cases} \frac{r \frac{T_{G2+M}+T_S}{T_C} - r \frac{T_{G2+M}-t}{T_C}}{r-1} & 0 \leq t < T_{G2+M} \\ 1 - \frac{T_C+T_{G2+M}-t}{r-1} - r \frac{T_{G2+M}+T_S}{T_C} & T_{G2+M} \leq t < T_C - T_S \\ 1 & t \geq T_C - T_S \end{cases} \quad (3.11)$$

for $r \neq 1$ and where t is the time after the start of BrdU injections, T_C is the cell cycle length, T_S is the length of S-Phase, T_{G2+M} is the combined length of G2 and M-phase and r is the average number of daughter cells that remained proliferative progenitor cells.

As there is no evidence that neural stem cells differentiate in the early period of regeneration (Zhang et al. 2003), I assumed proliferative cell divisions, i.e. each cell division produces two proliferating cells. Hence, I set $r = 2$. As there are also non-proliferating cells we have to correct the labeling fraction R' with the growth fraction GF :

$$R(t) = GF(t)R'(t). \quad (3.12)$$

In the case of proliferative cell divisions the growth fraction will shrink over time because the proliferating cells increase and the non-proliferating cells remain constant in number. Hence,

$$GF(t) = \frac{GF_0 r^{\frac{t}{T_C}}}{GF_0 r^{\frac{t}{T_C}} + 1 - GF_0} \quad (3.13)$$

where GF_0 is the initial growth fraction at $t = 0$.

I estimated the parameters for each cell population by the method of least squares, that is, minimizing the SSE, SSE , calculated as follows:

$$SSE(T_S, T_C, T_{G2+M}, GF_0) = \sum_{i=1}^n (R_{exp_i} - R(t_i, T_S, T_C, T_{G2+M}, GF_0))^2,$$

where n is the number of measurements and $Rexp_i$ is the measured BrdU-labeling fraction of the i -th measurement at time t_i . I minimized the SSE using the migrad algorithm implemented in the python module `iMinuit` (<https://github.com/iminuit/iminuit>) (James and Roos 1975). I determined the parameter errors by bootstrapping using case resampling. The BrdU labeling data and the implementation of the parameter estimation can be found in the Supplementary Notebook 'BrdU_bootstrapping_day6' from Rost et al. (2016d). I found a cell cycle length of (117 ± 12) h corresponding to a proliferation rate of $(0.21 \pm 0.02) \text{ d}^{-1}$ at 6 days after amputation.

As the mitotic index is proportional to the proliferation rate (Smith and Dendy 1962), the mitotic index time-course in the high-proliferation zone was rescaled with the proliferation rate at day 6 to obtain the proliferation rate time-course:

$$r(t) = \frac{mi(t)}{mi(\text{day } 6)} r(\text{day } 6),$$

where $r(t)$ is the proliferation rate at time t and $mi(t)$ is the mitotic index at time t .

I found that the proliferation rate is $(0.06 \pm 0.02) \text{ d}^{-1}$ in the uninjured spinal cord which corresponds to a cell cycle length of (10 ± 4) days (Figure 3.11B,C). The proliferation rate is similar at day 3. However, at day 4 the proliferation rate increases to about 0.15 d^{-1} corresponding to a cell cycle length of about 5 days and the proliferation rate remains that high until day 8.

ACTIVATION OF QUIESCENT STEM CELLS

Two possible scenarios could lead to the observed increased growth fraction in the high-proliferation zone (Figure 3.10C'): the activation of quiescent stem cells, or the dilution of quiescent cells due to the expansion of the proliferating cell population. If quiescent cells were activated, the total number of quiescent cells in the high-proliferation zone would decrease. Given the mean number of $\text{SOX2}^+/\text{PCNA}^-$ cells per cross section, N_{qs} , the mean AP cell length, l_c , and the outgrowth time-course, $L(t)$ the total number of quiescent cells in the high-proliferation zone, N_q , can be estimated by

$$N_q(t) = N_{qs} \frac{L(t)}{l_c}. \quad (3.14)$$

The resulting time course for the total number of quiescent cells in the high-proliferation zone is shown in fig. 3.12. The number of $\text{SOX2}^+/\text{PCNA}^-$ cells drops from 180 ± 30 at day 0 to 23 ± 13 at day 6 (Figure 3.12) which means that quiescent cells get activated and re-enter the cell cycle upon injury. The number of quiescent cells appears to increase again at day 8.

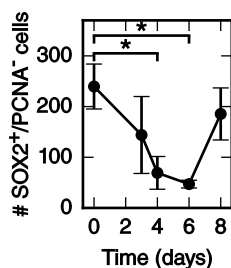


Figure 3.12.: Total number of SOX2⁺PCNA⁻ cells in the high-proliferation zone (mean ± linearly propagated 1- σ error).

CELL INFLUX

Cell movement could also contribute to the spinal cord outgrowth. To investigate whether anterior neural stem cells move into the high-proliferation zone, thereby producing a cell influx, we followed individual cells during regeneration. For that, a cytoplasmic GFP and a nuclear mCherry plasmids were co-electroporated at very low concentration to achieve sparse labeling of cells. They were tracked daily during the first 8 days of regeneration (Figure 3.13A, for experimental details see Rost et al. (2016a)). I measured the distance between the amputation plane which is visible in the myotome and the anterior border of a clone in each image using AxioVision microscopy software.

We found that labeled cells preserve their original spatial order: cells located close to the amputation plane end up at the posterior end of the regenerated spinal cord (Figure 3.13B). Most-anterior cells, however, almost do not change their position. From the clone trajectories, I calculated the mean clone velocity at different positions along the AP axis in the following way: I subdivided the space along the AP axis into 800 μm bins. For each clone trajectory I grouped the position measurements according to these bins. I excluded groups containing less than 2 measurements. Then, I estimated the average clone velocity for each group with linear regression. Next, I calculated the mean and standard deviation of the velocity of all the clones in a bin (Figure 3.13C).⁴ Clones initially located 800 $\mu\text{m}/\text{day}$ anterior to the amputation plane move slowly, with a velocity of $(20 \pm 9) \mu\text{m}/\text{day}$. In contrast, the more posterior a clone is, the faster it moves.

3.2.5. MECHANISTIC MODEL OF SPINAL CORD OUTGROWTH

Above I showed that cell density is constant along the AP axis of the regenerating spinal cord (Figure 3.9). The spinal cord must therefore grow as a result of increasing cell numbers. In line with this, I found a high-proliferation zone, first spanning from 800 μm anterior to the amputation plane, and showed that the increase in cell proliferation is due to both (i) the acceleration of cell cycle and (ii) the activation of quiescent stem

⁴Source code and data available under https://nbviewer.jupyter.org/github/fabianrost84/Rost-Rodrigo-Albors-et-al.-2016/blob/master/calculations/clone_velocities/clone_velocities.ipynb (Rost et al. 2016d)

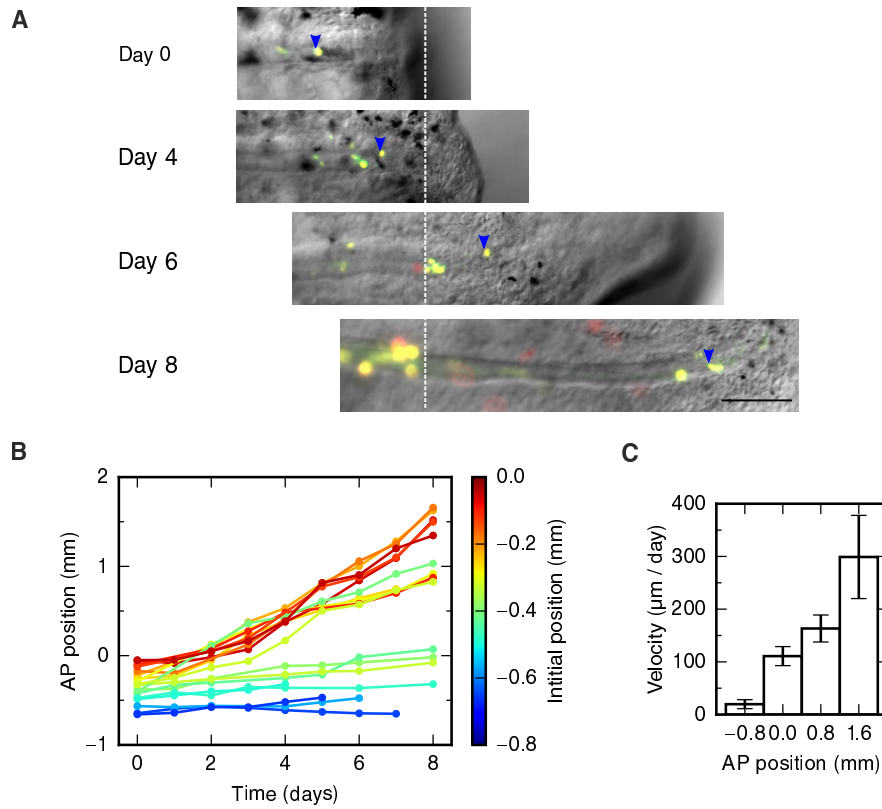


Figure 3.13.: Cell movements in the regenerating spinal cord. **A**: Selected time-lapse images of clone (blue arrowhead) tracking during spinal cord regeneration. Dashed line marks the amputation plane. Images of all clones available in Rost et al. (2016c) **B**: Tracking of 19 clones along the AP axis during regeneration. Clone trajectories are color coded by their initial position. **C**: Clone velocities at different positions along the AP axis.

cells (Figures 3.10 to 3.12). Based on our finding of cell movements during regeneration (Figure 3.13), the influx of cells into the regenerating spinal cord could also contribute to increasing the cell numbers in the regenerating spinal cord.

Hence, I propose the following mechanistic model of spinal cord growth during regeneration (Figure 3.14): A 800 μm source zone expands posteriorly by increasing the stem cell number while maintaining the stem cell density along AP axis constant. It should be noted that the model is agnostic about the mechanisms that keep the density constant. This could happen due to oriented cell division or cell rearrangements or a combination of both. There are 2 sources for the cell number increase, namely, cell divisions and influx of stem cells from anterior regions. Furthermore, quiescent stem cells are activated during regeneration. After activation, stem cells start to divide. Hence, activation of quiescent stem cells indirectly leads to enhanced growth.

To assess the contribution of these cell behaviors to the spinal cord outgrowth time-course, I used a quantitative mathematical modeling framework (Chara et al. 2014; Oates et al. 2009). For the mathematical model I assumed that cells entering into the high-proliferation zone at the switchpoint acquire the features of high-proliferative cells in terms of the same growth fraction and that the activation follows linear kinetics. With that, I formalized the influence of those cell behaviors on the total number of proliferating and quiescent stem cells in the high-proliferation zone in the following ordinary differential equations:

$$\frac{dN_p(t)}{dt} = \overbrace{r(t)N_p(t)}^{\text{cell divisions}} + \overbrace{kN_q(t)}^{\text{activation}} + \overbrace{\frac{N_p(t)}{N_p(t) + N_q(t)}v\rho}^{\text{influx}}, \quad N_p(t=0) = N_p^0, \quad (3.15)$$

$$\frac{dN_q(t)}{dt} = -kN_q(t) + \frac{N_q(t)}{N_p(t) + N_q(t)}v\rho, \quad N_q(t=0) = N_q^0. \quad (3.16)$$

where N_p^0 and N_q^0 are the initial cell numbers in this zone, $r(t)$ is the proliferation rate at time t , v is the velocity of cells 800 μm anterior to the amputation plane, ρ is the line density of cells along the AP axis and k is the quiescent cell activation rate. The factors $N_{p/q}/(N_p + N_q)$ in the third term of eqs. (3.15) and (3.16) ensure that the influx of cells into the high-proliferation zone does not alter the growth fraction. As the density is constant one can use eq. (3.2) to write

$$\rho(L + L_0) = N_p + N_q, \quad (3.17)$$

where L is the outgrowth posterior to the amputation plane and $L_0 = 800 \mu\text{m}$ is the high-proliferation zone length at $t = 0$. Using this relation and the definition of the growth fraction GF ,

$$GF = \frac{N_p}{N_p + N_q}, \quad (3.18)$$

I reformulated the cell number model as a model for spinal cord outgrowth, L , and growth

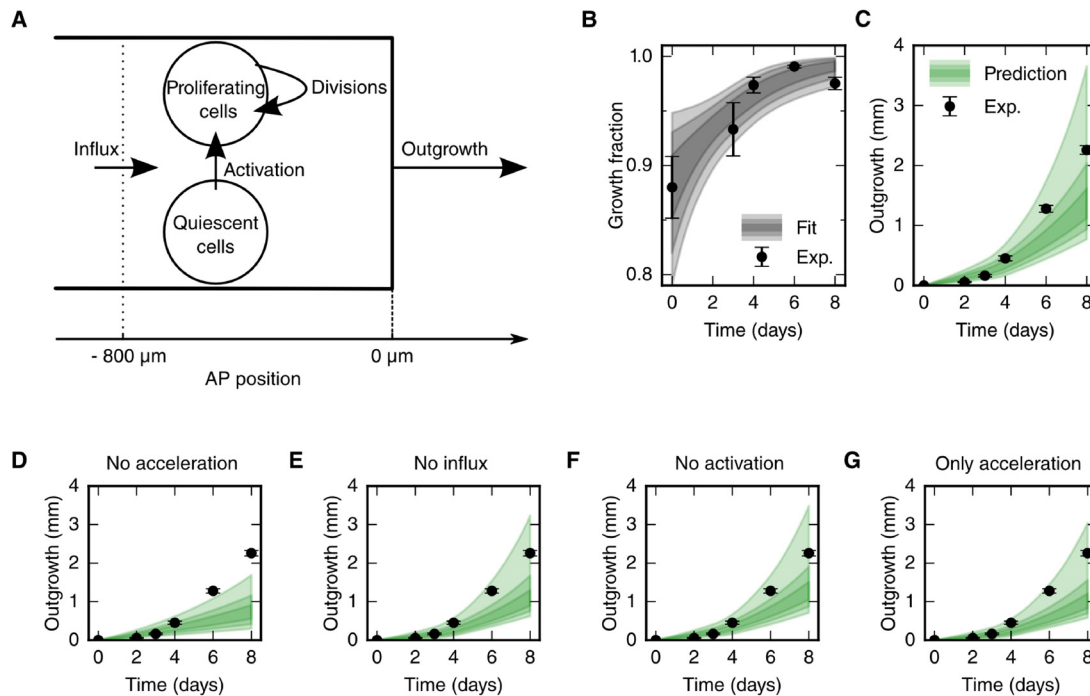


Figure 3.14.: **A:** Schematic of cell behaviors included in the model: cell proliferation, quiescent cell activation, and cell influx into the $800\ \mu\text{m}$ high-proliferation zone. **B:** Growth fraction time-course of the SOX2^+ cell population in the high-proliferation zone as observed (black dots) and fitted by the model (gray shaded areas, from darker to lighter, 68%, 95% and 99.7% confidence intervals of the model prediction). **C:** Spinal cord outgrowth during the first eight days of regeneration as observed (black dots, $n = 8$ axolotls) and predicted by the model (green shaded areas). The model prediction is in agreement with the experimental data. **D-G:** Prediction of spinal cord outgrowth for four model scenarios with selected mechanisms switched off (green shaded areas). Black dots show the same experimental data as in panel (C). **D:** The acceleration of the cell cycle is switched off. Hence, the proliferation rate is fixed to the basal proliferation rate of uninjured animals. **E:** Cell influx is switched off ($v = 0$). **F:** Quiescent cell activation is switched off ($k = 0$). **G:** Cell influx and quiescent cell activation are switched off ($k = 0, v = 0$). Corresponding predictions for growth fraction in fig. S6.

fraction, GF :

$$\frac{dL(t)}{dt} = \underbrace{r(t)(L(t) + L_0)GF(t)}_{\text{divisions of proliferating cells}} + \underbrace{\nu}_{\text{influx of cells into the high-proliferation zone}}, \quad L(t=0) = 0, \quad (3.19)$$

$$\frac{dGF(t)}{dt} = \underbrace{(1 - GF(t))k}_{\text{activation of quiescent cells}} + \underbrace{(1 - GF(t))r(t)GF(t)}_{\text{dilution of quiescent cells in the expanding pool of proliferative cells}}, \quad GF(t=0) = GF_0. \quad (3.20)$$

where $L_0 = 800 \mu\text{m}$ is the length of the high-proliferation zone, GF_0 is the growth fraction in uninjured tails, $r(t)$ is the proliferation rate at time t , ν is the velocity of cells $800 \mu\text{m}$ anterior to the amputation plane, and k is the cell cycle entry rate. As we determined the proliferation rate time-course $r(t)$ (Figure 3.11B), the initial growth fraction GF_0 (Figure 3.10C) and the influx velocity ν (Figure 3.13C) only the cell cycle entry rate k is unknown. Via eq. (3.20) the model predicts the growth fraction time-course which we already measured (Figure 3.10C). Therefore I decided to estimate the cell cycle entry rate k by fitting the model prediction to the measured growth fraction time-course. To take into account the uncertainties of the other model parameters and to simultaneously compute the CI of the model prediction I applied the following bootstrapping procedure.

The assumption that the population mean parameters correctly predict the population mean outgrowth time-course was used when simulating the model and interpreting results. The confidence intervals of the model prediction were estimated with a Monte Carlo approach using bootstrapping with a case resampling scheme (100,000 iterations). In each iteration we case-resampled the cell count data, the BrdU incorporation data and the clone trajectory data and calculated the proliferation rate time-course, clone velocity at $-800 \mu\text{m}$ and initial growth fraction, GF_0 , from this resampled data. Then, in each iteration, these bootstrapped parameter values were used to estimate the activation rate k by fitting the model prediction of the growth fraction to the data using the LS method (Figure 3.14B). With that, I determined the value of the cell cycle entry rate as $k = (0.2 \pm 0.1) \text{d}^{-1}$. The growth fraction measurement of day 8 was excluded from the fit because its precise value would only affect the model prediction after this day. Now, as all parameters were estimated, an outgrowth trajectory was calculated for each iteration. The ensemble of all trajectories was used to calculate the confidence intervals of the model prediction (Figure 3.14C).⁵

Strikingly, the model predicts a time-course of spinal cord outgrowth which recapitulates the experimental data (Figure 3.14C). Please note, that the outgrowth data was not used to obtain the model prediction. The model parameters were all estimated by the quantification of cell behaviors in section 3.2.4. The fit-free agreement between the model prediction and the observed outgrowth time-course shows that acceleration

⁵The source code is available in the supplementary notebook "lg_model" under https://nbviewer.jupyter.org/github/fabianrost84/Rost-Rodrigo-Albors-et-al.-2016/blob/master/calculations/lg_model/lg_model.ipynb (Rost et al. 2016d).

of the cell cycle, activation of quiescent stem cells and an influx of cells quantitatively explain the observed time-course of spinal cord outgrowth.

To quantitatively determine the contribution of each cell behavior, we switched them off one by one *in silico*. The same approach was used for the model scenarios with individual mechanisms turned off (Figure 3.14D-G). Switching off the acceleration of the cell cycle leads to an outgrowth of less than 1.7 mm by day 8 due to the basal proliferation rate in the uninjured spinal cord, the influx of cells towards the amputation plane and the activation of quiescent stem cells (Figure 3.14D). This underestimates the experimental outgrowth which implies that the acceleration of the cell cycle is necessary to drive spinal cord outgrowth. In contrast, switching off cell influx nearly does not impact on the spinal cord outgrowth, implying that it is not a major driver of the regeneration process (Figure 3.14E). Similarly, switching off the activation of quiescent stem cells has only a small effect on regenerative spinal cord outgrowth (Figure 3.14F). Interestingly, when both, cell influx and cell activation are switched off the experimental spinal cord outgrowth time-course is still as we predicted, implying that acceleration of the cell cycle is sufficient to drive the regeneration process (Figure 3.14G).

Taken together, the model shows that the acceleration of the cell cycle in cells that were already proliferating in the uninjured spinal cord is the major driver of the observed spinal cord outgrowth.

3.2.6. APPLICATION OF THE MECHANISTIC MODEL TO PERTURBED REGENERATION

The mechanistic, mathematical model of regenerative spinal cord outgrowth given by eqs. (3.19) and (3.20) was set up to explain *normal* regeneration in terms of the underlying cell behaviors. For that, the contribution of each relevant cell behavior was quantified in section 3.2.4. To understand spinal cord regeneration on a molecular scale, regeneration has been perturbed on the molecular level using drugs like cyclopamine and retinoic acid or gene-knockouts like CRISPR-mediated knock-out of *Sox2*. (Fei et al. 2014; Pietsch 1993; Pietsch 1987; Schnapp et al. 2005).

One might ask whether the mechanistic model developed here, can be used to explain such conditions of *perturbed* regeneration. For that, it is important to note that the regulation of the cell behaviors are not explicitly considered in the presented modeling framework. Perturbing the cell behaviors on the molecular scale might lead to unexpected compensatory cell behaviors. It could even be the case that cell behaviors that were excluded to play a role in normal regeneration, like cellular rearrangements or apoptosis could play a role in perturbed regeneration conditions.

The rigorous strategy to understand perturbed conditions of regeneration in terms of the contribution of cell behaviors would therefore be the following: First, one would have to repeat the quantification of all cell behaviors like presented in section 3.2.3. In case other cell behaviors than proliferation, activation and cell flux play a role or their effects are spatially graded one would have to adopt the mathematical model accordingly.

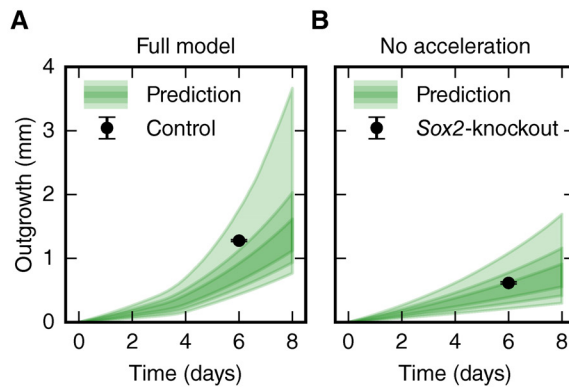


Figure 3.15.: Comparison of the spinal cord outgrowth prediction by our model with the measured outgrowth reported by Fei et al. (2014). **A**: Outgrowth prediction of the full model (green, same as in fig. 3.14C) and rescaled outgrowth in control condition (black dots, $n = 12$ axolotls). **B**: Outgrowth prediction of the model for the case that cell cycle acceleration is switched off (green, same as in fig. 3.14D) and rescaled, density corrected outgrowth in a Sox2-knockout condition (black dots, $n = 24$ axolotls).

Then, the model could be validated and the contribution of each cell behavior could be accessed similar to the way described in section 3.2.5. However, the quantification of each individual cell behavior is expensive. Nonetheless, if only some changes in cell behaviors are quantified the model can be used to access whether this change is sufficient to explain altered outgrowth kinetics using the assumptions that all other cell behaviors do not change. Notably, proliferation has been quantified to some extent for the perturbed conditions mentioned above. Here, I will apply our model to the Sox2 knockout condition reported by Fei et al. (2014) to access whether the quantified changes in proliferation can explain the altered outgrowth time-course.

Fei et al. (2014) showed that Sox2-knockout leads to shorter spinal cord outgrowth compared to control conditions. Control animals by Fei et al. (2014) showed less regenerative outgrowth than our 'normally' regenerating animals. This could be either due to their control CRISPR treatment or due to their reduced feeding. To account for the reduced growth, I assumed that all cell behaviors maintain the same relative contribution in Fei and colleagues' control as they have in normal regeneration. This assumption allowed linear rescaling of the outgrowth dataset from Fei and colleagues to match our 'normal' outgrowth dataset (Figure 3.9A).⁶ Furthermore, the authors found evidences that Sox2-knockout prevented the acceleration of the cell cycle during regeneration. As discussed above not all other cell behaviors that possibly could influence the observed spinal cord outgrowth were quantified by the authors. However, the authors quantified

⁶The source code is available in the supplementary notebook "lg_model" under https://nbviewer.jupyter.org/github/fabianrost84/Rost-Rodrigo-Albors-et-al.-2016/blob/master/calculations/lg_model/lg_model.ipynb (Rost et al. 2016d).

the number of neural stem cells per circumference. They found that fewer neural stem cells make up the circumference of *Sox2*-knockout spinal cords. Assuming that AP cell length is unchanged this means that cell density is decreased in this condition. Therefore, I corrected the outgrowth for the *Sox2*-knockout dataset to a density corrected outgrowth by

$$L_{corr} = \frac{N_S^{Sox2^{ko}}}{N_S^{control}} L, \quad (3.21)$$

where L_{corr} is the density corrected outgrowth, L is the measured outgrowth in the *Sox2*-knockout dataset and $N_S^{Sox2^{ko}}$ and $N_S^{control}$ are the mean number of neural stem cells per cross section in the *Sox2*-knockout and control condition, respectively (Figure 3.15B). Except for the cellular density, I assumed that *Sox2*-knockout only affects the acceleration of the cell cycle but that all other cell behaviors remain unaffected (i.e. compensatory mechanisms are not considered). If this assumption should be correct, then the 'No acceleration' scenario of the mechanistic outgrowth model should correctly predict the observed, density-corrected, outgrowth in the *Sox2*-knockout condition. Indeed, running our model with the acceleration of the cell cycle switched off recapitulated the shorter outgrowth in the *Sox2*-knockout condition (Figure 3.15B).

3.3. RESULTS: MUSCLE SEGMENT REGENERATION

3.3.1. CELL CYCLE ANALYSIS

In the previous section, I found that the accelerated proliferation in a 800 μm zone is the major driver of spinal cord regeneration. Similar quantitative approaches to understand regeneration in terms of the underlying cell behaviors could be performed in other tissues. An obvious candidate would be the surrounding muscle tissue in the axolotl tail, which we studied in Vincent et al. (2015).

Here, I will test whether the source zone of activated cells is of a similar length in the regenerating muscle and spinal cord tissue. For that, we performed proximal amputations at the level of the 16th myotome posterior to the cloaca, which is similar to location of the amputations in the previous section. Furthermore, we performed amputations at a more distal level (4th myotome posterior to the cloaca) to study how the location affects myotome regeneration (Figure 3.16). First, I estimate the cell cycle length and the growth fraction using the cumulative BrdU labeling method. Then, I estimate the size of source zone that harbors the cells that are responsible for the blastema growth.

The myotomes are formed from the mesenchymal blastema that forms adjacent to the regenerating spinal cord. Therefore, we measured the time course of the BrdU labeling fraction in the mesenchymal blastema (Figure 3.17A). I describe this time course with

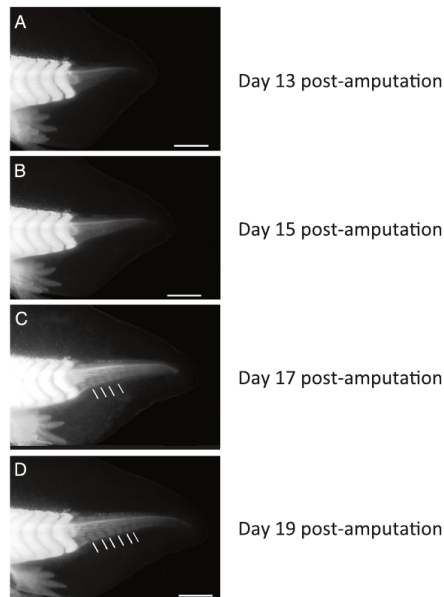


Figure 3.16.: Regeneration of chevron shaped muscle segments in axolotl. Photomicrographs of regenerating CAGGS:GFP transgenic axolotl tails. CAGGS:GFP is strongly expressed in muscle tissue. Amputation at 4th myotome posterior to the cloaca (proximal cut). **A**: No organized muscle tissue at day 13, yet. **B**: Myotome formation starts at day 15. **C,D**: More myotomes formed by day 17 and 19. White lines point at myotome boundaries. Scale bars: 2.5 mm.^a

^aReproduced from Vincent et al. 2015, Fig. 4.

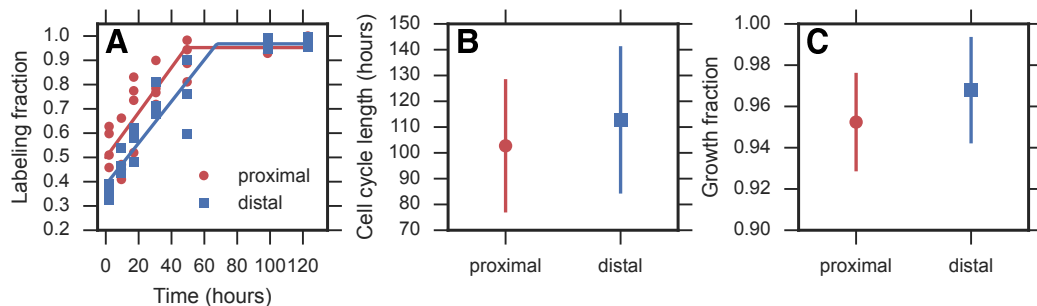


Figure 3.17.: Cell cycle analyses of day 10 mesenchymal tail blastemas after proximal and distal amputations in red and blue, respectively. **A**: Time course of BrdU labeling fraction during cumulative BrdU treatment starting at day 10. Each data point represents an individual animal (three to five per time point). Solid curves show model fits (using the model proposed by Nowakowski et al. (1989), see section 3.2.4 for an explanation of the method). **B,C**: Cell cycle parameters derived from model fits to the time courses of the BrdU labeling fraction. **B**: Cell cycle lengths, T_C . **C**: Growth fraction of proliferating mesenchymal cells, GF .

the model developed by Nowakowski et al. (1989), which is given by

$$R(t) = \begin{cases} GF \frac{t+T_S}{T_C} & t < T_C - T_S \\ GF & t \geq T_C - T_S \end{cases} \quad (3.22)$$

where $R(t)$ is the labeling fraction at time t , T_C is the cell cycle length, T_S is the S-phase length and GF is the growth fraction.

This model assumes 1) that all cycling cells within the analyzed section occur homogeneously distributed over the cell cycle phases and have identical cell cycle parameters, 2) a fixed total cell number and 3) a constant fraction of quiescent cells. To estimate the cell cycle parameters, I fitted the model using the method of least squares and determined parameter estimates and confidence intervals by bootstrapping (Figure 3.17B,C).⁷

The cell cycle lengths in both conditions are very similar with $T_C = (103 \pm 26)$ h for 10 day-proximal, $T_C = (112 \pm 29)$ h for 10 day-distal (Figure 3.17B). Also, the S-phase duration also was very similar for both conditions with $T_S = (54 \pm 17)$ h for 10 day-proximal and $T_S = (45 \pm 14)$ h for 10 day-distal. Nearly all cells were cycling with a growth fraction of $GF = (95 \pm 2)$ % and $GF = (97 \pm 3)$ % for proximal and distal amputations, respectively (parameters reported as mean \pm 68 % CI).

3.3.2. TOTAL NUMBER OF CELLS IN THE MESENCHYMAL BLASTEMA AND SIZE OF SOURCE ZONE

Next, we determined the total number of cells in the mesenchymal blastema at 10 days after amputation. We followed a similar strategy as described for the spinal cord in sections 3.2.4 and 3.2.4. First, we measured the mean cell nucleus length in AP direction which we found to be 22 μ m. Then, we measured the mean number of mesenchymal cells per cross section perpendicular to the AP axis. From that, we calculated the total number of cells in the mesenchymal blastema. Because the average nucleus in the blastema is approximately 22 μ m in diameter and each section was 10 μ m thick, the total number was divided by 2.2 to account for parts of each nucleus that extend over 2 or 3 consecutive sections and generated a $\frac{22}{10}$ higher apparent average nucleus count per section (Table 3.3). There are about 40 thousand and 22 thousand cells in the proximal and distal blastema, respectively.

Given the total number of cells at day 10 and the estimated cell cycle length, we can now estimate the progenitor pool size which is the minimal number of cells that gave rise to the blastema. To do so, I use a mathematical modeling approach. For this model, I assume that the cell cycle length is constant and that the blastema only grows due to cell divisions. Then, the increase in number of cells can be modeled with a Malthus

⁷Source code for calculations available under http://nbviewer.jupyter.org/github/fabianrost84/axolotl-calculations-phd/blob/master/axolotl_myotome.ipynb

	Proximal	Distal
Cell number in day 10 regenerate	39 982 ± 5024	22 154 ± 2862
Progenitor cell number	12 552 ± 1577	7485 ± 967
Cells at amputation plane	794 ± 88	376 ± 65
Distance from amputation plane	(348 ± 82) μm	(438 ± 132) μm

Table 3.3.: Progenitor cell number and spatial extent in blastema. Regenerated tails from proximal and distal blastemas were collected on day 10 post-amputation, fixed, cryosectioned and total mesenchymal cell numbers counted (for methods see Vincent et al. (2015)). The table compares the total cell counts, the calculated number of progenitor cells required to give rise to the total cell number within 10 days, the counted cell numbers within the amputation plane and the calculated spatial extent of the progenitor pools for both amputation levels. Despite several individual parameters differing between amputation levels, the distances the progenitor pools extend proximal to the amputation plane are similar within the confidence intervals.

growth model given by the ordinary differential equation

$$\frac{dN(t)}{dt} = \frac{\ln 2}{T_C} (N(t) + N_0 - N_q), \quad N(t = 0) = 0, \quad (3.23)$$

where $N(t)$ is the total number of cells in the regenerate at time t , N_0 is the progenitor pool size and N_q is the number of quiescent cells. The model eq. (3.23) is solved by

$$N(t) = (N_0 - N_q)(2^{\frac{t}{T_C}} - 1). \quad (3.24)$$

The number of quiescent cells can be calculated from the growth fraction, GF , and the total number of cells in the regenerate at day 10, $N_{\text{day } 10}$:

$$N_q = (1 - GF) (N_{\text{day } 10} + N_0). \quad (3.25)$$

Using eqs. (3.24) and (3.25), I find that the progenitor pool size can be estimated by

$$N_0 = N_{\text{day } 10} \frac{\left(1 + \left(\frac{1}{GF} - 1\right) 2^{\frac{t}{T_C}}\right)}{2^{\frac{t}{T_C}} - 1}. \quad (3.26)$$

Assuming the animal-to-animal variability in $N(t)$ to be the dominating source of uncertainty, I estimated the 68 % CI by linear error propagation:

$$\Delta N_0 = N_0 \left(\frac{\Delta N(t)}{N(t)} \right). \quad (3.27)$$

I found the number of cells in the progenitor pool to be about 13 thousand cells and 7

thousand cells in the proximal and distal blastema, respectively (Table 3.3).

Finally, I calculate the length of the source zone. This is the AP length of the zone that harbors all the cells from the progenitor pool. This length can be calculated by dividing N_0 by the nucleus density per AP length. The nuclear density per length is defined as the mean number of cells per cross section divided by the mean cell nucleus length in AP direction. The nucleus density per AP length differs between proximal and distal cut locations, mostly as a consequence of the 3D tail geometry. We counted the number of nuclei N_a in single $10\ \mu\text{m}$ thick sections at the amputation plane of each animal and divided the mean (reported in table 3.3) by the correction factor of 2.2 accounting for the same nuclei occupying multiple sections, see above. The progenitor zone length, L , is then obtained from

$$L = \frac{N_0}{\frac{N_a/2.2}{10\ \mu\text{m}}}. \quad (3.28)$$

The error estimates were propagated by adding the relative errors of input variables, hence

$$\Delta L = L \left(\frac{\Delta N_0}{N_0} + \frac{\Delta N_a}{N_a} \right), \quad (3.29)$$

and an additional error may result from the estimate of cell density per length. Interestingly, the minimal AP length of the source zone is similar for proximal and distal amputations with a length of about $400\ \mu\text{m}$ in both conditions (see table 3.3).

3.4. DISCUSSION

3.4.1. CELL BEHAVIORS DRIVING SPINAL CORD OUTGROWTH

Spinal cord tissue architecture is faithfully restored after tail amputation in the axolotl (Figure 3.4A). This unique regenerative capability relies on the neural stem cells covering the tube. Those stem cells re-activate a developmental program involving the PCP pathway enhancing cell proliferation while maintaining the tubular shape. How this massive and yet tightly controlled regenerative response takes place in the axolotl but does not occur in other species remained unknown.

In principle, regenerative spinal cord outgrowth could be controlled by mechanisms which conserve the number of stem cells. In those mechanisms, either cell size changes (Figure 3.7, left) or cells rearrange like in the PCP-oriented cell behavior responsible for convergence and extension (Figure 3.7, middle) (Wallingford 2012), a mechanism which is involved in the development of tube-like structures like kidney tubules in mice (Karner et al. 2009; Lienkamp et al. 2012) or spinal cord in the *Xenopus laevis* midgastrula (Keller et al. 1992a; Keller et al. 1992b).

Alternatively, outgrowth could be controlled by cell behaviors that change the number of stem cells (Figure 3.7, right). It was recently shown that apoptosis is negligible compared to proliferation during the regeneration of axolotl spinal cord (Rodrigo Albors et al. 2015).

Interestingly, this is consistent with recent quantitative results obtained in chicken spinal cord development (Kicheva et al. 2014). In this last study terminal differentiation was considered as a factor that determines the number of neural progenitors in a given spinal cord domain (Kicheva et al. 2014). This is not the case for early axolotl spinal cord regeneration since neurogenesis starts to occur not before 8 days post amputation (Rodrigo Albors et al. 2015). Theoretically, the number of stem cells could be increased by the dedifferentiation of neurons into neural stem cells. However, there is no evidence that this happens. Other mechanisms that could control spinal cord outgrowth by changing the number of stem cells in the regenerating zone are cell divisions, activation of quiescent cells and cell movements.

Here, I combined detailed quantitative datasets with mathematical modeling to dissect the contributions of the cell behaviors that underlie regenerative spinal cord outgrowth in axolotls. I found that the response to injury involves (i) changes in cell proliferation rate, (ii) activation of quiescent cells, and (iii) cell influx into the regenerating spinal cord, all while maintaining a surprisingly organized neural stem cell-scaffold. Modeling the contribution of each of these mechanisms to tissue outgrowth upon regeneration, I uncovered that the acceleration of the cell cycle is the main driver of regenerative spinal cord outgrowth in axolotls.

Increased proliferation of SOX2⁺ cells upon spinal cord injury is a common feature among vertebrates (Becker and Corral 2015, e.g.). In zebrafish (Hui et al. 2010; Hui et al. 2015), *Xenopus* (Gaete et al. 2012), mouse (Lacroix et al. 2014) and axolotl (Holtzer 1956; Rodrigo Albors et al. 2015) traumatic spinal cord injury triggers a long-range wave of increased cell proliferation. It is however clear that although the potential to replace lost cells or tissue exists in other species, they are not as efficient as axolotls at resolving spinal cord injuries. A more comprehensive characterization of cell proliferation responses is thus needed to understand fundamental differences between species of different regenerative capabilities. In a previous study, we uncovered that spinal cord stem cells speed up their cell cycle during regeneration (Rodrigo Albors et al. 2015). Performing detailed quantifications in the axolotl, I was able to delineate a high-proliferation zone that initially spans from the 800 μm adjacent to the amputation plane to the regenerating tip, and later shifts posteriorly, as the spinal cord regrows. By performing experiments *in silico* using my mechanistic model of spinal cord regeneration I demonstrated that the acceleration of the cell cycle can explain the observed spinal cord outgrowth.

3.4.2. UNDERSTANDING OF PERTURBED REGENERATION

Furthermore, I applied the model to an independent experimental dataset in which *Sox2*-knockout spinal cords do not regrow properly upon amputation (Fei et al. 2014). *Sox2*-knockout cells express PCNA which indicates that they are able to proliferate, but their lower incorporation of the thymidine analog 5-ethynyl-2'-deoxyuridine (EdU) suggests that they cannot speed up the cell cycle (Fei et al. 2014). I was able to show that the reduced outgrowth in *Sox2*-knockout spinal cords can be quantitatively explained

by the lack of cell cycle acceleration (Figure 3.15). However, it is important to point out that my model does not include the regulation of individual cell behaviors and thus it does not consider possible compensatory mechanisms that may operate under perturbed conditions. Hence, each cell behavior has to be quantified for each perturbed regeneration condition to rigorously apply the presented model framework. To apply my model to the *Sox2*-knockout dataset, I assumed that knocking out *Sox2* only affects the acceleration of the cell cycle. The fact that the model successfully recapitulated the experimental outgrowth in the *Sox2*-knockout scenario suggests that compensatory mechanisms might have only a small contribution in this condition.

The application of the model to the *Sox2*-knockout condition demonstrates how my model of spinal cord outgrowth (Figures 3.14 and 3.15) can be used to mechanistically understand how cell behaviors change the regenerative outgrowth in perturbed regeneration conditions. To consolidate the understanding of the *Sox2*-knockout, the assumptions I made for this particular analysis must be tested. This could be done by performing a detailed quantification of the possibly involved cell behaviors as presented in this chapter for the unperturbed regeneration.

The same strategy could also be applied to understand other perturbed regeneration conditions. Blocking hedgehog signaling or treatment with retinoic acid have been reported to impair regenerative outgrowth (Pietsch 1993; Pietsch 1987; Schnapp et al. 2005). How are the underlying cell behaviors affected in these conditions? For both conditions a decrease in proliferation and outgrowth is reported. This is in qualitative agreement with my finding that the acceleration of the cell cycle can explain the observed spinal cord outgrowth. Unfortunately, the stem cell density has not been quantified in neither of those conditions. This is what hindered me to also test the applicability of my mechanistic model to these conditions here.

3.4.3. THE CELL PUSHING MECHANISM

By analyzing cell tracks during regeneration, I found that cells move along the AP axis of the spinal cord but maintain their relative position: cells move faster the closer they are to the amputation plane (Figure 3.13B,C). In line with earlier work (Mchedlishvili et al. 2007), I found that cells initially located within the 500 μm anterior to the amputation plane move fast enough to contribute to the regenerated spinal cord; while cells outside this zone move slower, and cells at 800 μm , the border of the high-proliferation zone, almost do not move. This is consistent with a conceptual model in which cells are passively displaced, pushed by more anterior dividing cells. In this model, the more posterior a cell is the more cells anterior to that cell divide and the stronger is the push, making the cell move faster (Figure 3.18). Importantly, the proliferative response extends beyond the 500 μm anterior to the amputation plane that gives rise to the regenerated spinal cord (Mchedlishvili et al. 2007). In the light of this model, it is plausible that cells in the posterior 500 μm of the high-proliferation zone produce the regenerated spinal cord posterior to the amputation plane. Simultaneously cells from the anterior 300 μm of the

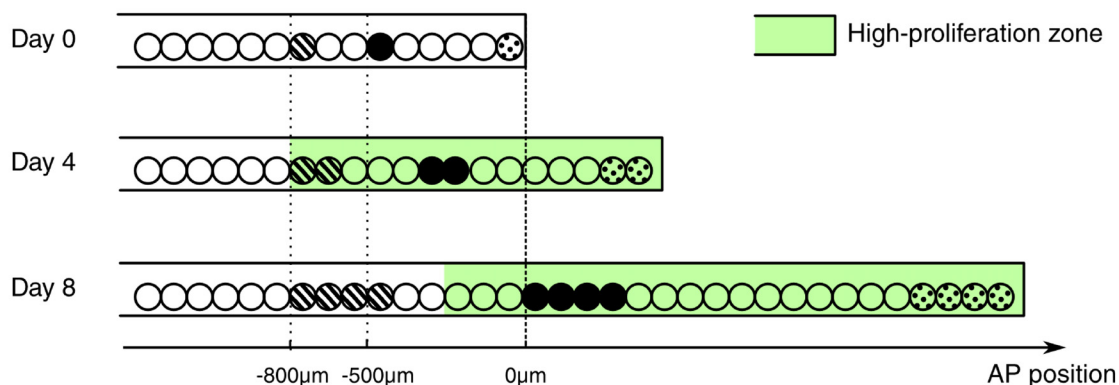


Figure 3.18.: Conceptual model of spinal cord growth during regeneration. Anterior is to the left. Only one row of stem cells is shown as circles. Three cell clones are marked with different patterns (striped, black and dotted). In the uninjured spinal cord (Day 0), cells divide at a slow, basal proliferation rate (white background). From day 4 after amputation, cells speed up their cell cycle and the growth fraction increases, within a high-proliferation zone that initially extends 800 μm anterior to the amputation plane (green background). The density of neural stem cells along the spinal cord stays constant and spinal cord outgrowth is achieved by an increase in the total number of neural stem cells. The major driver of this increase in cell number is the acceleration of the cell cycle in the high-proliferation zone. Cells might just be displaced by the pushing of cells dividing anterior to them. The more posterior a cell is the more cells anterior to that cell divide and push the cell making it move faster: While an anterior clone (striped) hardly moves, clones in the center of the high-proliferation zone (black) move faster. Clones that start at the amputation plane (dotted) stay at the tip of the regenerating spinal cord and move fastest.

high-proliferation zone replenish and push out the posterior 500 μm .

3.4.4. COMPARISON OF REGENERATION PARAMETERS IN SPINAL CORD AND MUSCLE

In section 3.3, I studied the regeneration of the myotomes. There, proximal and distal amputations were performed. The distal amputations were performed at a similar AP location as the amputations made for the study of spinal cord regeneration. I found the cell cycle lengths to be similar for proximal and distal amputations with a growth fraction of nearly 1 (Figure 3.17). Interestingly, the cell cycle length is about 4 to 5 days for the mesenchymal blastema cells and the neural stem cells at day 8 and day 10, respectively (Figures 3.11 and 3.17).

Surprisingly, I found comparable source zone lengths of about 400 μm for proximal and distal amputations while the involved number of progenitor cells was significantly higher for proximal amputations (Table 3.3). Given the fact that the source zone length in the mesenchymal blastema is of the same order as the length of the high-proliferation zone in the spinal cord, one might speculate that similar signaling mechanisms are at work to instruct those tissues to perform regeneration. Candidates for the identity of such a signal are the WNT, FGF and retinoic acid pathways which are involved in paraxial mesoderm development (Aulehla and Pourquié 2010). Inhibition of Wnt/beta-catenin or FGF signaling stops tail regeneration in *Xenopus* tadpoles and Wnt/PCP signaling is required for proper spinal cord regeneration in axolotl (Lin and Slack 2008; Rodrigo Albors et al. 2015). On the other hand, administration of retinoic acid inhibits axolotl tail regeneration and reduces the mitotic activity in the spinal cord (Pietsch 1993; Pietsch 1987). Whether these factors are actually involved in the specification of the progenitor zone sizes in the regenerating spinal cord and muscle segments has to be addressed in future studies.

Please note, that the estimate for the mesenchymal blastema source zone length was a rather rough estimate where I ignored a number of cell behaviors. Their influence could be estimated in future studies using a similarly detailed approach as we used for the study of spinal cord regeneration.

3.5. CONCLUSION

In this chapter, I asked what are the underlying cell behaviors that drive the regenerative spinal cord outgrowth during the first 8 days after tail amputation. After quantifying the spinal cord outgrowth, I analyzed the data with a first naive model that assumed proliferation as the only driver of the outgrowth. This initial analysis showed that a model involving a biphasic proliferation response, initially slow and accelerated from about 3 days after amputation could explain the outgrowth well. Then, I went on to quantify all possibly involved cell behaviors. I found a constant density of stem cells along the

AP axis which indicated that convergence and extension movements of cells are not important. A detailed analysis of the proliferation pattern in space and time revealed that the predictions of the first naive model would hold true: the cell cycle is accelerated between 3-4 days in a high proliferation zone initially spanning from 800 μm anterior to the amputation plane. Furthermore, I also revealed contributions by the activation of quiescent stem cells and a cell influx into the high-proliferation zone. I developed a mathematical model of spinal cord outgrowth involving all these cell behaviors. With the model, I could show that the involved cell behaviors can quantitatively explain the observed outgrowth. Performing *in silico* experiments, I could identify the acceleration of the cell cycle as the major driver.

I also studied the regeneration of the adjacent muscle tissue. This tissue rebuilds the correct number of myotomes and those myotomes acquire their typical chevron-shape. A comparison between the spinal cord and the adjacent muscle tissue showed that cell cycle parameters and source zone lengths are similar in both tissues. The similar zone length could be a hint to a similar underlying signaling mechanism.

The findings presented in this chapter highlight the importance and potential of careful quantification of cell proliferation and of mathematical modeling to understand the mechanisms of regeneration. Moreover, the careful spatial and temporal characterization of cell proliferation helps to focus the search for key signals that might be operating in the high-proliferation zone to speed up the cell cycle of regenerative neural stem cells. It will be interesting to see whether the expression of AxMLP, the recently identified regeneration-initiating factor in axolotls (Sugiura et al. 2016), correlates in time and space with the high-proliferation zone.

Notably, the increase in cell numbers during regeneration is tightly regulated such that the regenerating spinal cord extends with constant cell density and its proper tube-like structure. This structure which is formed mostly of neural stem cells might be essential to act as a basis for rebuilding the complete spinal cord tissue architecture. Previously, we showed that the activation of PCP signaling within the source zone instructs cells to divide along the growing axis of the spinal cord and is key for effective spinal cord regeneration (Rodrigo Albors et al. 2015). This work highlights the importance of orderly and directed expansion of the neural stem cell pool for efficient spinal cord regeneration.

My findings provide a quantitative, mechanistic understanding of the cell behaviors that drive complete spinal cord regeneration in axolotl. By combining a quantitative modeling approach with quantitative experimental data, I have established that axolotl spinal cord outgrowth is driven by the acceleration of cell proliferation in a pool of SOX2⁺ neural stem cells restricted in space and time. Whether this peculiar spatiotemporal proliferative pattern is restricted only to the axolotl and how this correlates with amputation-induced signaling pathway activation remain to be elucidated.

4. DEVELOPMENT OF MUSCLE SEGMENTS IN ZEBRAFISH

4.1. INTRODUCTION

In the previous chapter, I studied the regeneration of the axolotl spinal cord and the adjacent muscle segments. Remarkably, those muscle segments also regenerate their folded shape (Figure 3.16). In this chapter, I study the shaping of muscle segments in the developing zebrafish. My quantification and model driven data analysis laid the foundation for the understanding of the shape changes as published in Rost et al. (2014). The folded shape of the muscle segments is termed chevron shape and it resembles the familiar shape of fish bones (Figure 4.1). The chevron shape is thought to be optimal for the undulating body movements of swimming (van Leeuwen 1999; van Leeuwen et al. 2008). However, the mechanism that shapes the chevron during embryogenesis is not understood.

Here, I used time-lapse movies of developing zebrafish embryos spanning the entire somitogenesis period to quantify the dynamics of chevron shape development. By comparing such time courses with the start of movements in wildtype zebrafish and analyzing immobile mutants, I show that the previously implicated body movements do not play a role in chevron formation. Further, the monotonic increase of chevron angle along the anteroposterior axis revealed by my data analysis constrains or rules out possible contributions by other previously proposed mechanisms. In particular, I show that muscle pioneers are not required for chevron formation. I test the tension-and-resistance mechanism that I proposed previously (Rost 2010). This mechanism involves interactions between intra-segmental tension and segment boundaries. To evaluate this mechanism, I derived and analyzed a mechanical model of a chain of contractile and resisting elements. Here, the predictions of this model are verified by comparison with experimental data. Altogether, my results support the notion that a simple physical mechanism suffices to self-organize the observed spatiotemporal pattern in chevron formation.

In this chapter, I first introduce what was already known about chevron shape forma-

tion in zebrafish and other species and continue reviewing the previously suggested mechanistic explanations of the shape changes. In the results section, my first goal is to quantify time-lapse light microscopy movies of chevron formation for mobile, immobile and muscle pioneer-ablated zebrafish embryos. My second goal is to test previously proposed mechanisms of chevron formation. I will find that the data disprove three of the four previously hypothesized mechanisms. My third goal is to test the tension-and-resistance mechanism for which chevrons form collectively. I will show that it is in qualitative agreement with the data. I suggest further tests and extensions of my model and briefly discuss my results in the light of evolution.

4.1.1. CHEVRON SHAPE OF MUSCLE SEGMENTS

All chordates have metameric muscle segments that are critical for locomotion. These muscles are termed myotomes, and their characteristic shape in aquatic species is referred to as chevron (Figure 4.1) (Bone 1978; Kimmel et al. 1995). Typically, one observes three folds in sagittal sections of adult fish like salmon and zebrafish (Agassiz and Vogt 1845; Greene and Greene 1913; Maurer 1913; Videler 1993), but there can be up to six (Harder 1964a; Harder 1964b). The oldest known fossils with chevrons are *Pikaia* (Morris and Caron 2012) and *Haikouichthys* (Shu et al. 1996). They are present in *Amphioxus* (Bone and Moore 2008; Hatschek 1882; Hatschek 1893; Nursall 1956), the most basal extant chordate (Delsuc et al. 2006), the agnathan Lamprey (Langelaan 1904; Nursall 1956; Wickström 1897), the tadpole of the anuran *Xenopus* (Harrison 1898; Von Seckendorff Hoff and Wassersug 1986) and in salamander larvae (Bordzilovskaya et al. 1989; Francis 1934; Gegenbaur 1859; Mchedlishvili et al. 2007).

The myotome's locomotory function has been conserved for at least 500 million years (Bone and Moore 2008), suggesting that the chevron shape has been optimized for this function (Bone 1978; Videler 1993). Chevron shape and function are used to infer evolutionary relationships among chordates (Lacalli 2012; Mallatt and Holland 2013; Morris and Caron 2012). The mechanics of chevron-shaped myotomes during swimming has been studied extensively for over a century (Alexander 1969; Chevrel 1913; Nursall 1956; Rauther 1940; Van der Stelt 1968; van Leeuwen 1999; van Leeuwen et al. 2008; Videler 1993; Willemse 1966; Wunder 1936). However, the development of the chevron remains poorly understood.

How does the chevron pattern emerge during embryogenesis? I address this question in the zebrafish *Danio rerio*. Its embryo facilitates investigation of morphological changes, notably somitogenesis (Durbin et al. 2000; Henry et al. 2005; Holley et al. 2000; Schröter et al. 2012; Schröter et al. 2008; van Eeden et al. 1996), myotome differentiation (Cortés et al. 2003; Currie and Ingham 1996; Daggett et al. 2007; Devoto et al. 1996; Henry and Amacher 2004; van Raamsdonk et al. 1978; van Raamsdonk et al. 1974a; Yin and Solnica-Krezel 2007), and chevron formation (van Raamsdonk et al. 1979; van Raamsdonk et al. 1977; van Raamsdonk et al. 1974a; van Raamsdonk et al. 1974b). As early development progresses, somites sequentially bud off the unstructured paraxial

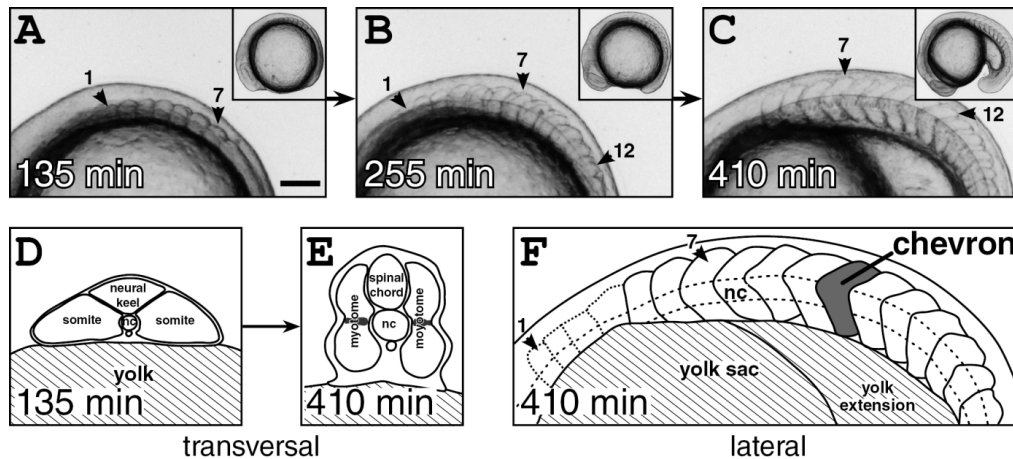


Figure 4.1.: Trunk and segment morphology of a developing zebrafish embryo. **A-C**: Lateral views of a developing zebrafish embryo from a representative time-lapse movie (Movie 1 in supplementary material to Rost et al. (2014)). Anterior is to the left. Arrowheads mark segments 1, 7 and 12. Insets show entire embryo. Scale bar 100 μ m. **A**: 7 cuboidal segments have formed. **B**: 12 segments have formed. Segment 1 is cuboidal, segment 7 already has chevron shape, the most recently formed segment 12 still is cuboidal. **C**: 18 segments have formed. Segment 12 now is chevron shaped. **D, E**: Illustrations of transversal sections of the anterior trunk at the level of segment 7. (Copyright 2000 Wiley. Modified and used with permission from Stickney et al., 2000). **D**: At the time of somite formation (segment 7 as representative), the trunk is initially flattened and medio-laterally extended, with the notochord (nc) in the middle. **E**: Later, when the segment has completed the rapid morphogenesis of the chevron, the trunk is dorso-ventrally extended. The shaded regions in the middle of the segment indicate the position of the muscle pioneers. **F**: Sketch of **C**. Visible segment boundaries are shown as solid lines and the poorly visible boundaries of the first 4 segments as dotted lines. One chevron-shaped segment is marked in gray. The notochord (dashed line) intersects the apices of the chevrons.^a

^aReproduced from Rost et al. 2014, Fig. 1.

mesoderm (Figure 4.1A-C, Movies 1,2 in supplementary material to Rost et al. (2014)¹) and commit most of their cells to myotome formation, thereby respecting and further enforcing tissue segmentation (Kimmel et al. 1995; Morin-Kensicki et al. 2002). I will use the generic term segment for both, somite and myotome (Figure 4.1D,E).

In zebrafish, about 35 segments form within approximately 15 hours (Schröter et al. 2008). Initially, segments appear as cuboidal blocks (Figure 4.1A). The anterior-most segments retain their cuboidal shape, more posterior segments deform into V-shaped chevrons with their apex pointing anteriorly. However, reports differ as to the number of segments that remain cuboidal (from 5-6), and the timing of chevron formation (starting when 7 or 12 segments have formed) (van Eeden et al. 1996; van Raamsdonk et al. 1974a). Van Raamsdonk et al. (1974a) reported that segments 5-12 deform simultaneously. Tail segments (18-35) start to deform immediately after each somite formed (van Raamsdonk et al. 1974a). The timing and the extent of shape changes of segments 13-17 have not been reported. Three weeks after hatching, W-shaped myotomes emerge. (van Raamsdonk et al. 1974a). Pioneering quantitative work measured the chevron angles of the anal segment for different time points (van Raamsdonk et al. 1979). Together, these findings indicate temporal and spatial heterogeneities but their quantification is incomplete. Hence, my *first* of three goals is to provide a conclusive description of chevron formation by quantifying time-lapse movies of developing zebrafish embryos. With these quantitative data, I will test competing mechanistic hypotheses of chevron formation which I will review in the next section.

4.1.2. SUGGESTED MECHANISTIC EXPLANATIONS FOR THE CHEVRON'S EMERGENCE

Here, I review five previously proposed, competing hypotheses seeking to explain chevron formation, namely body movements, templating of the chevron from the posterior border of the head, relative tissue movements, differential growth or tonic muscle tension associated to muscle pioneer cells, and self-organization by mechanical forces.

The processes driving chevron formation during embryogenesis and larval stages were first investigated in the 1970s by van Raamsdonk and colleagues (van Raamsdonk et al. 1979; van Raamsdonk et al. 1977; van Raamsdonk et al. 1974a; van Raamsdonk et al. 1974b). Given the accepted importance of the chevron shape for locomotion, they suggested that the undulating lateral movements that herald the onset of locomotion play a role in the morphogenesis of the chevron (te Kronnié 2000; van Raamsdonk et al. 1979; van Raamsdonk et al. 1977; van Raamsdonk et al. 1974a). Van Raamsdonk and colleagues tested this hypothesis by immobilizing young fish with developed chevrons through removal of the brain, damage of midbody somites or fixation in agar (van Raamsdonk et al. 1979; van Raamsdonk et al. 1977). They observed a slight straightening of the chevron angles. The fish recovered the normal pattern when it could move again.

¹<http://jeb.biologists.org/content/jexbio/suppl/2014/10/23/217.21.3870.DC1/JEB102202.pdf>

Independently, and arguing against a strong role for swimming movements in chevron development, the genetically immobile homozygous *nic^{b107}* mutant zebrafish forms chevrons (Schröter et al. 2008; van der Meulen et al. 2005). However, this formation has never been quantified. Thus, a contribution from movement to the dynamics of chevron formation, or the final angle of the chevron, may yet be present.

Independent of motion, a templating hypothesis for chevron formation posits that the posterior border of the head already possesses the chevron shape, and this pattern can be passed to the next segment. Muscle cells may simply grow to a predefined size, so that when the muscle cells connect to the next segment's anterior boundary this segment would also form a chevron (van Raamsdonk et al. 1979). Unless interrupted, this pattern would be passed sequentially into the tail. Inconsistent with templating as the sole determinant, chevrons develop immediately posterior to segments with experimentally disrupted shapes (Riedel-Kruse et al. 2007; Windner et al. 2012). However, a contribution to the final shape by templating is not ruled out.

Another hypothesis features relative movement of structures in the embryo (Turner 2007). The myosepts were proposed to attach to the notochord to be pulled into chevron shape. This hypothesis can be tested by time-lapse microscopy.

Tonic muscle contraction and differential growth within the myotome have also been considered as potential mechanisms (van Raamsdonk et al. 1979). The earliest developing muscle fibers, the muscle pioneers, elongate in concert with the formation of chevrons (Kimmel et al. 1995). Mutants that fail to differentiate muscle pioneers do not have normal V-shaped chevrons when examined at larval stages, instead displaying a U-shaped chevron (Halpern et al. 1993; te Kronnié 2000; van Eeden et al. 1996). It is thus now widely believed that the muscle pioneers or the myoseptum are responsible for the chevron shape (Dolez et al. 2011; Koumans and Akster 1995; Meyers et al. 2013), but this has not been directly tested, and a mechanism whereby these cells would cause the chevron shape has not been proposed.

In summary, these four hypotheses represent a range of mechanisms that are not mutually exclusive, but for which there is currently no conclusive experimental support. My *second goal* is to test these competing hypotheses. I will achieve this after I achieved my first goal, the conclusive quantification of chevron formation. Then, I can compare the predictions of these four competing hypotheses to the quantitative data.

Independent of which, if any, of these proposed mechanisms will be confirmed, morphogenesis of the chevron is ultimately executed by mechanical forces. These might either act (1) *autonomously* in each segment in a segment-specific and genetically encoded manner. Alternatively, by analogy to chevron patterns in abiotic systems such as rock formations in geology (Bayly 1974) and polymers and liquid crystals in material science (Read et al. 1999; Singer 1993), the chevron might emerge (2) *collectively* as a result of force fields across the tissue with initially homogeneous properties and without the need to invoke genetically encoded and segment-specific properties. Previously, I hypothesized that the latter scenario is true (Rost 2010). I put forward a tension-and-resistance mechanism to describe the force field in the shaping segments. I formalized

this putative mechanism in a mathematical, mechanical model. My *third goal* is to test the latter scenario by comparing the mechanical model predictions with the quantitative data.

4.2. RESULTS

4.2.1. QUANTIFICATION OF CHEVRON FORMATION IN MOBILE EMBRYOS

I quantified chevron formation using time-lapse imaging of embryos from incrosses of free spawning heterozygous *nic^{b107}* parents (Herrgen et al. 2009; Schröter et al. 2008). Wildtype and heterozygous *nic^{b107}* mutant zebrafish show undulatory swimming movements (Movie 1 in supplementary material to Rost et al. (2014)) whereas the homozygous *nic^{b107}* mutant remains still throughout the observation period (Movie 2 in supplementary material to Rost et al. (2014)). I will refer to homozygous *nic^{b107}* mutant embryos as “immobile”, and to both, wildtype and heterozygous *nic^{b107}* embryos, as “mobile”. I analyzed time-lapse microscopy movies of 3 mobile and 5 immobile zebrafish from the beginning of segmentation until the end of chevron formation. I will first focus on mobile embryos.

The embryos were oriented laterally, affording a view of the segmenting paraxial mesoderm in which the forming straight somite boundaries could be seen reliably (Figure 4.1A). As the somites matured into myotomes and changed their shape from a cuboidal block to a chevron, I could observe the deformation of segments (Figure 4.1B,C). Through this 16 h time window, the overall shape of the embryonic axis deformed as the segmenting mesoderm converged from a flattened medio-laterally extended cross section (Figure 4.1D) to a dorso-ventrally extended cross section (Figure 4.1E). In each time-lapse frame, the medially located notochord was visible as a reference line that intersected with the apex of the forming chevron (Figure 4.1F).

To quantitate the emergence of the chevron shape, I estimated α , the angle between the dorsal segment boundary and the dorso-ventral axis (Figure 4.2B) as described in section 2.3.1. The chevron angle, α , is 0° for cuboidal segments and an increase in α indicates chevron formation. I show these data for segment 1, 7, and 15 from a representative embryo in figs. 4.2C-E. Due to high contrast of the yolk edge, the anterior-most segments were difficult to follow leading to gaps in the time series (Figure 4.2C). In contrast, more posterior segments yielded near-continuous time series of chevron angle values until the start of occasional movements at (7.3 ± 0.2) h also introduced intermittent gaps (gray regions in figs. 4.2C-E, Movie 1 in supplementary material to Rost et al. (2014)).

The anterior-most segment did not form a chevron (Figure 4.2C). Strikingly, the chevron angle of segments 7 and 15 changed smoothly over a time interval of about 2 hours before reaching the final chevron shape, which remained constant until the end of recording (Figures 4.2D,E).

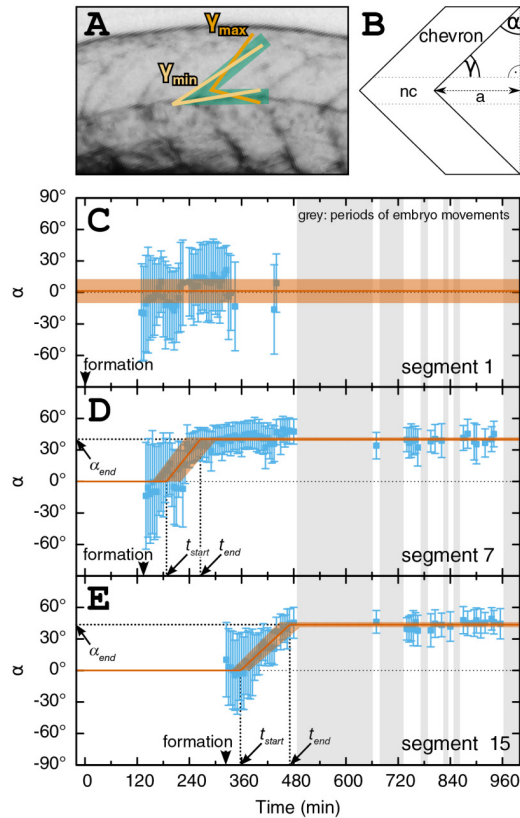


Figure 4.2.: Measurement of changing chevron angles for representative anterior and posterior segments **A**: Measurement of the chevron angle. The green area marks the posterior segment boundary and the dorsal notochord boundary in the maximum projection from a z-stack. The light and dark orange lines mark the measured angles γ_{min} and γ_{max} , respectively. **B**: Sketch of a bent segment boundary showing the geometrical relation between γ and chevron angle α . Measured angles γ were transformed into α (see section 2.3.1). For straight boundaries α is 0; $\alpha > 0$ indicates a bent boundary. **C-E**: Blue: Angle measurements for segments 1, 7 and 15 of the embryo shown in fig. 4.1 as a function of time. The error bar shows the 68% confidence interval. Thin dotted black line shows $\alpha = 0$, meaning no chevron. Grey shaded intervals indicate lack of data due to autonomous movements of the animal. **C**: Segment boundary 1 stays straight (on average $\alpha = (1 \pm 11)^\circ$, shown in orange). **D, E**: Segment boundaries 7 and 15 form a chevron. Arrowheads mark segment formation time. The fit with the empirical model of chevron angle time course (Figure 4.3) is shown in orange with the uncertainty of the fit depicted by the transparent orange area. The 3 model parameters are indicated by thick dotted lines. **D** $t_{start} = (187 \pm 33)$ min, $t_{end} = (265 \pm 34)$ min, $\alpha_{end} = (40 \pm 2)^\circ$. **E** $t_{start} = (357 \pm 21)$ min, $t_{end} = (471 \pm 24)$ min, $\alpha_{end} = (44 \pm 2)^\circ$.^a

^aReproduced from Rost et al. 2014, Fig. 2.

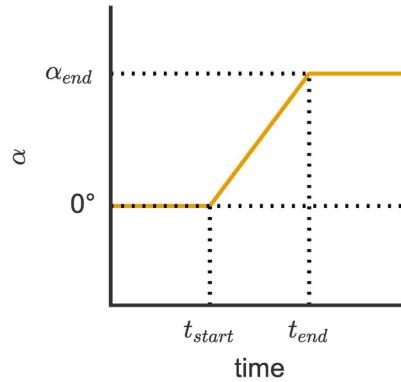


Figure 4.3.: Empirical model of chevron angle time course. The chevron shape change is described with angle α over time. For a straight segment boundary, $\alpha = 0^\circ$ (see fig. 4.2B). In the model I assume all segments start with straight boundaries, hence $\alpha = 0^\circ$, initially. Then, in the time interval from t_{start} to t_{end} the chevron is formed. I assume, that the angle increases linearly. Afterwards, the final chevron angle, α_{end} , remains unchanged.

4.2.2. EMPIRICAL MODEL TO SUMMARIZE CHEVRON ANGLE TIME COURSE

In the previous section I described the results of the chevron shape quantification for 3 segments of one fish. However, as I quantified the chevron angles for 15 segments in 3 mobile and 5 immobile fish, I sought to summarize this data by a smaller number of characteristic parameters. Therefore, I employed the fitting of an empirical model of the shape change as described in detail in this section.

Based on the data for each single segment, I identified non-chevron-forming segments as those for which most of the measured angles α were close to 0° (see section 2.2.2). For them, I calculated the final angle α_{end} as the mean of all measured angles (Figure 4.2C, orange). To capture the dynamic behavior of each chevron-forming segment in a compact and informative manner, I described the change in the chevron angle over time with an empirical model involving three parameters (Figure 4.3): α_{end} , the final chevron angle, where $\alpha_{end} = 0^\circ$ means no chevron formation and a typical posterior chevron has $\alpha_{end} \approx 40^\circ$; as well as the time points at which chevron formation started, t_{start} , and ended, t_{end} . These parameter values were determined for each segment by fitting the empirical model to the chevron angle time series (Figure 4.2D,E, see section 2.2.2). I restrict my analysis to trunk segments 1 to 15, as the values for the final chevron angle, α_{end} , did not change appreciably in segments 16 to 30 when compared to segments 8 to 15 (data not shown).

Segment	1	2	3	4	5	6	7	8	9	10	11	12	13	14	15
Mobile (%)	0	0	0	100	100	100	-	100	100	-	100	100	100	100	-
Immobile (%)	0	0	-	80	100	100	100	100	100	100	100	100	100	100	100

Table 4.1.: Percentage of embryos showing significant chevron formation. Only segments for which the fitting gave significant results can be considered as significantly chevron-forming segments (blue columns, segments 4-15), for the definition see section 4.2.2. Segments are marked red if none of the quantified individuals could be identified as significantly chevron-forming (segments 1-2). An unambiguous classification of segment 3 could not be achieved as it would require more individuals and more time points to be quantified. Number of individuals n is 3 to 5. Dash indicates $n < 3$, result not valid.

4.2.3. QUANTITATIVE DESCRIPTION OF CHEVRON FORMATION

Here, I derive the conclusive, quantitative description of chevron formation. I use the results derived by fitting the empirical model that I introduced in section 4.2.2 to the chevron angle data. For all quantified time series of mobile and immobile zebrafish, I first assessed which segments along the axis showed robust chevron formation. For segments 1 to 2, I did not observe embryos with significantly chevron-forming boundaries, regardless of mobility (Table 4.1).

For both mobile and immobile embryos, segment boundaries deform significantly at segments 4-15 (Table 4.1). I conclude that the 2 anterior segments do not form chevrons and that the transition from block-like to chevron-shaped myotomes occurs at segment number 3.

For segments 4-15, 96% of the datasets were of sufficiently high quality so that the result of the model fitting was accepted and these values are plotted in fig. 4.4. For mobile embryos (green symbols), the deformation of boundaries of segments 4-7 starts nearly simultaneously, whereas the boundary deformation of segments 8-15 starts sequentially and with a small offset after the formation of the segment boundary (Figure 4.4A, green symbols). Boundary deformation of all quantified segments in mobile embryos ceased (2 ± 1) h after chevron formation start (Figure 4.4A,B, green symbols). The data for the final chevron angle group the segments in a similar way as the chevron formation start time: Whereas the final chevron angle monotonically increases for segments 1-7, the more posterior segments homogeneously acquire $(40 \pm 3)^\circ$ (Figure 4.4C, green symbols).

Complementing previous studies of chevron shape in late developmental stages with established chevrons (van der Meulen et al. 2005; van Raamsdonk et al. 1979; van Raamsdonk et al. 1977; van Raamsdonk et al. 1974a), the results here represent the first quantitative measurements of the dynamics of chevron formation in any species. Therewith, the first goal of this chapter, the conclusive quantification of chevron formation, has been reached and I can now compare the data to the predictions of hypothetical mechanisms for chevron formation.

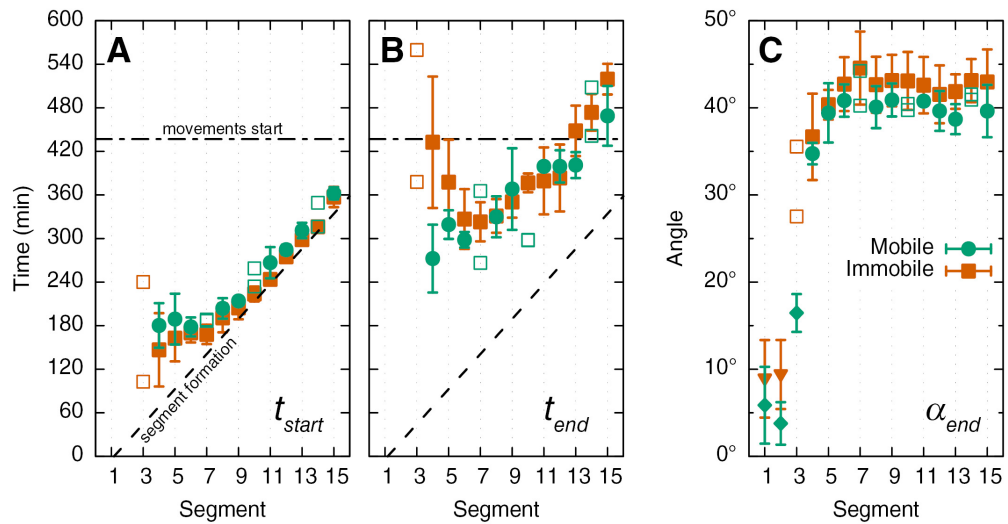


Figure 4.4.: Chevron formation for mobile and immobile embryos. **A-C**: Filled symbols with error-bars depict mean and standard deviation (number of animals n is 3 to 5) for the fit parameters (A) chevron formation start time t_{start} , (B) end time t_{end} , and (C) final chevron angle α_{end} as a function of segment index, respectively. In case $n < 3$, single measurements are plotted as open symbols. Green circles, mobile embryos; orange squares, immobile embryos. **A, B**: The solid black curve indicates somite formation times (Schröter et al. 2008). The horizontal dash dotted line denotes the average onset of autonomous movements. **C**: Additional to the fitting results, the mean angles for non-chevron-forming segments are shown as green diamonds and orange triangles for mobile and immobile embryos, respectively^a.

^aReproduced from Rost et al. 2014, Fig. 3.

4.2.4. ROLE OF BODY MOVEMENTS

To test whether the normal undulating body movements resulting from rhythmic muscle contractions have an influence on early chevron formation, as has been previously proposed (van Raamsdonk et al. 1979; van Raamsdonk et al. 1977; van Raamsdonk et al. 1974a), I can now use the data to quantitatively relate the dynamics of chevron formation and the start of movements. As expected (van Raamsdonk et al. 1974a), I find that movements start after the anterior segments 4-17 have already started to deform (Figure 4.4A, Movie 1 in supplementary material to Rost et al. (2014)). Hence, movements are not required to start chevron formation. Segments 4-13 had finished chevron formation already before movements start in wildtype embryos.

To what extent movements contribute to chevron formation dynamics and to setting the final chevron angle can also be determined by comparison to non-moving embryos. Ideally suited for this purpose, the *nic^{b107}* mutant has a lesion in the nicotinic cholinergic receptor that prevents neurotransmitters of motor neurons from activating muscle contraction, consequently paralyzing the embryo (Sepich et al. 1998; Sepich et al. 1994; Westerfield et al. 1990). The data for immobile *nic^{b107}* homozygous embryos confirm that chevrons form (Figure 4.4, orange symbols), as expected (Schröter et al. 2008; van der Meulen et al. 2005). As then expected for segments 4-13, which ceased chevron formation before the start of movements in mobile embryos, mobile and immobile embryos showed very similar timing of chevron formation, t_{start} and t_{end} .

Importantly, no significant difference was found between mobile and immobile embryos in the values of final chevron angles α_{end} , based on 8 hours of recording after movements of wildtype embryos had started. Strikingly, no significant differences were found for segments 14 and 15 which finished chevron formation after the embryo started to move. I conclude that the movements of early rhythmic muscle contraction that precede swimming have no effect on the formation of chevrons in the zebrafish embryo.

4.2.5. ROLE OF SIMPLE CHEVRON TEMPLATING

The data in table 4.1 and fig. 4.4C can also be used to test the previously proposed templating mechanism for chevron formation (van Raamsdonk et al. 1979). If the chevron shape is simply copied from a chevron-shaped surface at the back of the head, then I expect the same chevron angle for all segments, but this is not observed at any stage of chevron formation. Thus, the new data do not support the idea that templating alone is responsible for the development of the chevron shape in the anterior trunk.

4.2.6. INHIBITION OF MUSCLE PIONEER DIFFERENTIATION

The data presented above rule out the body-movement, simple-templating and notochord-movement hypotheses (see section 4.3.1). Muscle pioneer cells are thought to be responsible for chevron formation (Dolez et al. 2011; Meyers et al. 2013). Muscle

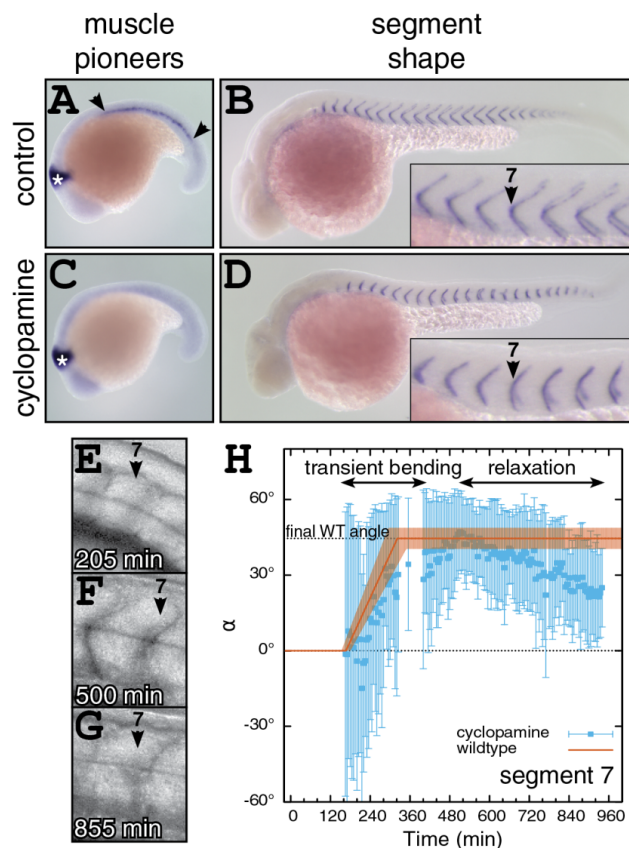


Figure 4.5.: Role of muscle pioneers in chevron maintenance, but not formation. **A, B**: embryos treated with 0.2% DMSO. **A**: *engrailed2* (*en2*) in situ hybridization of 18 somite stage. Muscle pioneers are stained by *en2*, area between arrowheads. The midbrain is marked with a white asterisk. **B**: *cb1045* in situ hybridization of 36 hours post fertilization (hpf) embryo to visualize segment boundaries. **C, D**: embryos treated with 7.5 μM cycloamine from bud stage. **C**: *en2* in situ hybridization. Muscle pioneers are absent. **D**: *cb1045* in situ hybridization of 36 hpf embryo. Boundaries are U-shaped. **E-F**: Lateral views of segment 7 of an embryo treated with 7.5 μM cycloamine from bud stage. **E**: Newly formed segment is cuboidal. **F**: 300 min after formation the segment has a clear chevron shape. **G**: At 855 min the chevron shape relaxed into a U-shape. **H**: Quantification of chevron angles of the segment shown in E-G (blue squares and error bars). The orange line shows the typical bending of an immobile embryo (empirical model for chevron angle time course with parameters for segment 7 from fig. 4.4, uncertainty depicted by the transparent orange area). Experimental methods can be found in Rost et al. (2014).^a

^aReproduced from Rost et al. 2014, Fig. 4.

pioneers can be identified by *engrailed2* expression (Figure 4.5A). Embryos treated with 0.2% DMSO carrier form normal chevrons, indistinguishable from wildtype embryos grown in only E3 medium, as illustrated by *cb1045* expression at segment boundaries (Figure 4.5B). Muscle pioneer differentiation can be blocked by inhibiting Shh signaling with cyclopamine (Barresi et al. 2001; Wolff et al. 2003) (Figure 4.5C). As expected, segment boundaries showed a U-shape phenotype at 36 hpf (Figure 4.5D), resembling U-mutants. I quantified time-lapse movies of these muscle pioneer-ablated embryos (Figures 4.5E-H, Movie 3 in supplementary material to Rost et al. (2014)). Segment formation progressed along the axis at the same rate as under normal conditions (data not shown). Surprisingly, I found 12 segments in 3 fish that transiently formed chevrons with a normal angle at around 400 min to 500 min (Figures 4.5F,H and fig. S7). Subsequently, the chevron shape was not maintained and relaxed into a U-shape (Figure 4.5D). For the majority of the analyzed segments, the wildtype start- and end-times of bending were in good agreement with the transient bending of muscle pioneer-ablated embryos (orange curve in fig. 4.5H).

4.3. DISCUSSION

4.3.1. INSUFFICIENCIES OF THREE PROPOSED MECHANISMS TO EXPLAIN CHEVRON FORMATION

The quantitative comparison of mobile and immobile embryos rules out a role for swimming motions of the embryo in both the timing and final shape of the embryonic chevrons. This corroborates and extends the earlier evidence that immobile *nic^{b107}* mutants did not show obvious chevron defects (Schröter et al. 2008; van der Meulen et al. 2005). However, this finding does not impact the acknowledged importance of the chevron shape for the locomotory function.

I quantified final chevron angles as function of segment index and found a monotonic increase for segments 4 to 7. Also, these segments also start chevron formation simultaneously, whereas segments 1 and 2 do not form chevrons (Figure 4.4). Instead of segment 3, earlier reports described this transition at segment 5 or 6 (van Raamsdonk et al. 1974a) which may reflect the lower spatial and temporal resolution of earlier methods. However, van Raamsdonk et al. (1974a) used a slightly lower temperature which might shift the transition. The increase in chevron angle along the anteroposterior axis rules out simple templating hypothesis according to which each angle is just a copy of its earlier-formed anterior neighbor. This also agrees with the results of Riedel-Kruse et al. (2007) in which correct segmentation was transiently perturbed and then rescued. Although segments 7 to 17 did not form correctly and thereby would be unable to pass on a chevron pattern, the more posterior segments were shaped as chevrons again. Windner et al. (2012) rescued defective somitogenesis in the *fss* mutant by transient expression of the Fss/Tbx6 protein. They observed one or two contiguous chevrons, for which the tissue immediately anterior was not chevron-shaped, again inconsistent

with a simple templating mechanism for chevron formation. Nevertheless, the posterior boundary of any segment is the anterior boundary for the next segment and can thereby influence its shape.

The anchoring hypothesis of Turner (2007) requires an anterior-ward movement of the notochord at the time of chevron formation. In contrast, the time-lapse movies showed a strong posterior-ward movement of the notochord relative to the segment boundaries (Movie 2 in supplementary material to Rost et al. (2014)), but this was observable only after the vacuolating cells of the notochord became visible, which occurs after completion of chevron formation. Confocal time-lapse movies revealing the posterior-ward sliding of the notochord had been reported (Barrios et al. 2003), but these were recorded slightly before chevron formation of the corresponding segments. Thus, there is no continuous anterior-ward movement of the notochord that would be consistent with the anchoring hypothesis. It remains formally possible that a wavefront of transient reversal of the direction of notochord sliding propagates along the axis in concert with chevron formation. However unlikely this proposal seems, time-lapse microscopy targeted to the notochord at this time point would be required to resolve the question.

4.3.2. U-SHAPED MYOTOME MUTANTS AND THE ROLE OF MUSCLE PIONEERS

Zebrafish mutants, termed U-mutants, have been reported in which somites form normally but the myotomes display a U-shape instead of a chevron at larval stages. These phenotypes have been associated with the failure to form a specific cell type in the myotome, the muscle pioneer at the apex of the chevron. The first genetic evidence of a role for these cells in chevron patterning came from the *no tail (ntl)* mutant, encoding a zebrafish Brachyury/T transcription factor, in which muscle pioneers fail to form and myotomes take on a U-shape (Halpern et al. 1993). Most of the U-mutants encode components of the Sonic Hedgehog signaling pathway, which is required for the differentiation of the adaxial cells, a columnar epithelium which is apposed to the notochord (Hatta et al. 1991; Weinberg et al. 1996), into early muscle fiber types such as the muscle pioneer (Johnston et al. 2011; Stickney et al. 2000). In *kny;tri* double-mutants, adaxial cells do take on a muscle fiber fate, but do not show proper spanning of the segment. Even in this case the chevron shape gets weaker (Yin and Solnica-Krezel 2007). However, the relationship between these cells and the development of the chevron has not been explored and the surgical removal of muscle pioneer precursor cells in a few segments did not result in obviously altered segment shapes (Honjo and Eisen 2005). Similarly, the inhibition of muscle pioneers by Dorsalin-1 in two consecutive segments did not lead to altered chevrons (Du et al. 1997).

The cyclopamine-treated embryos closely recapitulate the appearance of the original U-mutants; they lack muscle pioneers in early segmentation stages and they exhibit U-shaped myotomes at larval stages. However, the surprising observation of transient chevron shapes that mimic the normal untreated embryo with respect to maximum chevron angle as well as bending start- and end-time speaks against a role for muscle

pioneers in chevron formation. High-level Shh signaling induces further cell types of the sclerotome (Fan and Tessierlavigne 1994; Hammerschmidt et al. 1996), the dermomyotome (Feng et al. 2006), the spinal cord and other embryonic tissues. The cyclopamine treatment likely also affected these Shh-dependent cell types and, hence, a requirement for any of them in chevron formation is also unlikely. Conversely, the observed failure to maintain the chevron shape may be due to the perturbation of any of the Shh-dependent cell types, including muscle pioneers. My findings suggest that U-mutants may similarly exhibit a failure of chevron maintenance, not formation. A potential role for other cell-types in chevron formation remains to be investigated.

4.3.3. A MECHANICAL MODEL FOR THE SELF-ORGANIZATION OF HETEROGENEOUS CHEVRON ANGLES

The final angle of the chevron in subsequent segments increases monotonously in the anteroposterior direction until it reaches the maximum value of $(40 \pm 3)^\circ$ at segment 7, which is also reached by all posterior segments that I analyzed. Why is there such a strong segment dependence of the chevron angles across the anterior segments? Is this because there is a molecular or genetic heterogeneity along the axis? Is it necessary that the pattern is pre-programmed so that each segment's angle is individually specified by genetic means, perhaps through a Hox gene code mechanism (Prince et al. 1998), or could the collective behavior of segments with homogeneous properties self-organize the observed heterogeneous angles?

To investigate this latter possibility, I previously proposed a mechanical model that was motivated by a series of published observations about the timing of cell differentiation and its coincidence with the timing of chevron formation (Rost 2010). The expression of the muscle-specific markers Eng protein and *myod* mRNA starts simultaneously in the anterior up to seven segments in the adaxial cells. For the more posterior segments, both genes are expressed sequentially (Hatta et al. 1991; Weinberg et al. 1996). The muscle pioneers differentiate from the adaxial cells and later give rise to the myoseptum (Daggett et al. 2007; Devoto et al. 1996; Johnston et al. 2011). The cellular shape changes and cell migration that accompany the differentiation of other muscle types also start close to the notochord and simultaneously in the first five segments (Cortés et al. 2003; Daggett et al. 2007; Stickney et al. 2000; van Eeden et al. 1996; Yin and Solnica-Krezel 2007) but then proceed posteriorly with constant time lag after segment formation (Henry and Amacher 2004). In summary, these observations group the segments in the same way as my data analysis does: A group of anterior segments behaves differently than the complementary posterior segments (Figure 4.6).

Although there are currently no measurements of the forces involved, it is plausible that the reported cellular rearrangements accompanying muscle differentiation generate tension from within the segments. Those cellular rearrangements start medially close to the notochord and the tension would act only medially on the segment boundaries and thereby bend them. Reinforced by extracellular matrix, these boundaries will resist

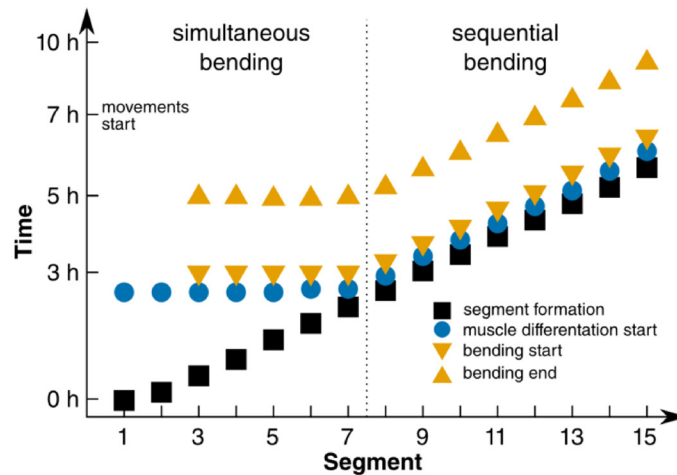


Figure 4.6.: Summary of chevron dynamics. Time of somite formation, approximate start of muscle differentiation (including cellular rearrangements and shape changes), chevron formation start and end time are sketched as function of segment index. Segments 1-7 differentiate simultaneously, i.e. anterior-most segments delay differentiation by up to 3 h after segmentation. Chevron formation of segments 1 and 2 is not detectable. Segments 4-7 deform simultaneously. Segments posterior to the 7th differentiate and deform sequentially. For any segment, chevron formation takes 2 h from onset until the final angle is reached^a.

^aReproduced from Rost et al. 2014, Fig. 5.

bending to some degree. The emergent behavior induced by the tension cannot be foreseen intuitively since all segments are coupled and interact simultaneously. It is possible to imagine all but the first segment acquiring equal shapes, or alternatively, multiple solutions may coexist and a fluctuation of a single initial segment shape could set up a pattern of mirrored chevrons to either side of the initial fluctuation.

The mathematical formalization of the model is required to understand if the system is capable of showing the emergence of the experimentally observed heterogeneous pattern (Figure 4.7). I previously derived and solved the mathematical formalization of the model (Rost 2010; Rost et al. 2014). Here, I sketch the main ideas but I omit the detailed calculations which can be found in Rost (2010) and Rost et al. (2014).

Note that this model assumes that tension is generated within the segment, but it does not attempt an explicit description of individual cellular behaviors and is agnostic about the source of this tension. The model includes the case that the reported cellular rearrangements cause the tension but it also encompasses other potential causes of tension. I reduce the model to two dimensions thanks to translational symmetry in the medio-lateral direction. It consists of $n = 7$ segments. Each segment has the same anteroposterior length L and dorso-ventral height h but a variable chevron angle $\alpha_i(t)$ of its posterior boundary. The angle of the segment's anterior boundary is given as the angle $\alpha_{i-1}(t)$ of the posterior boundary of the corresponding neighboring segment. I treat the anterior-most boundary between the head and segment 1 as stiff and straight, i.e. with a constant chevron angle of 0° . All segment boundaries are initialized as straight (Figure 4.7A). I then add harmonic springs (spring constant K_x , rest length $L_0 < L$) in each segment that model the intra-segmental tension (Figure 4.7B'). These springs contribute part of the energy of the system (Equation fig. 4.7D, blue). The resistance of the boundaries against bending is modeled by adding an energy penalty (strength K_α , Equation fig. 4.7D, orange). Of course, the extension of the springs, x_i , and the chevron angles, α_i , are constrained by the geometry of the system (Figure 4.7C'). Assuming $2L \approx h$ (true for zebrafish segments) and small α_i I express this relation in the formula for the x_i (Figure 4.7D, as derived in Rost (2010) and Rost et al. (2014)).

With the derived energy and the initial conditions for α_i and the head boundary condition, I could calculate the final chevron angles in the steady state of the model and simulate the dynamics. I derived the steady state of the model by minimizing the energy. The relevant parameters are $K = K_\alpha/(K_x L^2)$, indicating the stiffness of the boundary relative to the stiffness of the intra-segment springs and L_0/L , the rest length of the spring in the segment relative to the segment length. I found that only one unique steady state exists. Independent of the chosen parameters and the number of segments, this state possesses monotonically increasing final chevron angles. The increase in chevron angle along the anteroposterior axis in the steady state is a robust property of the model (Figure 4.7E). Importantly, the *heterogeneous* steady state pattern does not need to be pre-determined by a complicated initial state but is found to self-organize from a completely homogeneous initial state.

The model predicts that all segments would remain straight in the case of no in-

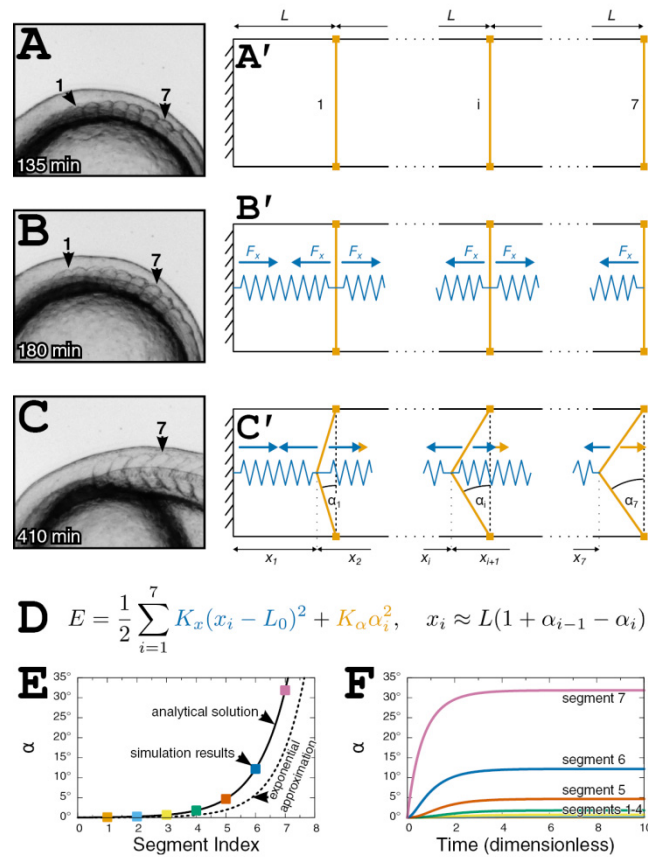


Figure 4.7.: A mechanical model for the establishment of chevron angles. **A-C**: Representative segment shapes (see fig. 4.1). **A**: The first 7 segments have formed with cuboidal shape. **B**: At about 180 min chevron formation starts, hypothetically in accordance with the onset of muscle cell differentiation and concomitant rearrangements in the medial part of the segments that result in a contractile force. **C**: At 410 min, segments 1-7 have their final shape. **A'-C'**: Construction of a minimal mechanical model for chevron shape establishment. **A'**: The model consists of 7 segments. The most anterior segment (1), one intermediate (i) and the last (7) are sketched. The boundary anterior to segment 1 is the posterior boundary of the head and treated as stiff. I neglect the lateral dimension and assume that all segments have the same anteroposterior length L and dorso-ventral height h . **B'**: To model the hypothesized intra-segmental tension I insert springs (blue) into each segment. The springs are identical (rest length L_0 , spring constant K_x). Blue arrows depict the forces exerted on the segment boundaries. *(continued on next page)^a*

^aReproduced from Rost et al. 2014, Fig. 6.

Figure 4.7.: (continued from previous page) **C'**: Except for the anterior boundary of segment 1 the segment boundaries are able to bend. The amount of bending is described by chevron angle α_j . I assume the dorsal and ventral tips of the boundaries (orange squares) to be fixed by the bulk segment tissue so that the segment length, L , cannot change and segment boundaries can only react to forces by bending. I assume the segment boundaries to resist this bending which results in forces in opposite direction (orange arrows). **D**: This simple mechanical model is fully defined by specifying the energy, E , of the system. I choose the intra-segmental springs (blue in the equation) to be harmonic and add a penalty for bending of the segment boundaries to the energy (orange in the equation). This penalty depends harmonically on α_j and is of strength K_α . The second equation gives the geometrical constraints for x_j and α_j . **E**: The final chevron angle of the model in the steady state of my model as function of segment index. Parameters are $K = 1$, $L_0 = 0.1$ and 7 segments. Black lines show the analytical solution and the exponential approximation as they were derived in Rost (2010) and Rost et al. (2014). The colored dots are simulation results for the final angle from panel F. **F**: Numerical solutions of the overdamped equations of motion (derived in section B.1, parameters as before). For the chosen parameter values, the segments simultaneously start to form chevrons at $t = 0$, the time the intrasegmental tension is switched on. Chevron angles increase monotonically for all segments. Segments reach their final chevron angle approximately at dimensionless time $t = 5$. The most anterior segment boundaries 1-3 remain straight and therefore are hard to distinguish in the plot.

tra-segmental contraction ($L_0/L = 1$) or nearly straight (chevron angle below 1°) for very stiff boundaries ($K > 60$). For stiff segment boundaries ($K \gg 1$), the monotonic angle dependency can be approximated as an exponential function of segment index. Because an exponential function starts to increase slowly, the most anterior segments appear to remain straight.

To investigate the temporal dynamics of the model, I derive the over-damped equations of motion for the chevron angles from the system's energy (see section B.1). These equations can be solved numerically. The simulations show that a simultaneous onset of chevron formation is possible (Figure 4.7F). This result is compatible with the experimental data. The particular shape of the time course depends on parameter values.

Taken together, I reached my third goal which was to test the tension-and-resistance mechanism that I proposed previously: The observed spatiotemporal pattern of chevron angles could emerge from a homogeneous tissue without the need for additional genetic or biochemical differences between the segments.

The mechanical model was motivated by stereotypical cellular rearrangements and differentiation of muscle fibers commencing around the time of chevron formation (Figure 4.6). Importantly, the model is agnostic about which cellular or sub-cellular mechanisms might be at work. Direct tests of this hypothesis should seek to alter the generation or propagation of tension through the file of segments preceding the chevron transition. One possibility would be to ablate the first somite, thereby removing the fixed end of the chain, just before the onset of chevron formation at the 7 somite stage. The proposed tension-and-resistance mechanism predicts that the angles of the forming chevrons will be altered: because segments will pull from both, anterior and posterior, sides, reversed chevron-shapes in the anterior and a central symmetrical segment are expected. From published material, a pattern with reversed chevrons was observed in frogs (Yoshigai et al. 2009). Another test might be to explant a row of somites from the embryo prior to the segment-seven transition, and ask whether a similar perturbation of chevron angles is observed as with the ablation of somite 1. If the somites could be separated from the file, or otherwise individually explanted (Beattie and Eisen 1997; Laale 1982), the autonomy of the chevron shape's development could be directly addressed. If somite 3 and somite 7, as examples, developed different chevron angles in isolation, my hypothesis of a collective mechanism would be contradicted.

If evidences supporting the general mechanical model were found, it would make sense to explore the cellular and molecular bases for this activity in some detail. Cellular candidates would include the rearrangement of the adaxial cells from epithelium to mesenchyme, or the development and migration of various muscle fiber types. Molecular candidates would include various force-generating systems such as cortical actin-myosin contractility, microtubule associated processes, or ion-flux regulated cellular volume changes.

My quantitative data analysis revealed a correlation between the reported onset of muscle differentiation and chevron formation. The mechanical model of chevron formation provides an explanation of the position-dependent final chevron angles for the anterior

segments. Please note that I was not able to obtain a quantitative fitting to the final angle of these segments. I would have been able to fit the data by introducing a non-linear saturation term in the model, but in the absence of a specific biological motivation for this term I have avoided the unnecessary complication. Furthermore, segments 8 to 32 do not deform more than segment 7 and also appear sequentially, but both of these properties are currently ignored by the simple model. To account for the constant posterior segment boundary angles, I propose a model extension with time-dependent parameters that reflect the developmental maturation of muscle differentiation.

Measurements and model are made in 2D, yet the body is 3D. A potential role for tensions in the third dimension is worth considering if such tension becomes quantitatively measurable. For future studies it is important to quantify changes of body cross section, cell rearrangements, muscle fiber elongation, muscle fiber force as function of segment index and time, and to correlate these new data sets to the space-time plot of chevron formation (Figure 4.6). Any observed correlations should then facilitate the identification of the mechanistic cause of the effective force field I have modeled. Extensions into 3D are required to address the later changes towards the concentric series of cones in the adult (Greene and Greene 1913; Shann 1914; Videler 1993).

4.3.4. CHEVRON PATTERNS IN OTHER SPECIES AND EVOLUTIONARY ASPECTS

Chevron patterns exist in other species, including other fish, frogs, salamanders, lampreys, *Amphioxus* and the pre-Cambrian fossil *Pikaia*. Key cellular events that inspired the tension-and-resistance model are conserved. For instance in *Amphioxus*, the chevron pattern forms in concert with cell elongation and muscle differentiation is delayed for anterior segments (Hatschek 1882; Hatschek 1893; Kästner 1892). In agreement with the proposed collective mode of chevron formation, several species including the tadpole of the frog *Leptodactylus albilabris* (Dent 1956), *Pikaia* (Morris and Caron 2012) and hagfish (Müller 1836) show anterior straight segments and bent posterior segments. While most authors only distinguish straight anterior versus bent posterior segments, those species might actually show a monotonic increase in chevron angle. For the tadpole of the frog *Xenopus*, published figures show monotonically increasing final chevron angles for at least 10 anterior segments (Gray et al. 2009; Lee et al. 2010). It will be interesting to quantify angle time courses in *Xenopus* and to compare these with the correspondingly parameterized model.

The chevron shape itself and the shape's function in locomotion have been used to infer the evolutionary relationships among chordates (Lacalli 2012; Mallatt and Holland 2013; Morris and Caron 2012). However, the development of the chevron, especially the mechanism underlying it, was largely ignored. The discussion of existing hypotheses and the proposed mechanism, which was motivated by quantitative correlations in fish but might be conserved across a number of other species (see above), may add to the emerging picture of chordate evolution.

4.4. CONCLUSION

I have quantified the time course of early chevron formation in terms of chevron formation start time, end time and final chevron angle for segments 1-15 for mobile, immobile and cyclopamine-treated zebrafish. To summarize the dynamic behavior of chevron formation in a compact and informative manner, I described the change in the chevron angle over time with an empirical model. The obtained data reject or heavily constrain the possible contribution of a number of hypotheses. I showed that muscle pioneers are not required for chevron formation but they or other high-level Shh signal-dependent cell types may be involved in chevron maintenance. I tested a previously proposed tension-and-resistance mechanism based on interactions between intra-segmental cell rearrangements and segment boundaries that explain the early phase of chevron development. A simple mechanical model allowed me to verify that this mechanism could account for the observed spatiotemporal pattern. A strong aspect of the model is the minimal set of ingredients it depends on and yet its robust prediction of the observable monotonic increase in final chevron angles along the anteroposterior axis. An appropriate temporal order of muscle cell differentiation (Figure 4.6) with uniform properties for all segments appears sufficient for the chevron pattern and its spatial dependencies to self-organize according to physical laws. Hence, evolution of segment-specific properties such as the increasing chevron angles across the anterior segments would not be necessary.

5. NEUROGENESIS IN THE ADULT HUMAN BRAIN

5.1. INTRODUCTION

For a long time, it was commonly assumed that there is no neurogenesis in the adult human brain. Evidence for this view came from studies on primates, which failed to reveal neurogenesis in adult primate brains (Eckenhoff and Rakic 1988; Rakic 1985). However, a later study based on the incorporation of BrdU in the adult human hippocampus showed the existence of neurogenesis in the adult human brain (Eriksson et al. 1998). Nonetheless, the amount of neuron turnover in the adult human brain remained an open question of. The answer to this question is relevant to understand whether neuron turnover is of importance for the function of the human brain as it is known to be for rodents (Clelland et al. 2009; Nakashiba et al. 2012; Sahay et al. 2011). The outstanding work by Spalding et al. (2013) approached this question by combining quantitative data and mathematical modeling and found that about 1/3 of the neurons in the human adult hippocampus undergo turnover and that about 700 neurons are born every day. In this chapter, I will reanalyze their data using their deterministic neuron turnover model. Spalding et al. (2013) used the method of LS to estimate the turnover parameters. Instead, I will make use of the more general ML method to perform the statistical inference. This way, I do not rely on possibly unjustified assumptions that Spalding et al. (2013) had to make.

Spalding et al. (2013) exploited the increase in the atmospheric concentration of the carbon isotope ^{14}C due to above-ground thermonuclear bomb tests during the cold war (Figure 5.1). This ^{14}C forms carbon dioxide (CO_2) in the atmosphere which is taken up by plants and finally by humans via the food chain. When cells synthesize new DNA for mitosis the current ^{14}C concentration creates a date mark in this DNA (Spalding et al. 2005). This allows inferring neuron turnover using the following idea: If all neurons were born during early development, the neuron genomic DNA would have the age of the subject. Hence, the ^{14}C concentration in the neuron genomic DNA would correspond to

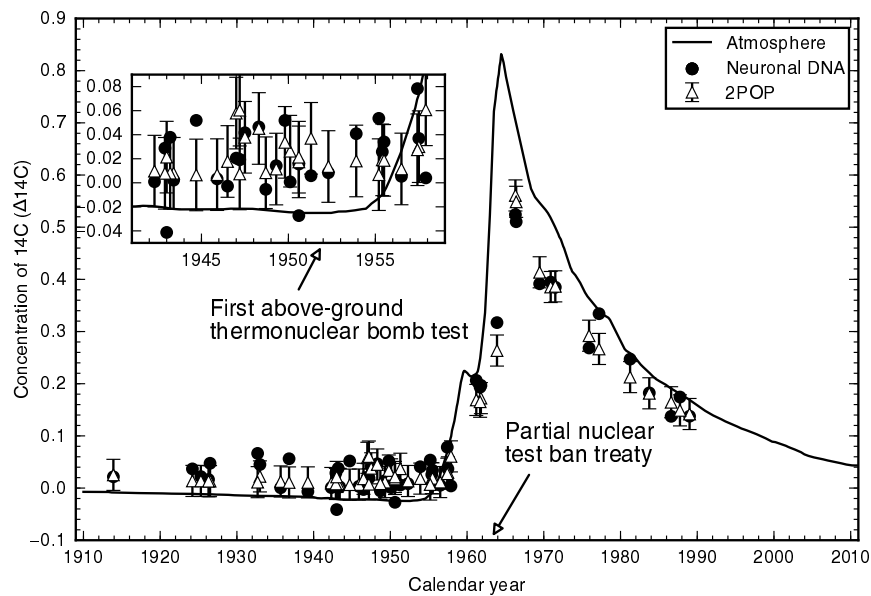


Figure 5.1.: Concentration of the carbon isotope ^{14}C in the atmosphere and hippocampal neuron genomic DNA in units of $\Delta^{14}\text{C}$. The black line shows the time course of atmospheric ^{14}C concentration in the last century with a peak stemming from above-ground thermonuclear tests that were performed from 1953 until 1963 (Nydal and Lövseth 1965; Vries 1958). The black circles show ^{14}C of hippocampal neuron genomic DNA plotted at the date of birth of subjects. The white triangles show the model prediction of scenario 2POP using the new parameters from my ML estimation (Tables 5.1 and 5.2 and fig. 5.2). Error bars depict the measurement error, σ . Inset is a zoom on the time between 1940 and 1960.

the atmospheric ^{14}C concentration at the date of birth. On the other hand, if all neurons would be turned over at a very high rate, the neuron genomic DNA would be very young. Consequently, the ^{14}C concentration in the neuron genomic DNA would correspond to the atmospheric ^{14}C concentration at the date of death. If the subjects' ^{14}C concentration in the neuron genomic DNA corresponds neither to the atmospheric ^{14}C concentration at birth nor at death, neurons are turned over at an intermediate rate.

Spalding et al. (2013) could measure the mean concentration of ^{14}C in the DNA of hippocampus tissue samples postmortem in subjects ($n = 55$) of different age using mass spectroscopy. As expected for an intermediate turnover rate, the ^{14}C concentration in the neuron genomic DNA corresponded neither to the atmospheric ^{14}C concentration at birth nor at death. To estimate the turnover rate, Spalding et al. (2013) developed a mathematical model of neuron turnover. The model predicts the ^{14}C concentration in neuron genomic DNA based on the known dynamics of ^{14}C concentration in the

atmosphere and the unknown turnover parameters (Bernard et al. 2010). Spalding et al. (2013) tested several model versions, termed scenarios. In each scenario the neuron turnover is modeled differently. While the authors also investigated many complex scenarios, I concentrate on only two scenarios: In the simplest scenario, termed scenario A, all neurons are turned over at a constant rate, r , throughout life. The other scenario is termed 2POP. It was identified by Spalding et al. (2013) as the best fitting scenario. In this scenario, only a fraction, f , of the neuron population undergoes turnover at constant rate, r . The model equations that I used for my analysis are given in the appendix, section B.2.

Spalding et al. (2013) estimated parameters with the method of weighted LS. To estimate the parameter uncertainties, they calculated the CIs by exploring the SSE landscape with MCMC methods. They selected the best scenario with a particular form of the AIC. There are two potential problems with this approach: First, the choice of the weighted LS method inherently implies a choice of the error model (Burnham and Anderson 2002; Hilborn and Mangel 1997; Olive et al. 2014). In particular, the arbitrary choice of the weights implicitly leads to a possibly unjustified assumption for the magnitude of the measurement error. However, the error model is crucial to correctly calculate the CIs and for model selection (Kreutz et al. 2007). Second, the different and more commonly used form of the AIC, namely the AICc (Equation (2.7)) may select a different scenario.

To circumvent the potential problems of the method of weighted LS, I estimate the parameters for the scenarios A and 2POP using the more general ML method and I select the best fitting model with the AICc. I find a general agreement with the parameter estimates reported by Spalding et al. (2013) and identify the same best fitting scenario. However, I can determine the fraction of renewing cells with higher precision. Strikingly, I find that for the turnover rate only a lower limit can be inferred. Hence, the neuronal turnover might occur at even higher rates than reported previously. Furthermore, I estimate how many additional samples would be needed to estimate the turnover rate with high precision. I find that collecting data from as many as 100 subjects that died recently does not guarantee substantial increase in precision. Instead, collecting data from as few as 5 subjects that died between 1960 and 1970 would increase precision considerably.

5.2. RESULTS

5.2.1. MAXIMUM-LIKELIHOOD ESTIMATION OF CELL TURNOVER PARAMETERS

I used the software Engauge Digitizer 5.2¹ to extract the atmospheric ¹⁴C data from Spalding et al. (2013, Fig. 2A). Furthermore, I made use of the ¹⁴C data that is provided as a supplement to Spalding et al. (2013) (Figure 5.1). I numerically solved the neuron

¹<https://markummittchell.github.io/engauge-digitizer/>

Parameters Unit	Turnover rate, r (per year)	Measurement error, σ ($\Delta^{14}\text{C}$)
Values LS	0.0066	1000‰/500‰
95% CI	-	-
Values ML	0.0055	54‰
95% CI	[0.0041, 0.0071]	[46‰, 66‰]

Table 5.1.: Comparison of parameter estimates for the LS and ML methods for scenario A. The values for the LS method are taken from Spalding et al. (2013, Table S3). In this case, the measurement error is not fitted but chosen by the authors in the model as weights, w_i (see section 5.3). The parameter values for the ML method were calculated as described in this chapter.

turnover model by Spalding et al. (2013) (see eqs. (B.6) to (B.10)) with Python code.²

As stated above, the use of the method of weighted LS by Spalding et al. (2013) implied a possibly unjustified choice of the measurement error. To overcome this potential problem, I used the ML method to estimate the parameters. Therefore, I use an error model of constant additive, normally-distributed noise with unknown measurement error, σ , assuming that the measurement error is the same for all subjects. This allows me to treat the measurement error, σ , as one additional unknown parameter which I can fit to the data. The corresponding Log-Likelihood is given by inserting the ^{14}C prediction of the neuron turnover model (see eq. (B.8) in section B.2), in eq. (2.3):

$$\ln \mathcal{L}(r, f, \sigma) = -\frac{1}{2} \sum_{i=1}^n \left(\frac{\tilde{C}(t_{b,i}, t_{d,i}; r, f) - C_i}{\sigma} \right)^2 + n \ln \left(\frac{1}{\sqrt{2\pi}\sigma} \right), \quad (5.1)$$

where \mathcal{L} is the likelihood, $\tilde{C}(t_{b,i}, t_{d,i}; r, f)$ is the predicted ^{14}C concentration for a subject i that was born at $t_{b,i}$ and died at $t_{d,i}$, C_i is the measured ^{14}C concentration of subject i and n is the number of subjects in the dataset. Then, the values for the turnover rate, r , the fraction renewing, f and the measurement error, σ , that maximize the Log-Likelihood, $\ln \mathcal{L}$, are the most likely parameters. I performed the search for these parameters as described in section 2.2. The estimated parameter values are given in tables 5.1 and 5.2 and fig. 5.2. I estimated the CIs with the profile likelihood method (see section 2.1.2).

For scenario A, the turnover rate estimated with the LS method lies within the 95% CI of the ML method (Figure 5.2, left panel). Hence, both parameter estimation methods agree.

For scenario 2POP the fraction renewing estimated with the LS method also lies within the 95% CI of the ML method (Figure 5.2, right panel). However, the 95% CI reported by Spalding et al. (2013) is 7 times bigger than that estimated with the ML method. Compared to the ML-derived 95% CI, the LS method slightly underestimates the turnover

²The code is available on GitHub under <https://github.com/fabianrost84/C14>

Parameters Unit	Fraction renewing, f	Turnover rate, r (per year)	Measurement error, σ ($\Delta^{14}\text{C}$)
Values LS	0.35	0.12	1000‰/500‰
95% CI	[0.12 - 0.63]	-	
Values ML	0.34	0.23	30‰
95% CI	[0.31, 0.38]	[0.14, \sim 4]	[25‰, 36‰]

Table 5.2.: Comparison of parameter estimates for the LS and ML methods for scenario 2POP. The values for the LS method are taken from Spalding et al. (2013, Table S3). In this case, the measurement error is not fitted but chosen by the authors in the model as weights, w_i (see section 5.3). The parameter values for the ML method were calculated as described in this chapter.

rate in scenario 2POP (Figure 5.2, middle panel). Moreover, the ML-derived 95% CI for the turnover rate in scenario 2POP is markedly asymmetric and has a very high upper limit (Tables 5.1 and 5.2 and fig. 5.3). This insensitivity can be understood intuitively in the following way: A turnover rate of 1 year^{-1} means that the number of cells that are replaced in one year equals the number of cells in the renewing population, i.e. almost all cells in the renewing population are replaced. Therefore, the genomic ^{14}C concentration in this population will be almost equal to the atmospheric ^{14}C concentration of this year. If the turnover rate is increased even more, the resulting ^{14}C concentration can only become slightly closer to the atmospheric ^{14}C concentration. Hence, at some point, increasing the turnover rate parameter has nearly no effect on the model prediction and the model becomes insensitive to this parameter.

In agreement with Spalding et al. (2013), the best fitting scenario clearly is the scenario 2POP (evidence ratio $7 \cdot 10^3$, table 5.3, fig. 5.1).

Scenario	$\ln \mathcal{L}$	k	AICc
A	82.2	2	-160.1
2POP	155.2	3	-224.0

Table 5.3.: Comparison of the model scenarios for ^{14}C incorporation. For the scenarios A and 2POP, the maximum value of the log-likelihood, $\ln \mathcal{L}$, the number of parameters, k , and the AICc are shown. The sample size is $n = 55$ for both scenarios. Scenario 2POP is the best fitting scenario because it has the lower AICc.

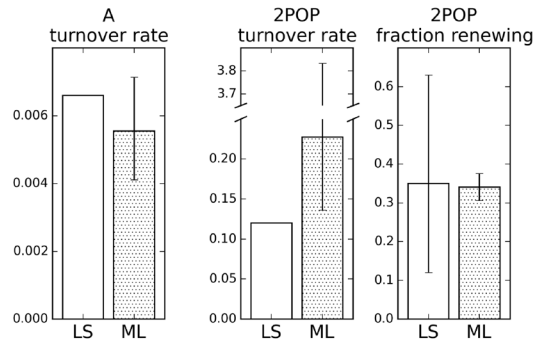


Figure 5.2.: Comparison of parameter estimates for the LS and ML methods, for the turnover rate, r , in scenario A (left panel), the turnover rate, r , in scenario 2POP (middle panel) and the fraction renewing, f , in scenario 2POP (right panel). Error bars depict the 95% CI as reported by Spalding et al. (2013) or calculated as described in this chapter for the LS and the ML method, respectively. For the turnover rates the 95% CIs were not reported by Spalding et al. (2013).

5.2.2. ESTIMATION OF ADDITIONAL NUMBER OF SUBJECTS NEEDED TO INFER TURNOVER RATE

Above I showed that only a lower limit for the turnover rate, r , could be inferred for scenario 2POP. One might expect, that the turnover rate can be estimated more accurately if one acquires data from more subjects. To investigate this quantitatively and to estimate the number of additional subjects needed, I will simulate data of artificial subjects. Then, I can repeat the parameter estimation using the real data plus the data of artificial subjects. If the resulting CI are substantially smaller, this indicates that the turnover rate could be estimated more accurately by increasing the sample size.

Some subjects will not contribute much information on the turnover rate. For example, a subject that was born and that died before the first thermonuclear bomb test will show the same ^{14}C concentration in the neuron genomic DNA independent of the turnover rate. The reason is that it experienced a nearly constant ^{14}C concentration throughout life (Figure 5.1). Hence, neuron turnover would not have changed the ^{14}C concentration in the neuron genomic DNA.

To quantitatively assess which subjects could contribute much information on the turnover rate, I calculated the sensitivity of the ^{14}C concentration on the turnover rate. In other words, I wanted to find out how much a change in the turnover rate, r , would change the ^{14}C concentration in the neuron genomic DNA. Therefore, I assume that scenario 2POP is the true scenario and that the fraction renewing, f , I estimated with the ML method is true (Table 5.2). Then, I calculate the difference in ^{14}C concentration, $diff$, between predictions of the scenario 2POP using a high and a low turnover rate,

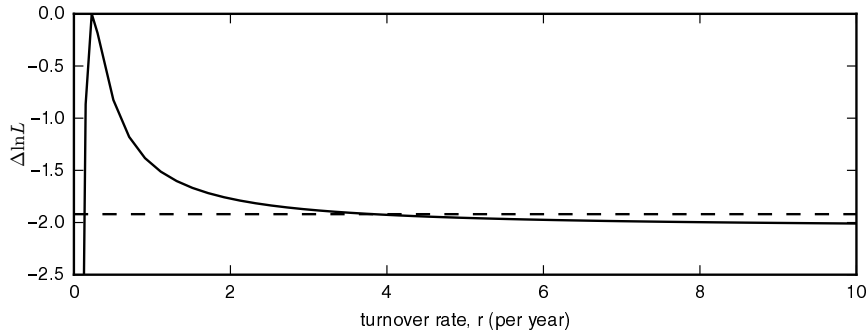


Figure 5.3.: Log-likelihood profile for the turnover rate, r , in scenario 2POP. The turnover rate was varied from 0 year^{-1} to 10 year^{-1} . For each fixed value of the turnover rate, r , in this interval the fraction renewing, f , and σ were fitted. The difference of the corresponding log-likelihoods to the maximal log-likelihood is shown. The maximum gives the optimal parameter ($r = 0.23 \text{ year}^{-1}$). The values of r where the profile crosses -1.92 (dashed line) give the 95% CI (see section 2.1.2).

r_{high} and r_{low} , respectively:

$$diff = \tilde{C}(t_b, t_d; r_{high}, f) - \tilde{C}(t_b, t_d; r_{low}, f), \quad (5.2)$$

where I arbitrarily chose to set $r_{high} = 3.83$ and $r_{low} = 0.23$ to the limits of the 95% CI (Table 5.2). Interestingly, for all subjects that died after 1990 the predicted difference in ^{14}C concentration is smaller than the estimated measurement error of 30‰ (Figure 5.4A). As all subjects used by Spalding et al. (2013) died after 1990, this can be viewed as an alternative explanation for the insensitivity in the estimation of the turnover rate, r (Figure 5.3).

On the contrary, for subjects that died between 1960 and 1970, i.e. in the period of strong increase in atmospheric ^{14}C concentration (Figure 5.1), a much higher difference is predicted (light area around yellow band in Figure 5.4A). I reasoned that if only a few samples from such subjects would be available this might allow inferring the turnover rate with higher precision. However, it might be impossible to get samples from subjects that died in the 1960s. Hence, I also wanted to test whether adding very many samples from subjects that died recently might also increase the precision in the turnover rate.

To perform these tests and to assess the number of additionally needed subjects, I decided for the following strategy: I assume that scenario 2POP with the parameters given in table 5.2 is true. Then, I simulate predicted ^{14}C concentrations for a number of artificial subjects. I add this simulated data to the experimental data by Spalding et al. (2013). Next, without using my knowledge of the parameter values I used for the simulation, I repeat the parameter estimation method described above. I calculate the log-likelihood profile for the turnover rate, r , to test whether it could be determined with higher precision using the larger, artificial dataset. I created artificial subject datasets

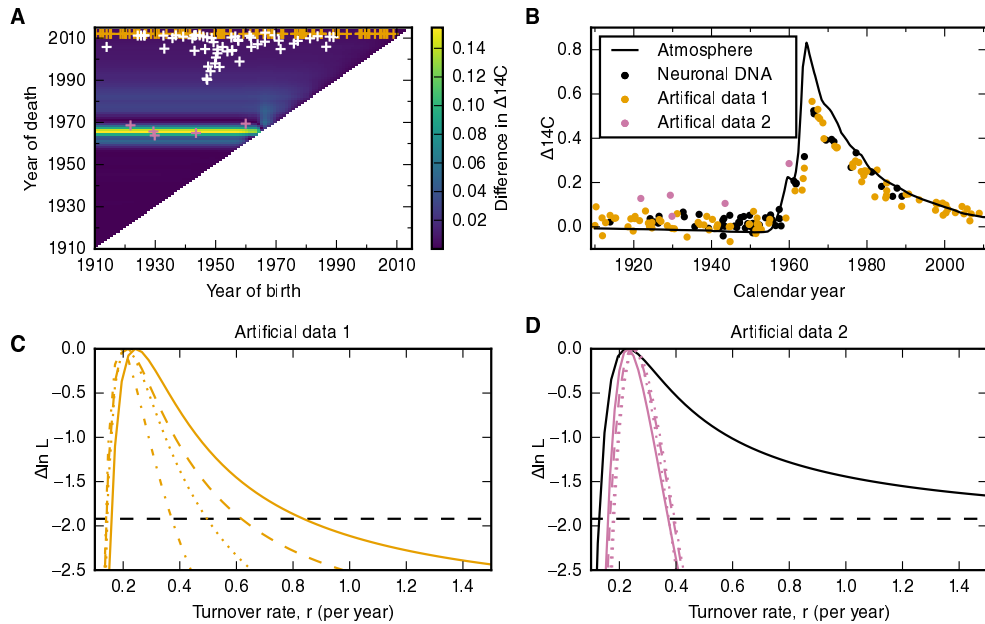


Figure 5.4.: Estimation of additional number of subjects needed to infer turnover rate. **A:** Scenario 2POP will predict different ^{14}C concentrations depending on the turnover rate, r . The heat map shows the difference in ^{14}C concentration between the predictions for $r = 0.23$ and $r = 3.83$ (Equation (5.2)). The fraction renewing, f , and the error model variance are set as given in table 5.2. White crosses: Subjects used by Spalding et al. (2013), orange crosses and purple crosses show a realization of type 1 and type 2 artificial subjects, respectively. **B:** Similar plot as fig. 5.1 with the two realizations of artificial subject datasets added. **C:** Similar plot as fig. 5.3. For the calculation of the solid log-likelihood profile the artificial data 1 was added to the data by Spalding et al. (2013). The other log-likelihood profiles were calculated using other realizations of artificial subjects created as artificial data 1. **D:** Same as (C) but artificial data 2 was used.

of 2 types, namely type 1 datasets of subjects that died recently and type 2 datasets of subjects that died in the 1960s. In type 1 datasets, 100 subjects are randomly born between 1910 and 2010 and die in 2012. In type 2 datasets, 5 subjects are randomly born between 1910 and 1960 and die randomly between 1961 and 1970. A realization of each type of artificial data is shown in figs. 5.4A,B. I calculated the log-likelihood profile for multiple realizations of artificial data of type 1 (Figure 5.4C). Interestingly, many of the profiles show that the turnover rate could not be determined with high precision despite the huge amount of added samples. On the contrary, for artificial data of type 2, all realizations allowed a much preciser estimate of the turnover rate with only 5 additional samples added (Figure 5.4D).

5.3. DISCUSSION

Spalding et al. (2013) fitted each scenario with the weighted LS method, i.e. by minimizing the SSE:

$$SSE = \sum_{i=1}^n (\tilde{C}(t_{b,i}, t_{d,i}; r, f) - C_i)^2 w_i^2, \quad (5.3)$$

where C_i is the measured ^{14}C concentration in subject i which was born at $t_{b,i}$ and died at $t_{d,i}$ and w_i is a weight. Depending on the mass of carbon extracted from a subject they chose a weight of 1 per $\Delta^{14}\text{C}$ (below 10 μg) or 2 per $\Delta^{14}\text{C}$ (above 10 μg) to reflect different measurement errors of the mass spectroscopy. Setting these weights to 1 and 2 arbitrarily, has consequences for the final result: To calculate CIs for the parameters, the LS method can be interpreted as a special case of the more general ML method, where one assumes an additive, normally-distributed noise error model (Burnham and Anderson 2002; Hilborn and Mangel 1997; Olive et al. 2014). Importantly, for the CIs and the AIC to be correct, the weights, w_i , in eq. (5.3) have to be the inverse of the measurement error, σ (Burnham and Anderson 2002; Olive et al. 2014).

Here, I used the data and the mathematical models from Spalding et al. (2013), but I used the more general ML method instead of the LS method to infer cell turnover dynamics (Burnham and Anderson 2002). I also assumed an additive, normally-distributed noise model, which is a common assumption for biological systems (Hilborn and Mangel 1997; Kreutz et al. 2007). Please note that the source of this noise must not only be expected to be measurement errors in mass spectroscopy. Two subjects which were born and died at the same dates will show different ^{14}C concentrations due to different individual histories of the subjects, e.g. contact with radioactivity or eating habits. As the individual histories of subjects are not explicitly modeled, they have to be taken into account as a source of measurement error as well.

In both scenarios, the best fit values for turnover rate and fraction renewing are close for the LS and the ML method and mostly agree within the 95% CI. However, for the turnover rate in scenario 2POP the upper limit of the ML 95% CI is found to be very high (Tables 5.1 and 5.2 and figs. 5.2 and 5.3). This points out that with the current data it is

only sensible to give a lower limit for the amount of neuron turnover in the adult human hippocampus. Hence, the turnover rate might be even higher than reported by Spalding et al. (2013). On the contrary, the LS method shows a much larger CI for the fraction renewing than does the ML method. The LS method might overestimate the size of the CI as mathematically discussed below.

The weighted LS method can be interpreted as a special case of the ML method. This can be seen in the following way: If one assumes one would know the measurement errors, σ_i , in eq. (5.1), then the second term on the right hand side would be a constant and maximizing the likelihood would be the same as minimizing the term

$$\sum_{i=1}^n \left(\frac{\tilde{C}_i(t_{b,i}, t_{d,i}; r, f) - C_i}{\sigma_i} \right)^2. \quad (5.4)$$

If one substitutes

$$w_i = \frac{1}{\sigma_i} \quad (5.5)$$

one gets eq. (5.3) for the SSE. Hence the turnover rate, r , and the fraction renewing, f , that minimize the SSE in eq. (5.3) are the same that maximize a likelihood with known normally distributed noise, σ_i , if one substitutes the weights accordingly. One can use relation (5.5) to transform the weights used by Spalding et al. (2013) in the LS method to an assumed measurement error. Hence, the measurement error, σ , which is free and fitted in the case of the ML method, is fixed to a particular value in the LS method: A weight of 2 corresponds to $\sigma = 1/w_i = 500\%$. This is one order of magnitude higher than the result from the ML method and is clearly outside the 95% CI for the measurement error, σ (Tables 5.1 and 5.2). Furthermore, as the concentration of atmospheric ^{14}C ranges from approximately 0‰ to 800‰, noise in the order of $\sigma = 500\%$ appears unrealistically high. If the measurement errors, σ_i , are assumed too high (and hence the weights, w_i , are assumed too low), the calculated CIs will be too large. This might explain the larger 95% CI of the fraction renewing from the LS method (Table 5.2 and fig. 5.2). Hence, using the ML method, I achieved higher precision for the estimate of the fraction renewing by also using implicit information on the true noise level that is hidden in the same data.

On the contrary, I could only determine a lower limit for the neuronal turnover rate for scenario 2POP. Therefore, I estimated the additional number of subjects needed to increase the precision in this estimate. I showed that this number highly depends on when the subjects were born and when they died: Adding 100 subjects that died recently does not guarantee an increase in precision (Figure 5.4C). On the contrary, as little as 5 subjects that died between 1961 and 1970 would lead to a huge increase in precision (Figure 5.4D). However, whether samples from subjects that died more than 40 years ago are still available, I cannot judge.

Spalding et al. (2013) reported the mass spectroscopy measurement errors to be different for samples from different subjects. They defined small and large samples as

those where the extracted mass of carbon was smaller or larger as 10 μg , respectively. The authors reported the measurement errors of the mass spectroscopy to be $\pm 4\%$ and $\pm 12\%$ for large and small samples, respectively. Accordingly, they also used different weights for large and small samples. In contrast, I used the same measurement error, σ , for all samples, independent of the amount of carbon. I could have introduced and fitted two different measurement errors, σ_{small} and σ_{large} , for small and large samples, respectively. However, using the ML method I fitted $\sigma = 30\%$ for scenario 2POP (Tables 5.1 and 5.2) which is nearly 3 times as big as the measurement error for small samples. This can be explained, because, as noted previously, the measurement error, σ , must not only include the mass spectroscopy measurement errors but also reflect errors due to different individual histories of the subjects. As the fitted measurement error of $\sigma = 30\%$ is considerably higher than the mass spectroscopy error of $\pm 4\%$ to $\pm 12\%$, it appears unnecessary to weight small and large samples differently. Nevertheless, I also fitted the data using an error model with two different measurement errors, σ_{small} and σ_{large} for small and large samples, respectively.³ As expected, the measurement errors, σ_{small} and σ_{large} , were not significantly different. Hence, the mass spectroscopy measurement errors are of minor importance compared to other error sources.

5.4. CONCLUSION

In this chapter, I reanalyzed data by Spalding et al. (2013) of the ^{14}C concentration in the neuron genomic DNA of the adult human hippocampus. I used a mathematical model of neuron turnover that was also developed by the same authors. This model can be used to predict the ^{14}C concentration. Contrary to Spalding et al. (2013), I used the more general ML method and the AICc to perform the statistical inference. The ML method allowed me to relax possibly unjustified assumptions by Spalding et al. (2013) through using a more general error model.

Corroborating the previous results, I found that the model scenario 2POP, in which a subpopulation of neurons undergoes constant turnover, is the best fitting model. I could determine the fraction of renewing cells with higher precision. On the other hand, I could show that the data do not allow to estimate an upper limit for the turnover rate. This result implies that the number of generated neurons during adulthood might be even higher than reported previously. I could show that adding data from only a few subjects that died in the 1960s would increase the precision of the turnover rate estimation substantially.

Spalding et al. (2013) investigated more model scenarios than the two scenarios I chose to investigate here. In the future the other scenarios should also be investigated, to test whether scenario 2POP really is the best fitting scenario. Furthermore, approaches based on measuring and modeling the ^{14}C concentration have been applied to other tissues as well (Arner et al. 2010; Bergmann et al. 2009; Bergmann et al. 2012; Bhardwaj

³data not shown, available in the GitHub repository <https://github.com/fabianrost84/C14>

et al. 2006; Ernst et al. 2014; Spalding et al. 2008). Similar to the results presented here, future studies involving the ^{14}C incorporation approach, could make use of the ML method to perform the statistical inference.

6. SUMMARY AND OUTLOOK

The aim of this thesis was to study how cell behaviors shape selected tissues and let them grow during regeneration and development. This included the quantitative measurement and description of cell behaviors, tissue shape and size changes, as well as finding the mechanistic connection between cell behaviors, tissue shaping and growth in terms of mathematical models. In particular, within chapters 3 to 5, I studied the regeneration of axolotl spinal cord and muscle segments during tail regeneration, the shape changes of muscle segments during zebrafish development, and neurogenesis in the adult human brain.

In chapter 3 on axolotl tail regeneration, I quantified cell behaviors and tissue growth, and developed a mechanistic model of how neural stem cell behaviors produce the spinal cord outgrowth. In particular, I showed that while cell influx and neural stem cell activation play a minor role, the proliferation in a zone that initially extends 800 μm anterior to the amputation plane is the major driver of the regenerative spinal cord outgrowth. Furthermore, I presented evidence that a similarly sized zone of mesenchymal progenitors gives rise to the adjacent regenerating muscle segments.

In chapter 4, I quantified the shaping of muscle segments during development in zebrafish. Motivated by previously reported cellular behaviors happening simultaneously in the anterior segments, I had proposed the existence of a simple force-field that shapes the muscle segments. I tested the plausibility of this hypothesis with a mechanical model that correctly predicts the quantified segment shapes.

Chapter 5 was again concerned with the behavior of neural stem cells. There, I refined the estimation of neuron turnover rates in a part of the adult human brain, the hippocampus. My results mainly corroborated previous results, but I found that the rate of neuron turnover in the adult human brain might be even higher than currently believed.

To achieve these results, I used quantitative data generated by image analysis, data-driven mathematical models and statistical inference as the main tools. This demonstrated the possibility to use mathematical models for a variety of purposes in development and regeneration. These purposes include:

First, if it is not possible to measure interesting parameters directly, mathematical

models enable the use of indirect experiments to estimate the parameters. Examples include the estimation of cell cycle parameters from continuous BrdU labeling data as seen in sections 3.2.4 and 3.3.1 as well as the estimation of neuron turnover from genomic ^{14}C concentrations in section 5.2.1.

Second, purely empirical mathematical models can be used to summarize datasets by using only a few meaningful parameters. For instance, proliferation-related cell number measurements in the axolotl spinal cord could be summarized using only a few parameters that describe two spatial zones of proliferation (Section 3.2.4 and fig. 3.10). Furthermore, an empirical model for the shaping of muscle segments during zebrafish development allowed a short and summarized characterization of these shape changes (Section 4.2.2 and fig. 4.6).

Third, mathematical models that formalize a mechanistic hypothesis can be used to test the hypothesis on quantitative data. For example, in section 3.2.5, a mechanistic outgrowth model verified that the quantified cellular behaviors are sufficient to generate the observed spinal cord outgrowth. In section 4.3.3, I used a mechanical model to verify that the observed spatiotemporal pattern of muscle segment shapes could be generated by a simple mechanical force field.

Fourth, model predictions can help for experimental planning. This is exemplified by the model-driven data analysis of spinal cord outgrowth in section 3.2.2 which predicted an acceleration of the cell cycle. A detailed analysis of cell behaviors in section 3.2.4 verified this prediction. In section 5.2.2, I simulated and analyzed artificial data to predict the minimal number of additional human samples needed for an improved estimation of cell turnover parameters.

Common to all of these uses of mathematical models is that the models are designed to understand the data: they are data-driven models. The comparison of data and model was performed by statistical inference. Statistical inference requires us to model not only the biological process but also the experiment, including to model the measurement error. In chapter 5, I used published quantitative data and a mathematical model of the underlying process and changed only the error model. This led to different results. This highlights that we need to be very explicit and thoughtful about the statistical methods we use when performing mathematical modeling of quantitative data in development and regeneration. This remains an ongoing task for mathematical biologists.

In this sense also the models used in this thesis should be developed further. In sections 3.2.4 and 3.3.1, I used a model for continuous BrdU labeling to estimate cell cycle parameters. I assumed a normally distributed measurement error. But the distribution of this measurement error should be modeled explicitly, taking into account noisy cell cycle parameters and limited sample sizes. With such a model, one might deduce not only the mean cell cycle parameters, but also their distribution across the population. In practical experimental terms, a more explicit error model might also allow using less data while achieving the same accuracy of estimates. The development of such a model is a task for the future.

When Erwin Schrödinger investigated the question “What is life?” in 1943, he hardly

used mathematics as “the subject was [...] too involved to be fully accessible to mathematics” (Schrödinger 2008, p. 3). The questions tackled in this thesis treated only one small aspect of life: Regeneration and development in terms of the underlying cell behaviors. For this aspect, I used mathematics to gain new insights, making use of the detailed data available nowadays. This might be a small step on the way to a quantitative, mechanistic understanding of how cells behave to shape tissues and let them grow.

A. SUPPLEMENTARY FIGURES

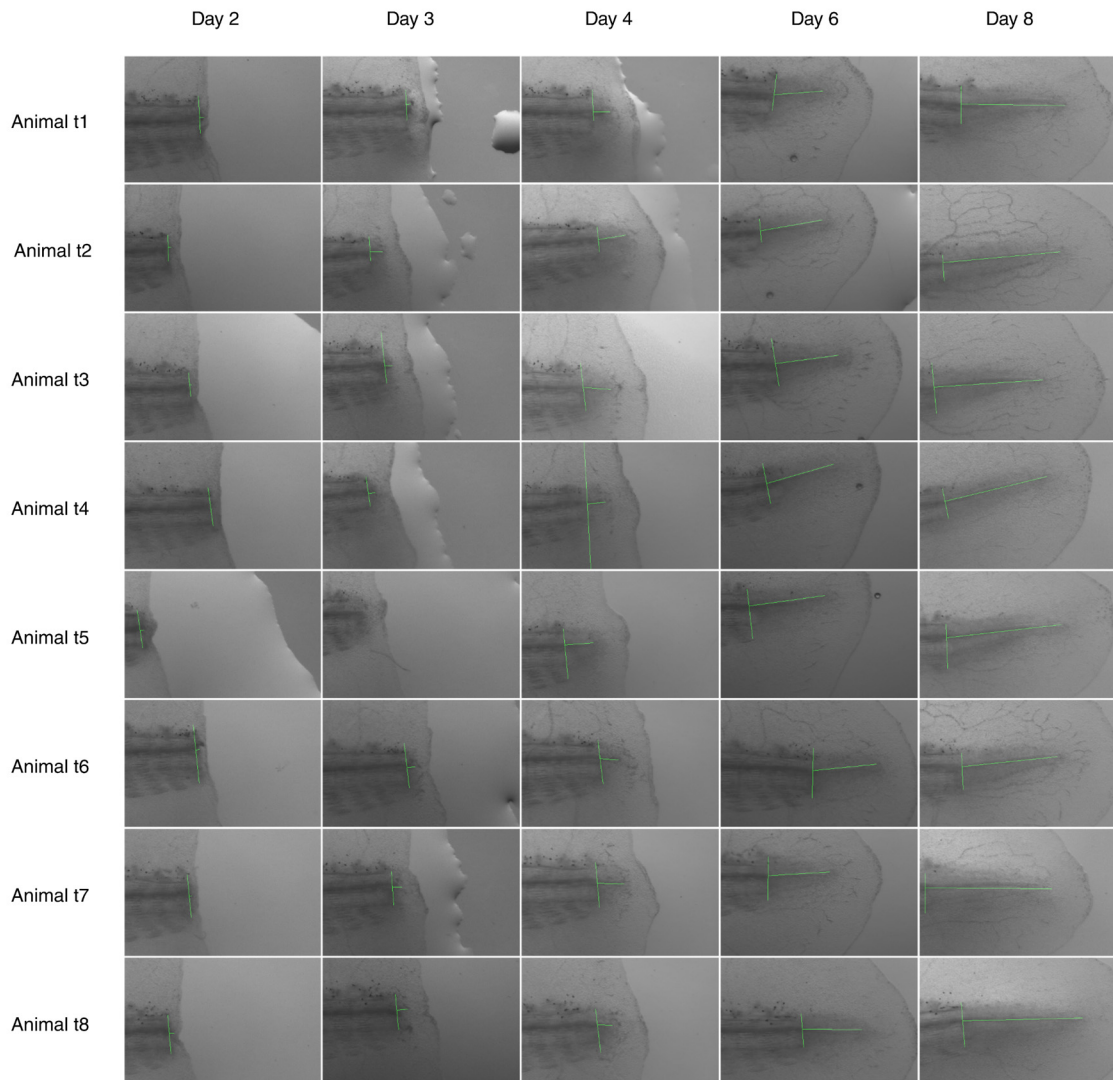


Figure S1.: Images used for spinal cord outgrowth measurements in fig. 3.4B. Each row shows an axolotl; columns are the different time-points analyzed. Thin green vertical and horizontal lines mark the amputation plane and the spinal cord outgrowth, respectively. High-resolution images can be found in Rost et al. (2016b). Animal t3 is shown as representative images in fig. 3.4A.

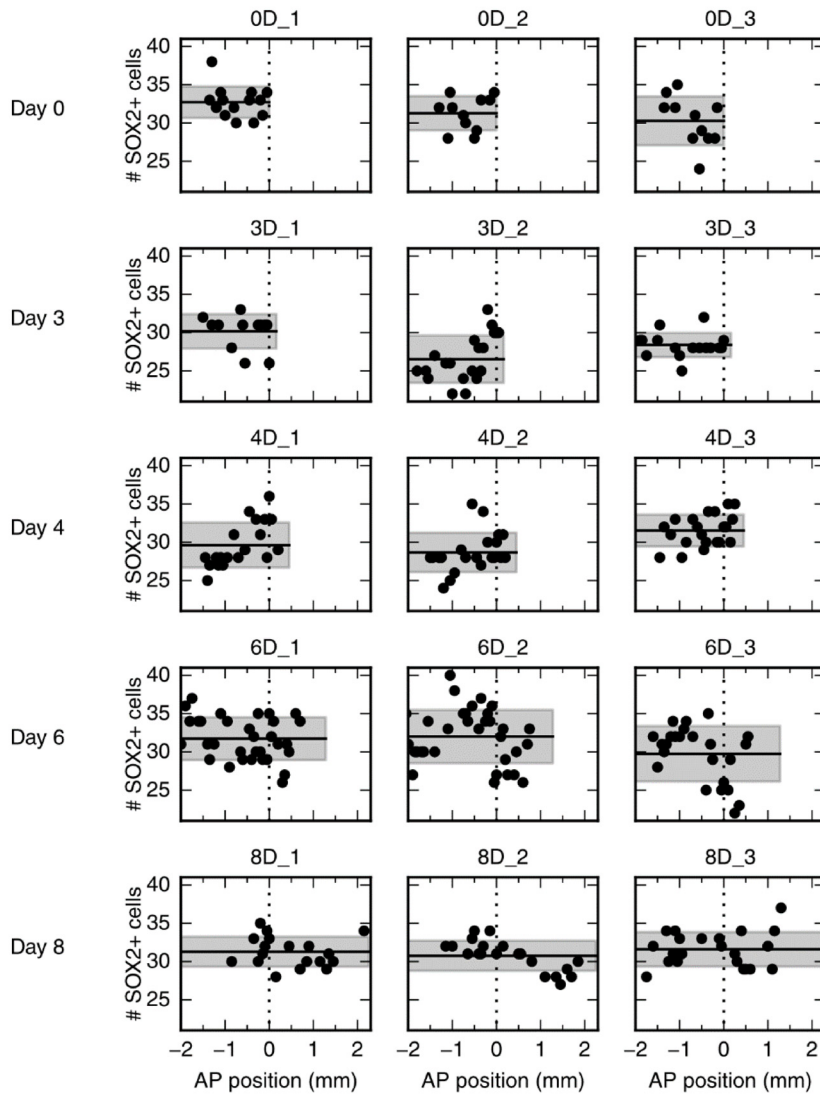


Figure S2.: Number of stem cells per cross section along the AP axis for all 15 animals. Each row shows 3 animals at a time point. Data from animals 0D_1 and 4D_3 are shown as representative data in fig. 3.9A and A', respectively.

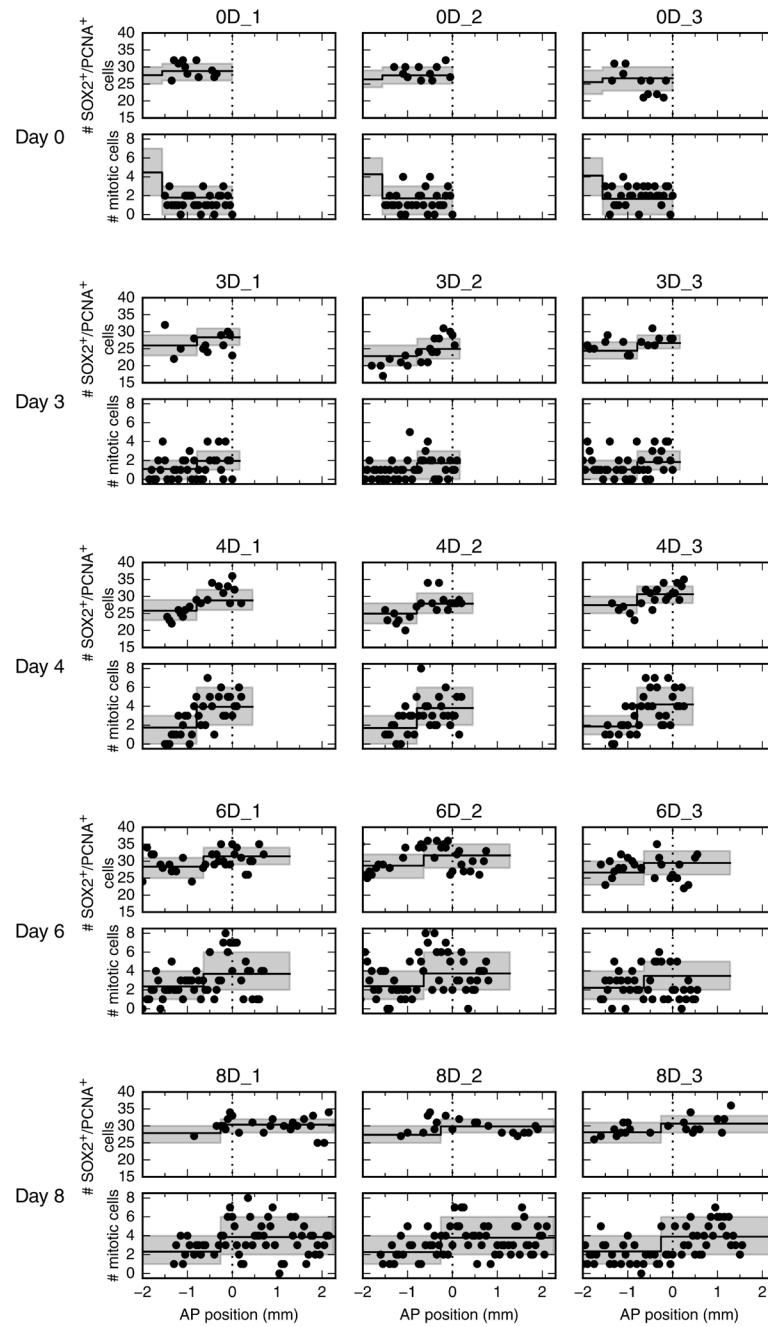


Figure S3.: Number of proliferating stem cells per cross section (upper panel) and mitotic cells per section (lower panel) along the AP axis for all 15 animals. Animals 0D_1 and 4D_3 are shown in figs. 3.10E and 3.10E', respectively. Each row shows 3 animals at a time point.

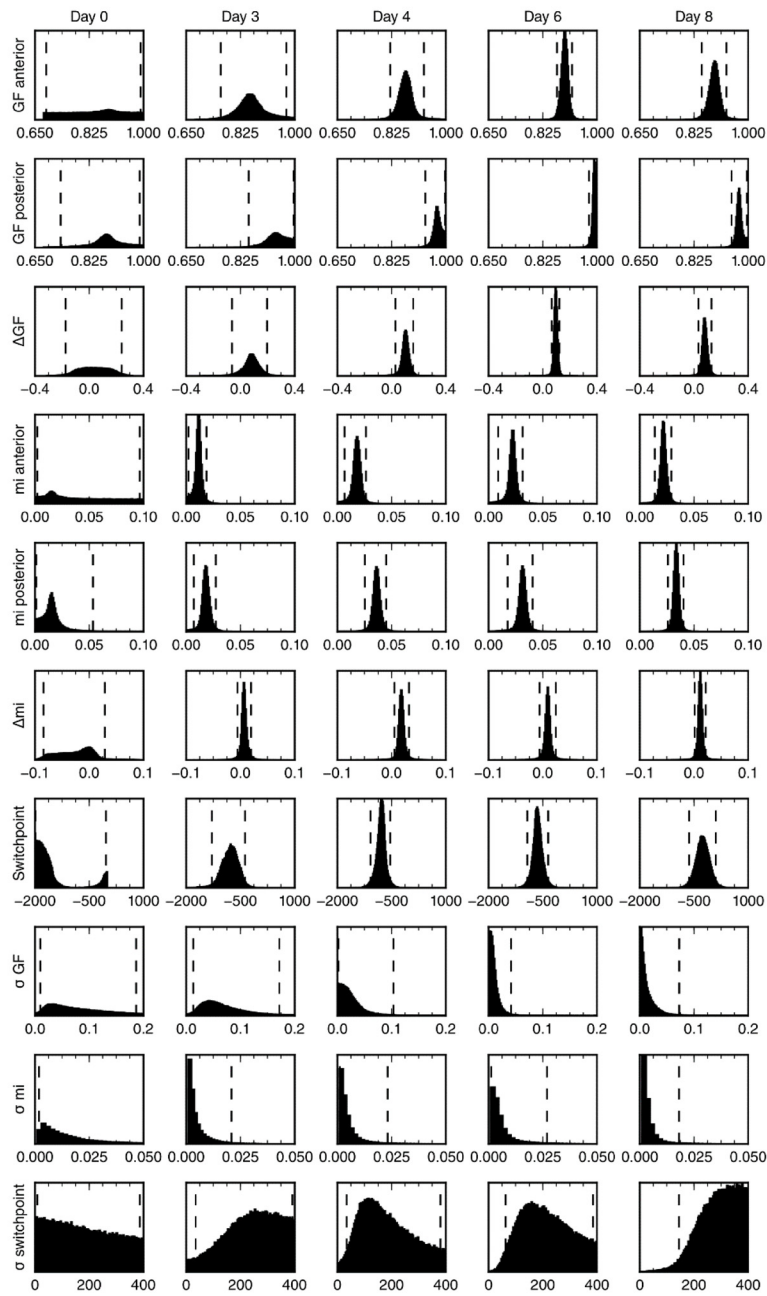


Figure S4.: Posterior marginal distributions for the parameters of the spatial model of cell counts to analyze the spatiotemporal pattern of proliferation. Each row shows a different model parameter. Each column shows a different time point. 3 animals per time point were used in the analysis. Vertical dashed lines show the limits of the 95% credibility interval. The distribution means and the 68% credibility intervals for the growth fraction, mitotic index and the switch point are shown in fig. 3.10C-C", respectively.

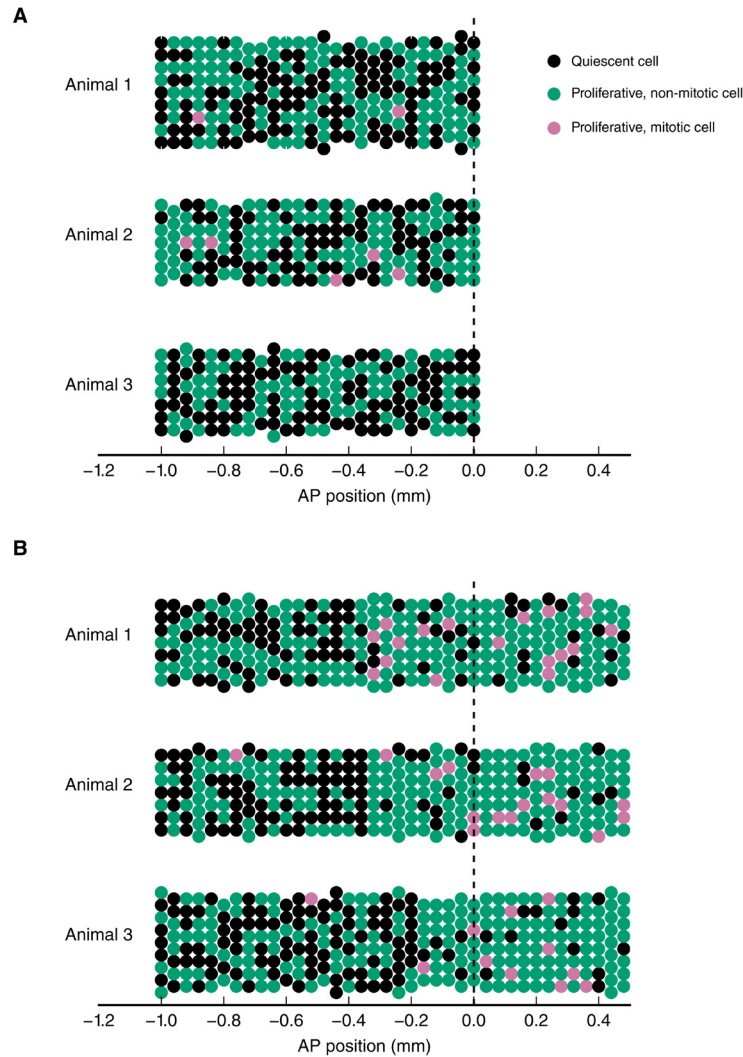


Figure S5.: Simulation of the spatial model of cell counts to analyze the spatiotemporal pattern of cell proliferation. **A**: Simulations of a spatially homogeneous zone of proliferation for 3 animals. Population mean number of stem cells per cross section, $NS_{pop} = 7$, inter-animal standard deviation for number of stem cells per cross section, $\sigma_{pop} = 1$, intra-animal standard deviation number of stem cells per cross section, $\sigma = 0.5$, probability of a cell to be proliferating (expected growth fraction), $p_p = 0.5$, inter-animal standard deviation of p_p , $\sigma_p = 0.04$, probability of a proliferating cell to be mitotic (expected mitotic index), $p_m = 0.015$, inter-animal standard deviation of p_m , $\sigma_m = 0.003$. **B**: Simulations of two adjacent spatially homogeneous zones of proliferation for 3 animals. Parameters for the anterior zone are the same as in (A). Probability of a cell to be proliferating and probability of a proliferating cell to be mitotic in the posterior zone are elevated to $p_p = 0.8$ and $p_m = 0.1$, respectively. The mean switch point location is $300 \mu\text{m}$ anterior to the amputation plane and the corresponding inter-animal standard deviation is $100 \mu\text{m}$. As expected, there are more proliferating and mitotic cells seen in the posterior zone. Simulation results can be used to infer growth fraction, mitotic index and switch point (Figure 3.10C-C'').

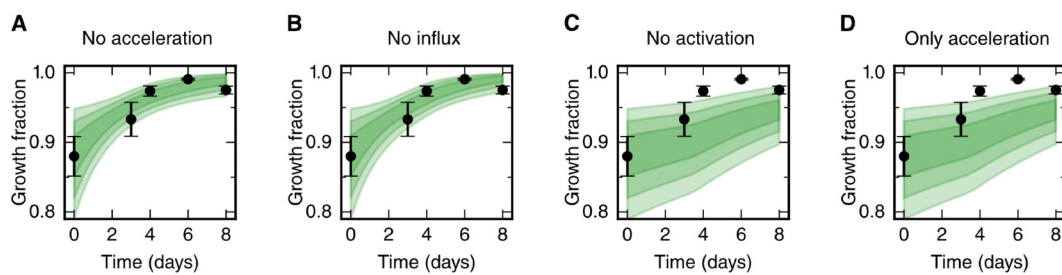


Figure S6.: Prediction of growth fraction in the high-proliferation zone for four model scenarios with selected mechanisms switched off (green shaded areas). Black dots show the same experimental data as in fig. 3.14B. Scenarios in panels A-D correspond to the scenarios in fig. 3.14D-G, respectively. Switching off the acceleration of the cell cycle length and switching off the cell influx hardly have an effect on the growth fraction time course (A,B). As expected, switching off the activation of quiescent stem cells has a strong impact on growth fraction time-course (C,D). This is consistent with the fit of a non-zero rate activation rate, k , to this data.

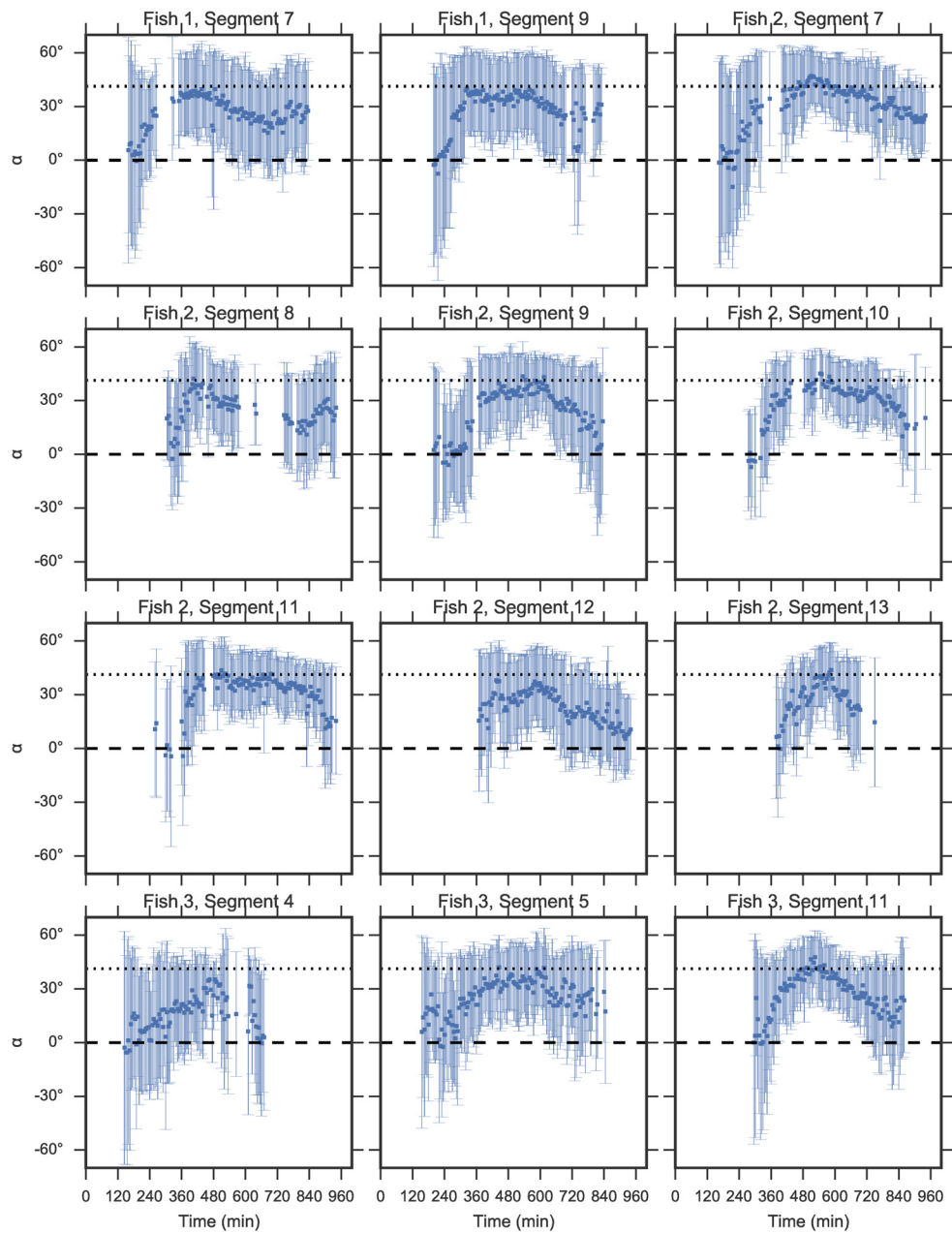


Figure S7.: Multiple time series of chevron angle, α , of embryos treated with cyclopamine. For all these segments chevrons formed with normal angle but then relaxed. Fish 2, segment 7 is also shown in Figure 4.5H.

B. SUPPLEMENTARY CALCULATIONS

B.1. OVERDAMPED DYNAMICS OF THE MECHANICAL MODEL OF CHEVRON FORMATION

Assuming viscous damping, the overdamped equations of motion of our model system follow from the energy equation given in fig. 4.7D as

$$\frac{\partial \alpha_i}{\partial t} = \frac{-1}{cL^2} \frac{\partial E}{\partial \alpha_i}, i = 1 \dots n, \quad (\text{B.1})$$

where I introduced the viscous damping coefficient c . Defining the dimensionless energy,

$$\tilde{E} = \frac{E}{K_x L^2}, \quad (\text{B.2})$$

and the dimensionless time,

$$\tilde{t} = t \frac{c}{K_x}, \quad (\text{B.3})$$

the dimensionless equations of motion read

$$\frac{\partial \alpha_i}{\partial \tilde{t}} = \frac{-\partial E_n}{\partial \alpha_i} = -(2 + K)\alpha_i + \alpha_{i-1} + \alpha_{i+1}, i = 1 \dots n. \quad (\text{B.4})$$

As all segments are formed straight, the initial conditions read

$$\alpha_j(t = 0) = 0. \quad (\text{B.5})$$

A numerical solution of the equations of motion for 7 segments is shown in fig. 4.7F.

B.2. MATHEMATICAL MODEL OF NEURON TURNOVER IN THE ADULT HUMAN HIPPOCAMPUS

Here, I give the model equations that were developed by Spalding et al. (2013) and that are needed for the statistical inference performed in chapter 5. The turnover model is given by the transport equation

$$\frac{\partial n(t, a)}{\partial t} + \frac{\partial n(t, a)}{\partial a} = -\gamma(t, a)n(t, a), \quad (\text{B.6})$$

where $n(t, a)$ is the cell density (in units of cells/age-interval), t is the age of the subject (time after birth), a is the age of the cells and $\gamma(t, a)$ is the cell death rate. The initial condition $n(-0.5, a)$ describes the cell population at 6 months prior to birth of the subject. The boundary condition,

$$n(t, 0) = b(t), \quad (\text{B.7})$$

specifies the cell birth rate. After specifying the functional form of $\gamma(t, a)$ and $b(t)$ with parameters p_1, \dots, p_k , eqs. (B.6) and (B.7) can be solved numerically to obtain the predicted cell density, $n(t_d - t_b, a; p_1, \dots, p_k)$ for a subject that was born at t_b and died at t_d . From that, the predicted average ^{14}C concentration, \tilde{C} , of a subject can be calculated by:

$$\tilde{C}(t_b, t_d; p_1, \dots, p_k) = \frac{\int_0^{t_d - t_b} K_{lag}(t_d - a)n(t_d - t_b, a; p_1, \dots, p_k)da}{\int_0^{t_d - t_b} n(t_d - t_b, a; p_1, \dots, p_k)da}, \quad (\text{B.8})$$

where $K_{lag}(t_d - a)$ is the ^{14}C concentration written in the DNA of cells with age a . As ^{14}C is mainly taken up via food it is reasonable to assume a delay between the atmospheric ^{14}C concentration, $K(t)$, and the ^{14}C concentration written in the DNA of cells, $K_{lag}(t)$. The simplest way to model this delay is to assume

$$K_{lag}(t) = K(t - t_{lag}). \quad (\text{B.9})$$

In accordance with Spalding et al. (2013), I use this form with $t_{lag} = 1$ year. The authors implemented different versions of the model, termed scenarios. Depending on the complexity of the scenario, each scenario has a different number of parameters, k . By fitting the scenario predictions to the measured ^{14}C concentrations they estimated the neuron turnover parameters and selected the best fitting scenario.

Here, I will focus on only two of the scenarios examined by Spalding et al. (2013), namely the simplest scenario, termed A, and the scenario selected by Spalding et al. (2013) as best fitting, termed 2POP. For both scenarios the total cell number and the cell

death rate are assumed to be constant and hence

$$\gamma(t, a) = b(t) = r, \quad (\text{B.10})$$

where r is the turnover rate. In scenario A, all cells are replaced with a constant turnover rate, r . Hence, r is the only model parameter in scenario A. In scenario 2POP, only a fraction of cells, f , undergoes turnover at constant rate, r . Therefore, the model parameters in scenario 2POP are r and f . Please note, that the special case of scenario 2POP in which $f = 1$ is identical to scenario A.

LIST OF FIGURES

1.1. The aim of this thesis	4
3.1. Idealized scheme of the tube-like structure of the spinal cord, definition of stem cell density along anteroposterior axis	22
3.2. Spinal cord cross sections	23
3.3. Definition of spatial zones in the axolotl spinal cord	24
3.4. Spinal cord outgrowth during regeneration after amputation	25
3.5. Proliferation-driven outgrowth model of spinal cord outgrowth	26
3.6. Fitting proliferation models to outgrowth time-course	28
3.7. Possible cell behaviors that could lead to spinal cord outgrowth	31
3.8. Stem cell length does not change during regeneration	32
3.9. Number of stem cells per cross section is constant	33
3.10. Spatiotemporal pattern of proliferation	35
3.11. Proliferation rate time-course	38
3.12. Total number of SOX2 ⁺ /PCNA ⁻ cells in the high-proliferation zone	40
3.13. Cell movements in the regenerating spinal cord	41
3.14. Mechanistic model of spinal cord outgrowth	43
3.15. Comparison of outgrowth model prediction with a <i>Sox2</i> knockout condition	46
3.16. Regeneration of chevron shaped muscle segments in axolotl	48
3.17. Cell cycle analyses of mesenchymal tail blastemas after amputations	48
3.18. Conceptual model of spinal cord growth during regeneration	54
4.1. Trunk and segment morphology of a developing zebrafish embryo	59
4.2. Quantification of chevron formation	63
4.3. Empirical model of chevron angle time course	64
4.4. Chevron formation for mobile and immobile embryos	66
4.5. Role of muscle pioneers in chevron maintenance, but not formation	68
4.6. Summary of chevron dynamics	72
4.7. A mechanical model for the establishment of chevron angles	74

5.1.	Concentration of the carbon isotope ^{14}C in the atmosphere and hippocampal neuron genomic DNA	80
5.2.	Comparison of parameter estimates for the LS and ML methods	84
5.3.	Log-likelihood profile for the turnover rate, r , in scenario 2POP	85
5.4.	Estimation of additional number of subjects needed to infer turnover rate	86
S1.	Images used for spinal cord outgrowth measurements in fig. 3.4	96
S2.	Number of stem cells per cross section along the AP axis for all 15 animals	97
S3.	Number of proliferating stem cells per cross section and mitotic cells per section along the AP axis for all 15 animals	98
S4.	Posterior marginal distributions for the parameters of the spatial model of cell counts to analyze the spatiotemporal pattern of proliferation	99
S5.	Simulation of the spatial model of cell counts to analyze the spatiotemporal pattern of cell proliferation	100
S6.	Prediction of growth fraction in the high-proliferation zone for four model scenarios with selected mechanisms switched off	101
S7.	Multiple time series of chevron angle, α , of embryos treated with cyclopamine	102

LIST OF TABLES

3.1. Parameter estimates for proliferation models.	27
3.2. Log-likelihood, number of free parameters, AICc and ER of the proliferation models	30
3.3. Progenitor cell number and spatial extent in blastema	50
4.1. Percentage of embryos showing significant chevron formation	65
5.1. Comparison of parameter estimates for the LS and ML methods for scenario A	82
5.2. Comparison of parameter estimates for the LS and ML methods for scenario 2POP	83
5.3. Comparison of the model scenarios for ¹⁴ C incorporation	83

BIBLIOGRAPHY

- Agassiz, L. and K. C. Vogt (1845). *Anatomie Des Salmones*. Neuchâtel: Wolfrath.
- Akaike, H. (1974). A New Look at the Statistical Model Identification. *IEEE Trans. Autom. Control* 19.6, pp. 716–723. DOI: 10.1109/TAC.1974.1100705.
- Alberts, B. (2015). *Molecular Biology of the Cell*. New York: Garland Science.
- Alexander, R. M. N. (1969). The Orientation of Muscle Fibres in the Myomeres of Fishes. *J. Mar. Biol. Assoc. U. K.* 49.2, pp. 263–290. DOI: 10.1017/S0025315400035906.
- Arner, E., P. O. Westermark, K. L. Spalding, T. Britton, M. Rydén, J. Frisén, S. Bernard, and P. Arner (2010). Adipocyte Turnover: Relevance to Human Adipose Tissue Morphology. *Diabetes* 59.1, pp. 105–109. DOI: 10.2337/db09-0942.
- Arsanto, J.-P., T. E. Komorowski, F. Dupin, X. Caubit, M. Diano, J. Géraudie, B. M. Carlson, and Y. Thouveny (1992). Formation of the Peripheral Nervous System during Tail Regeneration in Urodele Amphibians: Ultrastructural and Immunohistochemical Studies of the Origin of the Cells. *J. Exp. Zool.* 264.3, pp. 273–292. DOI: 10.1002/jez.1402640307.
- Aulehla, A. and O. Pourquié (2010). Signaling Gradients during Paraxial Mesoderm Development. *Cold Spring Harb. Perspect. Biol.* 2.2, a000869. DOI: 10.1101/cshperspect.a000869.
- Barresi, M., J. D'Angelo, L. Hernandez, and S. Devoto (2001). Distinct Mechanisms Regulate Slow-Muscle Development. *Curr. Biol.* 11.18, pp. 1432–1438. DOI: 10.1016/S0960-9822(01)00428-6.
- Barrios, A., R. J. Poole, L. Durbin, C. Brennan, N. Holder, and S. W. Wilson (2003). Eph/Ephrin Signaling Regulates the Mesenchymal-to-Epithelial Transition of the Paraxial Mesoderm during Somite Morphogenesis. *Curr. Biol.* 13.18, pp. 1571–1582. DOI: 10.1016/j.cub.2003.08.030.
- Bayly, M. (1974). An Energy Calculation Concerning the Roundness of Folds. *Tectonophysics* 24.4, pp. 291–316. DOI: 10.1016/0040-1951(74)90014-6.
- Beattie, C. E. and J. S. Eisen (1997). Notochord Alters the Permissiveness of Myotome for Pathfinding by an Identified Motoneuron in Embryonic Zebrafish. *Development* 124.3, pp. 713–720.

- Becker, C. G. and R. D. del Corral (2015). Neural Development and Regeneration: It's All in Your Spinal Cord. *Development* 142.5, pp. 811–816. DOI: 10.1242/dev.121053.
- Bergmann, O., R. D. Bhardwaj, S. Bernard, S. Zdunek, F. Barnabé-Heider, S. Walsh, J. Zupicich, K. Alkass, B. A. Buchholz, H. Druid, S. Jovinge, and J. Frisé (2009). Evidence for Cardiomyocyte Renewal in Humans. *Science* 324.5923, pp. 98–102. DOI: 10.1126/science.1164680.
- Bergmann, O., J. Liebl, S. Bernard, K. Alkass, M. S. Y. Yeung, P. Steier, W. Kutschera, L. Johnson, M. Landén, H. Druid, K. L. Spalding, and J. Frisé (2012). The Age of Olfactory Bulb Neurons in Humans. *Neuron* 74.4, pp. 634–639. DOI: 10.1016/j.neuron.2012.03.030.
- Bernard, S., J. Frisé, and K. L. Spalding (2010). A Mathematical Model for the Interpretation of Nuclear Bomb Test Derived ¹⁴C Incorporation in Biological Systems. *Nucl. Instrum. Methods Phys. Res. Sect. B Beam Interact. Mater. At.* Proceedings of the Eleventh International Conference on Accelerator Mass Spectrometry 268 (7–8), pp. 1295–1298. DOI: 10.1016/j.nimb.2009.10.156.
- Bhardwaj, R. D., M. A. Curtis, K. L. Spalding, B. A. Buchholz, D. Fink, T. Björk-Eriksson, C. Nordborg, F. H. Gage, H. Druid, P. S. Eriksson, and J. Frisé (2006). Neocortical Neurogenesis in Humans Is Restricted to Development. *Proc. Natl. Acad. Sci.* 103.33, pp. 12564–12568. DOI: 10.1073/pnas.0605177103.
- Bielmeier, C., S. Alt, V. Weichselberger, M. La Fortezza, H. Harz, F. Jülicher, G. Salbreux, and A.-K. Classen (2016). Interface Contractility between Differently Fated Cells Drives Cell Elimination and Cyst Formation. *Curr. Biol.* 26.5, pp. 563–574. DOI: 10.1016/j.cub.2015.12.063.
- Blanchard, G. B., A. J. Kabla, N. L. Schultz, L. C. Butler, B. Sanson, N. Gorfinkiel, L. Mahadevan, and R. J. Adams (2009). Tissue Tectonics: Morphogenetic Strain Rates, Cell Shape Change and Intercalation. *Nat. Methods* 6.6, pp. 458–464. DOI: 10.1038/nmeth.1327.
- Bone, Q. (1978). Locomotor Muscle. In: *Locomotion*. Ed. by W. S. Hoar and D. J. Randall. Fish physiology. New York: Academic Press, pp. 361–424.
- Bone, Q. and R. H. Moore (2008). *Biology of Fishes*. 3rd ed. New York: Taylor & Francis.
- Bonner, J. T. (1974). *On Development: The Biology of Form*. Cambridge: Harvard University Press. 300 pp.
- Bordzilovskaya, N., T. Detlaff, S. Duhon, and G. Malacinski (1989). Developmental-Stage Series of Axolotl Embryos. In: *Developmental Biology of the Axolotl*. Ed. by J.B. Armstrong and G.M. Malacinski. New York: Oxford University Press, pp. 201–219.
- Bosveld, F., I. Bonnet, B. Guirao, S. Tlili, Z. Wang, A. Pétalot, R. Marchand, P.-L. Bardet, P. Marcq, F. Graner, and Y. Bellaïche (2012). Mechanical Control of Morphogenesis by Fat/Dachsous/Four-Jointed Planar Cell Polarity Pathway. *Science* 336.6082, pp. 724–727. DOI: 10.1126/science.1221071.
- Burnham, K. P. and D. R. Anderson (2002). *Model Selection and Multimodel Inference: A Practical Information Theoretic Approach*. 2nd ed. New York: Springer. 488 pp.

- Chara, O., E. M. Tanaka, and L. Bruschi (2014). Mathematical Modeling of Regenerative Processes. *Curr. Top. Dev. Biol.* 108, pp. 283–317. DOI: 10.1016/B978-0-12-391498-9.00011-5.
- Chernoff, E. A., D. L. Stocum, H. L. Nye, and J. A. Cameron (2003). Urodele Spinal Cord Regeneration and Related Processes. *Dev. Dyn.* 226.2, pp. 295–307. DOI: 10.1002/dvdy.10240.
- Chevrel, R. (1913). Essai Sur La Morphologie et La Physiologie Du Muscle Latéral Chez Les Poissons Osseux. *Arch. Zool. Expérimentale Générale* 52, pp. 473–607.
- Chickarmane, V., A. H. K. Roeder, P. T. Tarr, A. Cunha, C. Tobin, and E. M. Meyerowitz (2010). Computational Morphodynamics: A Modeling Framework to Understand Plant Growth. *Annu. Rev. Plant Biol.* 61.1, pp. 65–87. DOI: 10.1146/annurev-arplant-042809-112213.
- Clelland, C. D., M. Choi, C. Romberg, G. D. Clemenson, A. Fragniere, P. Tyers, S. Jessberger, L. M. Saksida, R. A. Barker, F. H. Gage, and T. J. Bussey (2009). A Functional Role for Adult Hippocampal Neurogenesis in Spatial Pattern Separation. *Science* 325.5937, pp. 210–213. DOI: 10.1126/science.1173215.
- Cortés, F., D. Daggett, R. J. Bryson-Richardson, C. Neyt, J. Maule, P. Gautier, G. E. Hollway, D. Keenan, and P. D. Currie (2003). Cadherin-Mediated Differential Cell Adhesion Controls Slow Muscle Cell Migration in the Developing Zebrafish Myotome. *Dev. Cell* 5.6, pp. 865–876. DOI: 10.1016/S1534-5807(03)00362-9.
- Crick, F. (1970). Diffusion in Embryogenesis. *Nature* 225.5231, pp. 420–422. DOI: 10.1038/225420a0.
- Currie, J. D., A. Kawaguchi, R. M. Traspas, M. Schuez, O. Chara, and E. M. Tanaka (2016). Live Imaging of Axolotl Digit Regeneration Reveals Spatiotemporal Choreography of Diverse Connective Tissue Progenitor Pools. *Dev. Cell* 39.4, pp. 411–423. DOI: 10.1016/j.devcel.2016.10.013.
- Currie, P. D. and P. W. Ingham (1996). Induction of a Specific Muscle Cell Type by a Hedgehog-like Protein in Zebrafish. *Nature* 382.6590, pp. 452–455. DOI: 10.1038/382452a0.
- Daggett, D., C. R. Domingo, P. D. Currie, and S. L. Amacher (2007). Control of Morphogenetic Cell Movements in the Early Zebrafish Myotome. *Dev. Biol.* 309.2, pp. 169–179. DOI: 10.1016/j.ydbio.2007.06.008.
- D'Agostino, R. B. (1971). An Omnibus Test of Normality for Moderate and Large Size Samples. *Biometrika* 58.2, pp. 341–348. DOI: 10.1093/biomet/58.2.341.
- D'Agostino, R. and E. S. Pearson (1973). Tests for Departure from Normality. *Biometrika* 60.3, pp. 613–622. DOI: 10.1093/biomet/60.3.613.
- De Back, W. (2015). *Multicellular Systems Biology of Development*. PhD Thesis. Dresden: Technische Universität Dresden.
- Delsuc, F., H. Brinkmann, D. Chourrout, and H. Philippe (2006). Tunicates and Not Cephalochordates Are the Closest Living Relatives of Vertebrates. *Nature* 439.7079, pp. 965–968. DOI: 10.1038/nature04336.

- Dent, J. N. (1956). Observations on the Life History and Development of *Leptodactylus Albilabris*. *Copeia* 1956.4, pp. 207–210.
- Devoto, S. H., E. Melançon, J. S. Eisen, and M. Westerfield (1996). Identification of Separate Slow and Fast Muscle Precursor Cells in Vivo, Prior to Somite Formation. *Development* 122.11, pp. 3371–3380.
- Dolez, M., J.-F. Nicolas, and E. Hirsinger (2011). Laminins, via Heparan Sulfate Proteoglycans, Participate in Zebrafish Myotome Morphogenesis by Modulating the Pattern of Bmp Responsiveness. *Development* 138.1, pp. 97–106. DOI: 10.1242/dev.053975.
- Driever, W. and C. Nüsslein-Volhard (1988). The Bicoid Protein Determines Position in the *Drosophila* Embryo in a Concentration-Dependent Manner. *Cell* 54.1, pp. 95–104. DOI: 10.1016/0092-8674(88)90183-3.
- Du, S. J., S. H. Devoto, M. Westerfield, and R. T. Moon (1997). Positive and Negative Regulation of Muscle Cell Identity by Members of the Hedgehog and TGF- β Gene Families. *J. Cell Biol.* 139.1, pp. 145–156. DOI: 10.1083/jcb.139.1.145.
- Durbin, L., P. Sordino, A. Barrios, M. Gering, C. Thisse, B. Thisse, C. Brennan, A. Green, S. Wilson, and N. Holder (2000). Anteroposterior Patterning Is Required within Segments for Somite Boundary Formation in Developing Zebrafish. *Development* 127.8, pp. 1703–1713.
- Eckenhoff, M. F. and P. Rakic (1988). Nature and Fate of Proliferative Cells in the Hippocampal Dentate Gyrus during the Life Span of the Rhesus Monkey. *J. Neurosci.* 8.8, pp. 2729–2747.
- Edelstein-Keshet, L. (2005). *Mathematical Models in Biology*. Classics in Applied Mathematics. Philadelphia: Society for Industrial and Applied Mathematics. 615 pp.
- Eriksson, P. S., E. Perfilieva, T. Björk-Eriksson, A.-M. Alborn, C. Nordborg, D. A. Peterson, and F. H. Gage (1998). Neurogenesis in the Adult Human Hippocampus. *Nat. Med.* 4.11, pp. 1313–1317. DOI: 10.1038/3305.
- Ernst, A., K. Alkass, S. Bernard, M. Salehpour, S. Perl, J. Tisdale, G. Possnert, H. Druid, and J. Frisén (2014). Neurogenesis in the Striatum of the Adult Human Brain. *Cell* 156.5, pp. 1072–1083. DOI: 10.1016/j.cell.2014.01.044.
- Etournay, R., M. Merkel, M. Popović, H. Brandl, N. A. Dye, B. Aigouy, G. Salbreux, S. Eaton, and F. Jülicher (2016). TissueMiner: A Multiscale Analysis Toolkit to Quantify How Cellular Processes Create Tissue Dynamics. *eLife* 5, e14334. DOI: 10.7554/eLife.14334.
- Etournay, R., M. Popović, M. Merkel, A. Nandi, C. Blasse, B. Aigouy, H. Brandl, G. Myers, G. Salbreux, F. Jülicher, and S. Eaton (2015). Interplay of Cell Dynamics and Epithelial Tension during Morphogenesis of the *Drosophila* Pupal Wing. *eLife* 4, e07090. DOI: 10.7554/eLife.07090.
- Fan, C. and M. Tessierlavigne (1994). Patterning of Mammalian Somites by Surface Ectoderm and Notochord - Evidence for Sclerotome Induction by a Hedgehog Homolog. *Cell* 79.7, pp. 1175–1186. DOI: 10.1016/0092-8674(94)90009-4.
- Fei, J.-F., M. Schuez, A. Tazaki, Y. Taniguchi, K. Roensch, and E. M. Tanaka (2014). CRISPR-Mediated Genomic Deletion of Sox2 in the Axolotl Shows a Requirement in

- Spinal Cord Neural Stem Cell Amplification during Tail Regeneration. *Stem Cell Rep.* 3.3, pp. 444–459. DOI: 10.1016/j.stemcr.2014.06.018.
- Feng, X., E. G. Adiarte, and S. H. Devoto (2006). Hedgehog Acts Directly on the Zebrafish Dermomyotome to Promote Myogenic Differentiation. *Dev. Biol.* 300.2, pp. 736–746. DOI: 10.1016/j.ydbio.2006.08.056.
- Francis, E. T. B. (1934). *The Anatomy of the Salamander*. Oxford: Oxford University Press. 482 pp.
- Fruciano, C. (2016). Measurement Error in Geometric Morphometrics. *Dev. Genes Evol.* 226.3, pp. 139–158. DOI: 10.1007/s00427-016-0537-4.
- Gaete, M., R. Muñoz, N. Sánchez, R. Tampe, M. Moreno, E. G. Contreras, D. Lee-Liu, and J. Larraín (2012). Spinal Cord Regeneration in *Xenopus* Tadpoles Proceeds through Activation of Sox2-Positive Cells. *Neural Develop.* 7, p. 13. DOI: 10.1186/1749-8104-7-13.
- Gegenbaur, C. (1859). *Grundzüge der vergleichenden Anatomie*. Leipzig: Wilhelm Engelmann. 632 pp.
- Getto, P. and A. Marciniak-Czochra (2015). Mathematical Modelling as a Tool to Understand Cell Self-Renewal and Differentiation. In: *Mammary Stem Cells*. Ed. by M. d. M. Vivanco. Vol. 1293. Methods in Molecular Biology. Springer New York, pp. 247–266. DOI: 10.1007/978-1-4939-2519-3_15.
- Gierer, A. and H. Meinhardt (1972). A Theory of Biological Pattern Formation. *Kybernetik* 12.1, pp. 30–39. DOI: 10.1007/BF00289234.
- Gilbert, S. F. (2010). *Developmental Biology*. 9th ed. Sunderland: Sinauer.
- Graner, F. and J. A. Glazier (1992). Simulation of Biological Cell Sorting Using a Two-Dimensional Extended Potts Model. *Phys. Rev. Lett.* 69.13, pp. 2013–2016. DOI: 10.1103/PhysRevLett.69.2013.
- Gray, R. S., R. D. Bayly, S. A. Green, S. Agarwala, C. J. Lowe, and J. B. Wallingford (2009). Diversification of the Expression Patterns and Developmental Functions of the Dishevelled Gene Family during Chordate Evolution. *Dev. Dyn.* 238.8, pp. 2044–2057. DOI: 10.1002/dvdy.22028.
- Greene, C. W. and C. H. Greene (1913). The Skeletal Musculature of the King Salmon. *Fish. Bull.* 33.1, pp. 21–60.
- Guirao, B., S. U. Rigaud, F. Bosveld, A. Bailles, J. López-Gay, S. Ishihara, K. Sugimura, F. Graner, and Y. Bellaïche (2015). Unified Quantitative Characterization of Epithelial Tissue Development. *eLife* 4, e08519. DOI: 10.7554/eLife.08519.
- Halpern, M., R. Ho, C. Walker, and C. Kimmel (1993). Induction of Muscle Pioneers and Floor Plate Is Distinguished by the Zebrafish No Tail Mutation. *Cell* 75.1, pp. 99–111. DOI: 10.1016/0092-8674(93)90682-G.
- Hammerschmidt, M., M. J. Bitgood, and A. P. McMahon (1996). Protein Kinase A Is a Common Negative Regulator of Hedgehog Signaling in the Vertebrate Embryo. *Genes Dev.* 10.6, pp. 647–658. DOI: 10.1101/gad.10.6.647.
- Harder, W. (1964a). *Handbuch Der Binnenfischerei Mitteleuropas - Bd. 2,A: Anatomie Der Fische, Abbildungsteil*. Stuttgart: Schweizerbart.

- Harder, W. (1964b). *Handbuch Der Binnenfischerei Mitteleuropas - Bd. 2,A: Anatomie Der Fische, Textteil*. Stuttgart: Schweizerbart.
- Harrison, R. G. (1898). The Growth and Regeneration of the Tail of the Frog Larva. *Arch. Für Entwicklungsmechanik Org.* 7, pp. 430–485.
- Hatschek, B. (1882). Studien Über Die Entwicklung Des Amphioxus. *Arb. Aus Dem Zool. Instituten Univ. Wien Zool. Stn. Triest* 4.1, pp. 1–88.
- (1893). *The Amphioxus and Its Development*. Ed. and trans. by J. Tuckey. London: Swan, Sonnenschein & co.
- Hatta, K., R. Bremiller, M. Westerfield, and C. Kimmel (1991). Diversity of Expression of Engrailed-like Antigens in Zebrafish. *Development* 112.3, pp. 821–832.
- Heisenberg, C.-P. and Y. Bellaïche (2013). Forces in Tissue Morphogenesis and Patterning. *Cell* 153.5, pp. 948–962. DOI: 10.1016/j.cell.2013.05.008.
- Henry, C., I. McNulty, W. Durst, S. Munchel, and S. Amacher (2005). Interactions between Muscle Fibers and Segment Boundaries in Zebrafish. *Dev. Biol.* 287.2, pp. 346–360. DOI: 10.1016/j.ydbio.2005.08.049.
- Henry, C. A. and S. L. Amacher (2004). Zebrafish Slow Muscle Cell Migration Induces a Wave of Fast Muscle Morphogenesis. *Dev. Cell* 7.6, pp. 917–923. DOI: 10.1016/j.devcel.2004.09.017.
- Herrgen, L., C. Schröter, L. Bajard, and A. C. Oates (2009). Multiple Embryo Time-Lapse Imaging of Zebrafish Development. In: *Zebrafish*. Ed. by G. J. Lieschke, A. C. Oates, and K. Kawakami. Vol. 546. Methods in Molecular Biology. Humana Press, pp. 243–254. DOI: 10.1007/978-1-60327-977-2_15.
- Hilborn, R. and M. Mangel (1997). *The Ecological Detective, Confronting Models with Data*. Princeton: Princeton University Press.
- Holley, S. A., R. Geisler, and C. Nüsslein-Volhard (2000). Control of Her1 Expression during Zebrafish Somitogenesis by a Delta-Dependent Oscillator and an Independent Wave-Front Activity. *Genes Dev.* 14.13, pp. 1678–1690.
- Holtzer, S. W. (1956). The Inductive Activity of the Spinal Cord in Urodele Tail Regeneration. *J. Morphol.* 99.1, pp. 1–39. DOI: 10.1002/jmor.1050990102.
- Honjo, Y. and J. S. Eisen (2005). Slow Muscle Regulates the Pattern of Trunk Neural Crest Migration in Zebrafish. *Development* 132.20, pp. 4461–4470. DOI: 10.1242/dev.02026.
- Hooke, R. (1665). *Micrographia*. London.
- Hui, S. P., A. Dutta, and S. Ghosh (2010). Cellular Response after Crush Injury in Adult Zebrafish Spinal Cord. *Dev. Dyn.* 239.11, pp. 2962–2979. DOI: 10.1002/dvdy.22438.
- Hui, S. P., T. C. Nag, and S. Ghosh (2015). Characterization of Proliferating Neural Progenitors after Spinal Cord Injury in Adult Zebrafish. *PloS One* 10.12, e0143595. DOI: 10.1371/journal.pone.0143595.
- Hunter, J. D. (2007). Matplotlib: A 2D Graphics Environment. *Comput. Sci. Eng.* 9.3, pp. 90–95. DOI: 10.1109/MCSE.2007.55.
- James, F. and M. Roos (1975). Minuit - a System for Function Minimization and Analysis of the Parameter Errors and Correlations. *Comput. Phys. Commun.* 10.6, pp. 343–367. DOI: 10.1016/0010-4655(75)90039-9.

- Johnston, I. A., N. I. Bower, and D. J. Macqueen (2011). Growth and the Regulation of Myotomal Muscle Mass in Teleost Fish. *J. Exp. Biol.* 214.10, pp. 1617–1628. DOI: 10.1242/jeb.038620.
- Jones, E., T. Oliphant, P. Peterson, et al. (2001). *SciPy: Open Source Scientific Tools for Python*. URL: <http://www.scipy.org/> (visited on 2016).
- Karner, C. M., R. Chirumamilla, S. Aoki, P. Igarashi, J. B. Wallingford, and T. J. Carroll (2009). Wnt9b Signaling Regulates Planar Cell Polarity and Kidney Tubule Morphogenesis. *Nat. Genet.* 41.7, pp. 793–799. DOI: 10.1038/ng.400.
- Kästner, S. (1892). Ueber Die Allgemeine Entwicklung Der Rumpf- Und Schwanzmuskulatur Bei Wirbelthieren. Mit Besonderer Berücksichtigung Der Selachier. *Anat. Abt. Arch. Für Anat. Physiol.* pp. 153–222.
- Keener, J. and J. Sneyd (1998). *Mathematical Physiology*. Vol. 8. Interdisciplinary applied mathematics: Mathematical biology. New York: Springer. 766 pp.
- Keller, P. J., A. D. Schmidt, J. Wittbrodt, and E. H. Stelzer (2008). Reconstruction of Zebrafish Early Embryonic Development by Scanned Light Sheet Microscopy. *Science* 322.5904, pp. 1065–1069. DOI: 10.1126/science.1162493.
- Keller, R., J. Shih, and A. Sater (1992a). The Cellular Basis of the Convergence and Extension of the Xenopus Neural Plate. *Dev. Dyn.* 193.3, pp. 199–217. DOI: 10.1002/aja.1001930302.
- Keller, R., J. Shih, A. K. Sater, and C. Moreno (1992b). Planar Induction of Convergence and Extension of the Neural Plate by the Organizer of Xenopus. *Dev. Dyn.* 193.3, pp. 218–234. DOI: 10.1002/aja.1001930303.
- Kicheva, A., T. Bollenbach, A. Ribeiro, H. P. Valle, R. Lovell-Badge, V. Episkopou, and J. Briscoe (2014). Coordination of Progenitor Specification and Growth in Mouse and Chick Spinal Cord. *Science* 345.6204, p. 1254927. DOI: 10.1126/science.1254927.
- Kimmel, C., W. Ballard, S. Kimmel, B. Ullmann, and T. Schilling (1995). Stages of Embryonic Development of the Zebrafish. *Dev. Dyn.* 203.3, pp. 253–310. DOI: 10.1002/aja.1002030302.
- Köhn-Luque, A., W. de Back, J. Starruß, A. Mattiotti, A. Deutsch, J. M. Pérez-Pomares, and M. A. Herrero (2011). Early Embryonic Vascular Patterning by Matrix-Mediated Paracrine Signalling: A Mathematical Model Study. *PloS One* 6.9, e24175. DOI: 10.1371/journal.pone.0024175.
- Kondo, S. and T. Miura (2010). Reaction-Diffusion Model as a Framework for Understanding Biological Pattern Formation. *Science* 329.5999, pp. 1616–1620. DOI: 10.1126/science.1179047.
- Koumans, J. T. M. and H. A. Akster (1995). Myogenic Cells in Development and Growth of Fish. *Comp. Biochem. Physiol. A Physiol.* 110.1, pp. 3–20. DOI: 10.1016/0300-9629(94)00150-R.
- Kreutz, C., M. M. B. Rodriguez, T. Maiwald, M. Seidl, H. E. Blum, L. Mohr, and J. Timmer (2007). An Error Model for Protein Quantification. *Bioinformatics* 23.20, pp. 2747–2753. DOI: 10.1093/bioinformatics/btm397.

- Laale, H. W. (1982). Fish Embryo Culture: Observations on Axial Cord Differentiation in Presomitic Isolates of the Zebrafish *Brachydanio Rerio* (Hamilton-Buchanan). *Can. J. Zool.* 60.7, pp. 1710–1721. DOI: 10.1139/z82-223.
- Lacalli, T. (2012). The Middle Cambrian Fossil *Pikaia* and the Evolution of Chordate Swimming. *EvoDevo* 3.1, p. 12. DOI: 10.1186/2041-9139-3-12.
- Lacroix, S., L. K. Hamilton, A. Vaugeois, S. Beaudoin, C. Breault-Dugas, I. Pineau, S. A. Lévesque, C.-A. Grégoire, and K. J. L. Fernandes (2014). Central Canal Ependymal Cells Proliferate Extensively in Response to Traumatic Spinal Cord Injury but Not Demyelinating Lesions. *PLoS One* 9.1, e85916. DOI: 10.1371/journal.pone.0085916.
- Langelaan, J. W. (1904). On the Form of the Trunk-Myotome. *K. Ned. Akad. Van Wet. Proc. Ser. B Phys. Sci.* 7, pp. 34–40.
- Lee, S. J., S. Kim, S.-C. Choi, and J.-K. Han (2010). *XpTeg* (Xenopus Proximal Tubules-Expressed Gene) Is Essential for Pronephric Mesoderm Specification and Tubulogenesis. *Mech. Dev.* 127 (1–2), pp. 49–61. DOI: 10.1016/j.mod.2009.11.001.
- Lefevre, J., D. J. Marshall, A. N. Combes, A. L. Ju, M. H. Little, and N. A. Hamilton (2013). Modelling Cell Turnover in a Complex Tissue during Development. *J. Theor. Biol.* 338, pp. 66–79. DOI: 10.1016/j.jtbi.2013.08.033.
- Lienkamp, S. S., K. Liu, C. M. Karner, T. J. Carroll, O. Ronneberger, J. B. Wallingford, and G. Walz (2012). Vertebrate Kidney Tubules Elongate Using a Planar Cell Polarity-Dependent, Rosette-Based Mechanism of Convergent Extension. *Nat. Genet.* 44.12, pp. 1382–1387. DOI: 10.1038/ng.2452.
- Lin, G. and J. M. W. Slack (2008). Requirement for Wnt and FGF Signaling in Xenopus Tadpole Tail Regeneration. *Dev. Biol.* 316.2, pp. 323–335. DOI: 10.1016/j.ydbio.2008.01.032.
- Loussouarn, G., C. El Rawadi, and G. Genain (2005). Diversity of Hair Growth Profiles. *Int. J. Dermatol.* 44, pp. 6–9. DOI: 10.1111/j.1365-4632.2005.02800.x.
- Maini, P. K., H. G. Othmer, and A. Deutsch (2017). Obituary: Hans Meinhardt (1938–2016). *Bull. Math. Biol.* pp. 1–6. DOI: 10.1007/s11538-016-0243-4.
- Mallatt, J. and N. Holland (2013). *Pikaia Gracilens* Walcott: Stem Chordate, or Already Specialized in the Cambrian? *J. Exp. Zoolog. B Mol. Dev. Evol.* 320.4, pp. 247–271. DOI: 10.1002/jez.b.22500.
- Maurer, F. (1913). Die Ventrale Rumpfmuskulatur Der Fische (Selachier, Ganoiden, Teleostier, Crossopterygier, Dipnoer). *Jenaische Z. Für Naturwissenschaft* 49, pp. 1–118.
- Mchedlishvili, L., H. H. Epperlein, A. Telzerow, and E. M. Tanaka (2007). A Clonal Analysis of Neural Progenitors during Axolotl Spinal Cord Regeneration Reveals Evidence for Both Spatially Restricted and Multipotent Progenitors. *Development* 134.11, pp. 2083–2093. DOI: 10.1242/dev.02852.
- Mchedlishvili, L., V. Mazurov, K. S. Grassme, K. Goehler, B. Robl, A. Tazaki, K. Roensch, A. Duemmler, and E. M. Tanaka (2012). Reconstitution of the Central and Peripheral Nervous System during Salamander Tail Regeneration. *Proc. Natl. Acad. Sci.* 109.34, E2258–E2266. DOI: 10.1073/pnas.1116738109.

- McKinney, W. (2010). "Data Structures for Statistical Computing in Python." In: *Proceedings of the 9th Python in Science Conference*. Ed. by S. van der Walt and J. Millman, pp. 51–56.
- Meyers, J., J. Planamento, P. Ebrom, N. Krulewitz, E. Wade, and M. Pownall (2013). Sulf1 Modulates BMP Signaling and Is Required for Somite Morphogenesis and Development of the Horizontal Myoseptum. *Dev. Biol.* DOI: 10.1016/j.ydbio.2013.04.002.
- Millman, K. J. and M. Aivazis (2011). Python for Scientists and Engineers. *Comput. Sci. Eng.* 13.2, pp. 9–12. DOI: 10.1109/MCSE.2011.36.
- Morin-Kensicki, E. M., E. Melancon, and J. S. Eisen (2002). Segmental Relationship between Somites and Vertebral Column in Zebrafish. *Development* 129.16, pp. 3851–3860.
- Morris, S. C. and J.-B. Caron (2012). Pikaia Gracilens Walcott, a Stem-Group Chordate from the Middle Cambrian of British Columbia. *Biol. Rev.* 87.2, pp. 480–512. DOI: 10.1111/j.1469-185x.2012.00220.x.
- Müller, J. (1836). Vergleichende Anatomie Der Myxinoiden, Der Cyclostomen Mit Durchbohrtem Gaumen. Erster Theil. Osteologie Und Myologie. *Abh. K. Akad. Wiss. Zu Berl.* 1834, pp. 65–340.
- Murawala, P., E. M. Tanaka, and J. D. Currie (2012). Regeneration: The Ultimate Example of Wound Healing. *Semin. Cell Dev. Biol.* Wound Repair 23.9, pp. 954–962. DOI: 10.1016/j.semcdb.2012.09.013.
- Murray, J. D. (2002). *Mathematical Biology: I. An Introduction*. 3rd ed. New York: Springer. 551 pp.
- Nacu, E. and E. M. Tanaka (2011). Limb Regeneration: A New Development? *Annu. Rev. Cell Dev. Biol.* 27.1, pp. 409–440. DOI: 10.1146/annurev-cellbio-092910-154115.
- Nakashiba, T., J. D. Cushman, K. A. Pelkey, S. Renaudineau, D. L. Buhl, T. J. McHugh, V. R. Barrera, R. Chittajallu, K. S. Iwamoto, C. J. McBain, M. S. Fanselow, and S. Tonegawa (2012). Young Dentate Granule Cells Mediate Pattern Separation, Whereas Old Granule Cells Facilitate Pattern Completion. *Cell* 149.1, pp. 188–201. DOI: 10.1016/j.cell.2012.01.046.
- Nicolis, G. and A. D. Wit (2007). Reaction-Diffusion Systems. *Scholarpedia* 2.9, p. 1475. DOI: 10.4249/scholarpedia.1475.
- Nowakowski, R. S., S. B. Lewin, and M. W. Miller (1989). Bromodeoxyuridine Immunohistochemical Determination of the Lengths of the Cell Cycle and the DNA-Synthetic Phase for an Anatomically Defined Population. *J. Neurocytol.* 18.3, pp. 311–318. DOI: 10.1007/BF01190834.
- Nursall, J. (1956). The Lateral Musculature and the Swimming of Fish. *Proc. Zool. Soc. Lond.* 126, pp. 127–143. DOI: 10.1111/j.1096-3642.1956.tb00429.x.
- Nydal, R. and K. Lövseth (1965). Distribution of Radiocarbon from Nuclear Tests. *Nature* 206.4988, pp. 1029–1031. DOI: 10.1038/2061029a0.

- Oates, A. C., N. Gorfinkiel, M. Gonzalez-Gaitan, and C.-P. Heisenberg (2009). Quantitative Approaches in Developmental Biology. *Nat. Rev. Genet.* 10.8, pp. 517–530. DOI: 10.1038/nrg2548.
- Oliphant, T. E. (2007). Python for Scientific Computing. *Comput. Sci. Eng.* 9.3, pp. 10–20. DOI: 10.1109/MCSE.2007.58.
- Olive, K. A. et al. (2014). Review of Particle Physics. *Chin. Phys. C* 38.9, p. 090001. DOI: 10.1088/1674-1137/38/9/090001.
- Pantazis, P. and W. Supatto (2014). Advances in Whole-Embryo Imaging: A Quantitative Transition Is Underway. *Nat. Rev. Mol. Cell Biol.* 15.5, pp. 327–339. DOI: 10.1038/nrm3786.
- Patil, A., D. Huard, and C. J. Fonnesbeck (2010). PyMC: Bayesian Stochastic Modelling in Python. *J. Stat. Softw.* 35.4, pp. 1–81.
- Pietsch, P. (1993). Retinoic Acid Treatment Inhibits Mitosis in the Pre-Existing Spinal Cord during Tail Regeneration of the Axolotl Larva, *Ambystoma Mexicanum*. *Cytobios* 76.304, pp. 7–11.
- Pietsch, P. (1987). The Effects of Retinoic Acid on Mitosis during Tail and Limb Regeneration in the Axolotl Larva, *Ambystoma Mexicanum*. *Roux's Arch. Dev. Biol.* 196.3, pp. 169–175. DOI: 10.1007/BF00376311.
- Press, W. H., S. A. Teukolsky, W. Vetterling T., and B. P. Flannery (1996). *Numerical Recipes in C*. 2nd ed. Cambridge: Cambridge University Press. 994 pp.
- Prince, V. E., L. Joly, M. Ekker, and R. K. Ho (1998). Zebrafish Hox Genes: Genomic Organization and Modified Colinear Expression Patterns in the Trunk. *Development* 125.3, pp. 407–420.
- Prpic, N.-M. and N. Posnien (2016). Size and Shape—integration of Morphometrics, Mathematical Modelling, Developmental and Evolutionary Biology. *Dev. Genes Evol.* 226.3, pp. 109–112. DOI: 10.1007/s00427-016-0536-5.
- Quintero, A., M. Myllykoski, A. Igolkina, A. Fretloft, N. Dixit, and F. Rost (2012). Morphogenesis and Dynamics of Multicellular Systems. *ECMI Newsl.* 52, pp. 27–30.
- Rakic, P. (1985). Limits of Neurogenesis in Primates. *Science* 227.4690, pp. 1054–1056. DOI: 10.1126/science.3975601.
- Raue, A., M. Schilling, J. Bachmann, A. Matteson, M. Schelke, D. Kaschek, S. Hug, C. Kreutz, B. D. Harms, F. J. Theis, U. Klingmüller, and J. Timmer (2013). Lessons Learned from Quantitative Dynamical Modeling in Systems Biology. *PLoS One* 8.9, e74335. DOI: 10.1371/journal.pone.0074335.
- Rauther, M. (1940). *1. Abt., 2. Buch: Echte Fische*. Vol. 6. Dr. H.G. Bronns Klassen und Ordnungen des Tierreichs. Leipzig: Akad. Verl. Ges.
- Read, D. J., R. A. Duckett, J. Sweeney, and T. C. B. McLeish (1999). Chevron Folding Instability in Thermoplastic Elastomers and Other Layered Materials. *J. Phys. Appl. Phys.* 32.16, pp. 2087–2099. DOI: 10.1088/0022-3727/32/16/319.
- Riedel-Kruse, I. H., C. Muller, and A. C. Oates (2007). Synchrony Dynamics During Initiation, Failure, and Rescue of the Segmentation Clock. *Science* 317.5846, pp. 1911–1915. DOI: 10.1126/science.1142538.

- Rodrigo Albors, A. (2014). *Cellular and Molecular Mechanisms Underlying Spinal Cord Regeneration in Ambystoma Mexicanum*. PhD Thesis. Dresden: Technische Universität Dresden. 114 pp.
- Rodrigo Albors, A. and E. M. Tanaka (2015). High-Efficiency Electroporation of the Spinal Cord in Larval Axolotl. In: *Salamanders in Regeneration Research*. Vol. 1290. Methods in Molecular Biology. New York: Springer New York, pp. 115–125. DOI: 10.1007/978-1-4939-2495-0_9.
- Rodrigo Albors, A., A. Tazaki, F. Rost, S. Nowoshilow, O. Chara, and E. M. Tanaka (2015). Planar Cell Polarity-Mediated Induction of Neural Stem Cell Expansion during Axolotl Spinal Cord Regeneration. *eLife* 4, e10230. DOI: 10.7554/eLife.10230.
- Roeder, A. H. K., P. T. Tarr, C. Tobin, X. Zhang, V. Chickarmane, A. Cunha, and E. M. Meyerowitz (2011). Computational Morphodynamics of Plants: Integrating Development over Space and Time. *Nat. Rev. Mol. Cell Biol.* 12.4, pp. 265–273. DOI: 10.1038/nrm3079.
- Rost, F. (2010). *Modelling and Analysis of the Chevron Formation in the Fish Myotome*. Diplomarbeit. Dresden: Technische Universität Dresden. 72 pp. DOI: 10.5281/zenodo.50522.
- Rost, F., C. Eugster, C. Schröter, A. C. Oates, and L. Brusch (2014). Chevron Formation of the Zebrafish Muscle Segments. *J. Exp. Biol.* 217.21, pp. 3870–3882. DOI: 10.1242/jeb.102202.
- Rost, F., A. Rodrigo Albors, V. Mazurov, L. Brusch, A. Deutsch, E. M. Tanaka, and O. Chara (2016a). Accelerated Cell Divisions Drive the Outgrowth of the Regenerating Spinal Cord in Axolotls. *eLife* 5, e20357. DOI: 10.7554/eLife.20357.
- (2016b). *Accelerated Cell Divisions Drive the Outgrowth of the Regenerating Spinal Cord in Axolotls - Supplementary File 1*. DOI: 10.5281/zenodo.59817.
- (2016c). *Accelerated Cell Divisions Drive the Outgrowth of the Regenerating Spinal Cord in Axolotls - Supplementary File 2*. DOI: 10.5281/zenodo.59824.
- (2016d). *Accelerated Cell Divisions Drive the Outgrowth of the Regenerating Spinal Cord in Axolotls - Supplementary Notebooks - v1.0*. *Zenodo*. DOI: 10.5281/zenodo.160333.
- Sahay, A., K. N. Scobie, A. S. Hill, C. M. O’Carroll, M. A. Kheirbek, N. S. Burghardt, A. A. Fenton, A. Dranovsky, and R. Hen (2011). Increasing Adult Hippocampal Neurogenesis Is Sufficient to Improve Pattern Separation. *Nature* 472.7344, pp. 466–470. DOI: 10.1038/nature09817.
- Sasai, Y. (2013). Cytosystems Dynamics in Self-Organization of Tissue Architecture. *Nature* 493.7432, pp. 318–326. DOI: 10.1038/nature11859.
- Schindelin, J. et al. (2012). Fiji: An Open-Source Platform for Biological-Image Analysis. *Nat. Methods* 9.7, pp. 676–682. DOI: 10.1038/nmeth.2019.
- Schleiden, M. (1838). Beiträge Zur Phytogenesis. *Arch. Für Anat. Physiol. Wiss. Med.* pp. 137–176.
- Schnapp, E., M. Kragl, L. Rubin, and E. M. Tanaka (2005). Hedgehog Signaling Controls Dorsoventral Patterning, Blastema Cell Proliferation and Cartilage Induction during

- Axolotl Tail Regeneration. *Development* 132.14, pp. 3243–3253. DOI: 10.1242/dev.01906.
- Schrödinger, E. (2008). *What Is Life?: With Mind and Matter and Autobiographical Sketches*. Canto ed., 18th printing. Cambridge: Cambridge University Press. 184 pp.
- Schröter, C., S. Ares, L. G. Morelli, A. Isakova, K. Hens, D. Soroldoni, M. Gajewski, F. Jülicher, S. J. Maerkl, B. Deplancke, and A. C. Oates (2012). Topology and Dynamics of the Zebrafish Segmentation Clock Core Circuit. *PLoS Biol.* 10.7, e1001364. DOI: 10.1371/journal.pbio.1001364.
- Schröter, C., L. Herrgen, A. Cardona, G. J. Brouhard, B. Feldman, and A. C. Oates (2008). Dynamics of Zebrafish Somitogenesis. *Dev. Dyn.* 237.3, pp. 545–553. DOI: 10.1002/dvdy.21458.
- Schwann, T. (1839). *Mikroskopische Untersuchungen Über Die Uebereinstimmung in Der Struktur Und Dem Wachsthum Der Thiere Und Pflanzen*. 1st ed. Berlin: Sander. 270 pp.
- Sepich, D. S., J. Wegner, S. O’Shea, and M. Westerfield (1998). An Altered Intron Inhibits Synthesis of the Acetylcholine Receptor Alpha-Subunit in the Paralyzed Zebrafish Mutant Nic1. *Genetics* 148.1, pp. 361–372.
- Sepich, D. S., R. K. Ho, and M. Westerfield (1994). Autonomous Expression of the Nic1 Acetylcholine Receptor Mutation in Zebrafish Muscle Cells. *Dev. Biol.* 161.1, pp. 84–90. DOI: 10.1006/dbio.1994.1010.
- Shann, E. W. (1914). On the Nature of the Lateral Muscle in Teleostei. *Proc. Zool. Soc. Lond.* 84.2, pp. 319–337.
- Shu, D.-G., S. C. Morris, and X.-L. Zhang (1996). A Pikaia-like Chordate from the Lower Cambrian of China. *Nature* 384.6605, pp. 157–158. DOI: 10.1038/384157a0.
- Singer, S. (1993). Layer Buckling in Smectic-A Liquid Crystals and Two-Dimensional Stripe Phases. *Phys. Rev. E* 48.4, pp. 2796–2804. DOI: 10.1103/PhysRevE.48.2796.
- Smith, C. L. and P. P. Dendy (1962). Relation between Mitotic Index, Duration of Mitosis, Generation Time and Fraction of Dividing Cells in a Cell Population. *Nature* 193.4815, pp. 555–556. DOI: 10.1038/193555a0.
- Spalding, K. L., E. Arner, P. O. Westermark, S. Bernard, B. A. Buchholz, O. Bergmann, L. Blomqvist, J. Hoffstedt, E. Näslund, T. Britton, H. Concha, M. Hassan, M. Rydén, J. Frisén, and P. Arner (2008). Dynamics of Fat Cell Turnover in Humans. *Nature* 453.7196, pp. 783–787. DOI: 10.1038/nature06902.
- Spalding, K. L., O. Bergmann, K. Alkass, S. Bernard, M. Salehpour, H. B. Huttner, E. Boström, I. Westerlund, C. Vial, B. A. Buchholz, G. Possnert, D. C. Mash, H. Druid, and J. Frisén (2013). Dynamics of Hippocampal Neurogenesis in Adult Humans. *Cell* 153.6, pp. 1219–1227. DOI: 10.1016/j.cell.2013.05.002.
- Spalding, K. L., R. D. Bhardwaj, B. A. Buchholz, H. Druid, and J. Frisén (2005). Retrospective Birth Dating of Cells in Humans. *Cell* 122.1, pp. 133–143. DOI: 10.1016/j.cell.2005.04.028.

- Starruß, J., W. de Back, L. Bruschi, and A. Deutsch (2014). Morpheus: A User-Friendly Modeling Environment for Multiscale and Multicellular Systems Biology. *Bioinformatics* 30.9, pp. 1331–1332. DOI: 10.1093/bioinformatics/btt772.
- Steventon, B., F. Duarte, R. Lagadec, S. Mazan, J.-F. Nicolas, and E. Hirsinger (2016). Species-Specific Contribution of Volumetric Growth and Tissue Convergence to Posterior Body Elongation in Vertebrates. *Development* 143.10, pp. 1732–1741. DOI: 10.1242/dev.126375.
- Stickney, H. L., M. J. Barresi, and S. H. Devoto (2000). Somite Development in Zebrafish. *Dev. Dyn.* 219.3, pp. 287–303. DOI: 10.1002/1097-0177(2000)9999:9999<::AID-DVDY1065>3.0.CO;2-A.
- Sugiura, T., H. Wang, R. Barsacchi, A. Simon, and E. M. Tanaka (2016). MARCKS-like Protein Is an Initiating Molecule in Axolotl Appendage Regeneration. *Nature* 531.7593, pp. 237–240. DOI: 10.1038/nature16974.
- Swigon, D. (2012). Ensemble Modeling of Biological Systems. In: *Mathematics and Life Sciences*. Ed. by A. V. Antoniouk and R. V. N. Meirik. De Gruyter.
- Taber, L. A. (2009). Towards a Unified Theory for Morphomechanics. *Philos. Trans. R. Soc. Lond. Math. Phys. Eng. Sci.* 367.1902, pp. 3555–3583. DOI: 10.1098/rsta.2009.0100.
- Tanaka, E. M. (2003). Regeneration: If They Can Do It, Why Can't We? *Cell* 113.5, pp. 559–562. DOI: 10.1016/S0092-8674(03)00395-7.
- Tanaka, E. M. and P. Ferretti (2009). Considering the Evolution of Regeneration in the Central Nervous System. *Nat. Rev. Neurosci.* 10.10, pp. 713–723. DOI: 10.1038/nrn2707.
- Te Kronnié, G. (2000). Axial Muscle Development in Fish. *Basic Appl. Myol.* 10.6, pp. 261–267.
- Thompson, D. W. (1915). Morphology and Mathematics. *Trans. R. Soc. Edinb.* 50.4.
– (1992). *On Growth and Form*. Ed. by J. T. Bonner. Canto ed. Cambridge: Cambridge University Press. 376 pp.
- Turing, A. M. (1952). The Chemical Basis of Morphogenesis. *Philos. Trans. R. Soc. Lond. B Biol. Sci.* 237.641, pp. 37–72. DOI: 10.1098/rstb.1952.0012.
- Turner, J. S. (2007). *The Tinkerer's Accomplice: How Design Emerges from Life Itself*. Cambridge: Harvard University Press.
- Van der Stelt, A. (1968). *Spijermechanica En Myotoombouw Bij Vissen*. PhD Thesis. Amsterdam: University of Amsterdam.
- Van der Meulen, T., H. Schipper, J. van Leeuwen, and S. Kranenbarg (2005). Effects of Decreased Muscle Activity on Developing Axial Musculature in Nic(B107) Mutant Zebrafish (*Danio Rerio*). *J. Exp. Biol.* 208.19, pp. 3675–3687. DOI: 10.1242/jeb.01826.
- Van Eeden, F. et al. (1996). Mutations Affecting Somite Formation and Patterning in the Zebrafish, *Danio Rerio*. *Development* 123.1, pp. 153–164.
- Van Leeuwen, J. (1999). A Mechanical Analysis of Myomere Shape in Fish. *J. Exp. Biol.* 202.23, pp. 3405–3414.

- Van Leeuwen, J., T. van der Meulen, H. Schipper, and S. Kranenborg (2008). A Functional Analysis of Myotomal Muscle-Fibre Reorientation in Developing Zebrafish *Danio Rerio*. *J. Exp. Biol.* 211.8, pp. 1289–1304. DOI: 10.1242/jeb.012336.
- Van Raamsdonk, W., W. Mos, G. Te Kronnié, C. W. Pool, and P. Mijzen (1979). Differentiation of the Musculature of the Teleost *Brachydanio-Rerio*. 2. Effects of Immobilization on the Shape and Structure of Somites. *Acta Morphol. Neerl. Scand.* 17.4, pp. 259–274.
- Van Raamsdonk, W., C. W. Pool, P. Mijzen, W. Mos, and A. van der Stelt (1977). On the Relation between Movements and the Shape of the Somites in Early Embryos of the Teleost *Brachydanio Rerio*. *Bijdr. Tot Dierkd.* 46.2, pp. 261–274.
- Van Raamsdonk, W., C. W. Pool, and G. Te Kronnié (1978). Differentiation of Muscle Fiber Types in the Teleost *Brachydanio Rerio*. *Anat. Embryol. (Berl.)* 153.2, pp. 137–155. DOI: 10.1007/BF00343370.
- Van Raamsdonk, W., A. van der Stelt, P. C. Diegenbach, W. van de Berg, H. de Bruyn, J. van Dijk, and P. Mijzen (1974a). Differentiation of Musculature of Teleost *Brachydanio-Rerio*. 1. Myotome Shape and Movements in Embryo. *Z. Für Anat. Entwicklungsgeschichte* 145.3, pp. 321–342. DOI: 10.1007/BF00519641.
- Van Raamsdonk, W., A. van Der Stelt, P. C. Diegenbach, and P. Nijzen (1974b). Nederlandse Dierkundige Vereniging (Netherlands Zoological Society). *Neth. J. Zool.* 25, p. 376. DOI: 10.1163/002829675X00344.
- Videler, J. J. (1993). *Fish Swimming*. Suffolk: Chapman & Hall. 298 pp.
- Vincent, C. D., F. Rost, W. Masselink, L. Bruschi, and E. M. Tanaka (2015). Cellular Dynamics Underlying Regeneration of Appropriate Segment Number during Axolotl Tail Regeneration. *BMC Dev. Biol.* 15, p. 48. DOI: 10.1186/s12861-015-0098-1.
- Virchow, R. (1858). *Die Cellularpathologie in Ihrer Begründung Auf Physiologische Und Pathologische Gewebelehre*. 1st ed. Berlin: Hirschwald. 440 pp.
- Von Seckendorff Hoff, K. and R. J. Wassersug (1986). The Kinematics of Swimming in Larvae of the Clawed Frog, *Xenopus Laevis*. *J. Exp. Biol.* 122.1, pp. 1–12.
- Vries, H. D. (1958). Atomic Bomb Effect: Variation of Radiocarbon in Plants, Shells, and Snails in the Past 4 Years. *Science* 128.3318, pp. 250–251. DOI: 10.1126/science.128.3318.250.
- Wallingford, J. B. (2012). Planar Cell Polarity and the Developmental Control of Cell Behavior in Vertebrate Embryos. *Annu. Rev. Cell Dev. Biol.* 28, pp. 627–653. DOI: 10.1146/annurev-cellbio-092910-154208.
- Walt, S. van der, S. C. Colbert, and G. Varoquaux (2011). The NumPy Array: A Structure for Efficient Numerical Computation. *Comput. Sci. Eng.* 13.2, pp. 22–30. DOI: 10.1109/MCSE.2011.37.
- Waskom, M. et al. (2016). Seaborn: V0.7.1 (June 2016). *Zenodo*. DOI: 10.5281/zenodo.54844.
- Weinberg, E., M. Allende, C. Kelly, A. Abdelhamid, T. Murakami, P. Andermann, O. Doerre, D. Grunwald, and B. Riggelman (1996). Developmental Regulation of Zebrafish MyoD in Wild-Type, No Tail and Spadetail Embryos. *Development* 122.1, pp. 271–280.

- Westerfield, M., D. W. Liu, C. B. Kimmel, and C. Walker (1990). Pathfinding and Synapse Formation in a Zebrafish Mutant Lacking Functional Acetylcholine Receptors. *Neuron* 4.6, pp. 867–874. DOI: 10.1016/0896-6273(90)90139-7.
- Wickström, A. (1897). Über Die Innervation Und Den Bau Der Myomeren Der Rumpfmuskulatur Einiger Fische. *Anat. Anz.* 13, pp. 401–408.
- Willemse, J. J. (1966). Functional Anatomy of the Myosepta in Fishes. *K. Ned. Akad. Van Wetenschappen Proc. Ser. C Biol. Med. Sci.* 69, pp. 58–63.
- Windner, S. E., N. C. Bird, S. E. Patterson, R. A. Doris, and S. H. Devoto (2012). Fss/Tbx6 Is Required for Central Dermomyotome Cell Fate in Zebrafish. *Biol. Open* 1.8, pp. 806–814. DOI: 10.1242/bio.20121958.
- Wolff, C., S. Roy, and P. W. Ingham (2003). Multiple Muscle Cell Identities Induced by Distinct Levels and Timing of Hedgehog Activity in the Zebrafish Embryo. *Curr. Biol.* 13.14, pp. 1169–1181. DOI: 10.1016/S0960-9822(03)00461-5.
- Wolpert, L. (1969). Positional Information and the Spatial Pattern of Cellular Differentiation. *J. Theor. Biol.* 25.1, pp. 1–47. DOI: 10.1016/S0022-5193(69)80016-0.
- Wolpert, L., R. Beddington, T. Jessell, P. Lawrence, E. Meyerowitz, and J. Smith (2002). *Principles of Development*. 2nd ed. Oxford: Oxford University Press. 542 pp.
- Wolpert, L., C. Tickle, and T. Arias (2015). *Principles of Development*. 5th ed. Oxford: Oxford University Press. 721 pp.
- Wunder, W. (1936). *Physiologie Der Süßwasserfische Mitteleuropas*. Vol. 2B. Handbuch der Binnenfischerei Mitteleuropas. Stuttgart: Schweizerbart. 340 pp.
- Yin, C. and L. Solnica-Krezel (2007). Convergence and Extension Movements Affect Dynamic Notochord-Somite Interactions Essential for Zebrafish Slow Muscle Morphogenesis. *Dev. Dyn.* 236.10, pp. 2742–2756. DOI: 10.1002/dvdy.21295.
- Yoshigai, E., S. Kawamura, S. Kuhara, and K. Tashiro (2009). Trim36/Haprin Plays a Critical Role in the Arrangement of Somites during *Xenopus* Embryogenesis. *Biochem. Biophys. Res. Commun.* 378.3, pp. 428–432. DOI: 10.1016/j.bbrc.2008.11.069.
- Zhang, F., P. Ferretti, and J. D. Clarke (2003). Recruitment of Postmitotic Neurons into the Regenerating Spinal Cord of Urodeles. *Dev. Dyn.* 226.2, pp. 341–348. DOI: 10.1002/dvdy.10230.

ACKNOWLEDGEMENTS

Thank you, Andreas Deutsch. Your lectures inspired me to explore Biology. And you gave me the opportunity to start in the IMC where I enjoyed so much freedom and so many inspirations. Thanks for your trust in my abilities. I am very grateful for that.

Equally grateful I am to Lutz Brusch. You sketched the plans for my work and accompanied me since I started becoming a scientist. You guided me in countless weekly meetings, discussed every detail with me and gave me the chance to try out so many paths. We still have a lot to do!

I am indebted to Elly M. Tanaka for all her inspiring work, which I enjoy reading so much, for writing papers together and for agreeing to review this thesis.

Thank you, Osvaldo Chara. You are a great scientist and a fantastic friend. When you joined the group, I immediately knew I wanted to work with this guy. It took us a while to get started, but it has not stopped since. I hope it stays that way. Without our endless discussions, I would not be the scientist I am today.

The ZIH offered a fantastic working environment. Claudia Schmidt, Conny Okuma, Cordula Hacker and Jenny Baumann made bureaucracy the least of my troubles, thank you! And I am especially grateful to my colleagues within the IMC who were always so helpful. In particular, the $\mathcal{O}(10^3)$ coffees with Walter de Back and Jörn Starruß as well as the discussions with Anja Voß-Böhme made an impact.

Thank you, Aida Rodrigo Albors, for taking the challenges of our collaborative work. I was always impressed by your deep knowledge of the matter. Your intuition is much faster than every piece of code I ever wrote and indeed most things turned out to be significant in the end. I am looking forward to the next coffee and discussion round, for sure!

Thank you, Andrew C. Oates. When I wrote my first paper with you and Lutz, I learned so much about science and writing. It was a pleasure.

I want to thank Nuno Barros for his enlightening course on statistics. It changed my thinking.

I enjoyed growing into a scientific environment strongly influenced by #OpenScience. Most of all, the easily available open source tools in the Python world made coding so

enjoyable. I would like to thank all of the developers and contributors.

I'd like to thank all my friends, especially all the guys I had and have the pleasure of playing in a band with, as well as my K47 friends and colleagues David Kajcsos and Matthias Schmidt. Thanks for making life good and for sometimes listening to my endless ramblings about my scientific ventures. Special thanks go to Colin Murphy who took the time to review parts of my writing.

Finally, I would like to thank my lovely Sabine. Nothing would be as good without you. Thank you, Paulina and Emil, both of you allowed me to take welcome breaks from science. I also want to thank my mom, Heidi and Jürgen for their support. You were always there when we needed you.

VERSICHERUNG

Hiermit versichere ich, dass ich die vorliegende Arbeit ohne unzulässige Hilfe Dritter und ohne Benutzung anderer als der angegebenen Hilfsmittel angefertigt habe; die aus fremden Quellen direkt oder indirekt übernommenen Gedanken sind als solche kenntlich gemacht. Die Arbeit wurde bisher weder im Inland noch im Ausland in gleicher oder ähnlicher Form einer anderen Prüfungsbehörde vorgelegt.

Die Dissertation wurde am Zentrum für Informationsdienste und Hochleistungsrechnen (ZIH) der Technischen Universität Dresden unter Betreuung von Prof. Dr. Elly M. Tanaka, Dr. Lutz Brusch, Dr. Osvaldo Chara und Prof. Dr. Andreas Deutsch angefertigt.

Es haben keine früheren erfolglosen Promotionsverfahren stattgefunden.

Ich erkenne die Promotionsordnung der Fakultät Mathematik und Naturwissenschaften, Technische Universität Dresden vom 23.02.2011 an.

15. März 2017, Fabian Rost